

**Dark features in the solar corona and the underlying
magnetic field studied with Solar Orbiter**

Von der Fakultät für Elektrotechnik, Informationstechnik, Physik
der Technischen Universität Carolo-Wilhelmina zu Braunschweig

zur Erlangung des Grades eines Doktors

der Naturwissenschaften (Dr. rer. nat.)

genehmigte Dissertation

von Jonathan David Nölke

aus Paderborn

1. Referent: Prof. Dr. Karl-Heinz Glaßmeier

2. Referent: Prof. Dr. Sami Solanki

eingereicht am: 30.04.2025

Disputation am: 17.07.2025

Druckjahr: 2026

**Dissertation an der Technischen Universität Braunschweig,
Fakultät für Elektrotechnik, Informationstechnik, Physik**

© Jonathan David Nölke



This work is distributed under a
Creative Commons Attribution 4.0 License

Printed in Germany

Cover figure:

Artistic representations of the Sun, based on an SDO/AIA 171 Å observation from 2021 November 5, and Solar Orbiter, inspired by ESA illustrations, both shown against a stellar background.

Abstract

The solar corona shows a variety of structures characterised by significantly reduced emission in the extreme ultraviolet (EUV). These include coronal holes (CHs), coronal dimmings, filaments, dark halos around active regions (ARs), and smaller-scale features such as coronal voids. While they share the common property of diminished EUV brightness, the physical conditions that give rise to these structures can differ greatly, and are, in some cases, not yet fully understood. This thesis combines two complementary studies of EUV-dark structures, focusing on a very first description of features we termed coronal voids embedded in the quiet Sun (QS) and on dark halos surrounding ARs, both aimed at exploring the relationship between EUV emission and the underlying photospheric magnetic field in these low-emission structures.

For these studies, we utilised the Extreme Ultraviolet Imager (EUI) aboard Solar Orbiter to capture high-resolution observations of the solar corona, providing detailed imaging of fine-structures. These observations were complemented by co-temporal line-of-sight magnetograms from the Polarimetric and Helioseismic Imager (SO/PHI), which allow for a direct comparison between the coronal emission and the underlying photospheric magnetic field. The study of dark halos surrounding ARs additionally uses supplementary data from the Solar Dynamics Observatory (SDO).

The first study examines dark coronal features in the QS that had not been identified or investigated before. These typically span scales from a few granules to several supergranules (~ 30 Mm). These coronal voids were identified in EUI data using a 75% intensity threshold of the mean QS emission and exhibit an average brightness of only 67% of the surrounding field of view. To investigate the origin of their reduced emission, two competing hypotheses were considered. One proposes that coronal voids are miniature analogues of CHs, with one dominant magnetic polarity and an open magnetic field configuration, which would account for a net loss of plasma and lower emission. The second hypothesis suggests that these regions appear dark because of reduced coronal heating resulting from a locally weak photospheric magnetic field. To test both scenarios, a co-temporal SO/PHI magnetogram was analysed to assess the underlying magnetic flux. The results show a significant reduction in magnetic flux density by at least 76%—compared to adjacent QS areas, and an absence of strong magnetic network structures. These findings support the second hypothesis, indicating that the dark appearance of coronal voids is primarily a consequence of reduced magnetic heating of the corona. The results identify coronal voids as a previously unrecognised category of EUV-dark structures, distinct from CHs in both scale and magnetic configuration.

The second project addresses a different class of EUV-dark regions: coronal dark halos surrounding ARs. These structures show significantly reduced emission at temperatures at or below 1 MK. Although they are sometimes mistaken for CHs, they differ substantially in

their magnetic and thermal characteristics. The mechanisms underlying their formation remain unclear, despite several proposed models. This study takes a new approach by analysing the variation of both coronal emission and photospheric magnetic field strength as a function of radial distance from the centre of AR NOAA 12893. High-resolution observations from Solar Orbiter's EUVI and SO/PHI instruments were combined with SDO data to probe the coronal plasma across a broader temperature range. The results show that while emission at lower coronal temperatures remains uniformly suppressed across the dark halo, the hotter component above 1.6 MK reveals a clear radial gradient: emission levels decrease with distance from the AR, eventually approaching QS values. Similarly, the underlying magnetic field is generally weaker within the dark halo compared to adjacent bright areas. Compared with the QS, however, the field in the dark halo is stronger close to the AR, but decreases towards its outer boundary, falling below the QS mean on the mean. Near its outer edge, it takes on values typical of those found in coronal voids. These findings point to the dark halo's reduced emission, especially in the outer regions, arising from the diminishing magnetic field that likely limits local heating. In the areas of the dark halo with stronger magnetic fields closer to the AR other mechanisms are anticipated to act in addition to the reduced heating.

This thesis offers new insights into the magnetic and radiative properties of EUV-dark structures in the solar corona, utilising snapshot observations. In future, expanding this research to include time-series observations would allow for a detailed analysis of the evolution and dynamics of these structures. Initial considerations for such future investigations are also discussed, paving the way for a more comprehensive understanding and continued exploration.

Key words: Sun: photosphere – Sun: corona – Sun: magnetic fields – Sun: atmosphere – Sun: sunspots

Zusammenfassung

Die Sonnenkorona weist eine Fülle komplexer Strukturen auf, die sich durch eine verminderte Emission im Bereich der extrem ultravioletten (EUV) Strahlung auszeichnen. Dazu zählen koronale Löcher, koronale Verdunkelungen, Filamente, dunkle koronale Halos im Umfeld aktiver Regionen sowie Coronal Voids. Obwohl alle diese Phänomene die Eigenschaft reduzierter EUV-Helligkeit besitzen, unterscheiden sich die physikalischen Bedingungen, die ihrer Entstehung zugrunde liegen, erheblich und sind teilweise nicht vollständig geklärt. In dieser Arbeit werden zwei Studien vorgestellt, die sich mit EUV-dunklen Strukturen befassen: Im Fokus stehen einerseits erstmals beschriebene Strukturen in der ruhigen Sonne, die als Coronal Voids bezeichnet werden, und andererseits dunkle Halos im Umfeld aktiver Regionen. Beide Arbeiten verfolgen das Ziel, ein besseres Verständnis für die Wechselwirkungen zwischen EUV-Emission und den damit assoziierten photosphärischen Magnetfeldern zu gewinnen.

Die Studien verwenden hochauflösende Bilder der Sonnenkorona, aufgenommen vom Extreme Ultraviolet Imager (EUI) an Bord von Solar Orbiter, die eine detaillierte Darstellung von Feinstrukturen ermöglichen. Ergänzt werden diese Beobachtungen durch zeitgleiche Magnetogramme, die vom Polarimetric and Helioseismic Imager (SO/PHI) erfasst wurden. Die Magnetogramme ermöglichen einen direkten Vergleich zwischen der koronalen Emission und dem darunterliegenden photosphärischen Magnetfeld. Für die Analyse der dunklen Halos um die aktiven Regionen werden über die Solar Orbiter Aufnahmen hinaus ergänzende Beobachtungen des Solar Dynamics Observatory (SDO) herangezogen.

Die erste Studie befasst sich mit dunklen koronalen Strukturen in der ruhigen Sonne, die zuvor noch nicht identifiziert und untersucht worden sind. Sie liegen typischerweise in der Größenordnung von wenigen Supergranulen (~ 30 Mm). Diese Coronal Voids werden in den EUI Bildern mittels einer Intensitätsschwelle von 75% der durchschnittlichen ruhige-Sonne-Emission identifiziert und zeigen eine durchschnittliche Helligkeit von nur 67% im Vergleich zu ihrer Umgebung. Um die Ursache der reduzierten Emission zu klären, wurden zwei konkurrierende Hypothesen aufgestellt und geprüft: Die erste Hypothese interpretiert Coronal Voids als Miniaturanaloga koronaler Löcher, die durch ein offenes und stark unipolares Magnetfeld gekennzeichnet sind und dadurch einen Nettoverlust an Plasma sowie eine geringere Emission aufweisen. Die alternative Hypothese besagt, dass die geringere Helligkeit dieser Regionen auf eine verringerte koronale Aufheizung zurückzuführen ist, verursacht durch ein lokal schwaches photosphärisches Magnetfeld. Zur Überprüfung beider Hypothesen wurde ein zeitgleiches Magnetogramm vom SO/PHI Instrument analysiert, um den zugrunde liegenden magnetischen Fluss zu bestimmen. Die Ergebnisse zeigen eine signifikante Reduktion der magnetischen Flussdichte um mindestens 76% im Vergleich zu benachbarten Bereichen der ruhigen Sonne sowie das

Fehlen starker magnetischer Netzwerkstrukturen. Diese Befunde stützen die Hypothese, dass die verringerte magnetische Aufheizung der Korona hauptsächlich für das dunkle Erscheinungsbild der Coronal Voids verantwortlich ist. Damit konnten Coronal Voids als eine zuvor unerkannte Kategorie EUV-dunkler Strukturen identifiziert werden, die sich sowohl in ihrer Größe als auch in ihrer magnetischen Konfiguration deutlich von koronalen Löchern unterscheiden.

Das zweite Forschungsprojekt widmet sich einer weiteren Kategorie von EUV-dunklen Bereichen: den koronalen dunklen Halos, die aktive Regionen umgeben. Diese Strukturen weisen bei Temperaturen von bis zu 1 MK deutlich verminderte Emission auf. Obwohl sie gelegentlich mit koronalen Löchern verwechselt werden, unterscheiden sie sich wesentlich in ihren magnetischen und thermischen Eigenschaften. Die zugrunde liegenden Entstehungsmechanismen sind trotz zahlreicher existierender Modelle bislang nicht abschließend geklärt. In dieser Studie wird ein neuer Analyseansatz verfolgt, indem sowohl die Variation der koronalen Emission als auch die Stärke des photosphärischen Magnetfeldes in Abhängigkeit von der radialen Entfernung zum Zentrum der aktiven Region NOAA 12893 untersucht werden. Hochauflösende Beobachtungen der EUV und SO/PHI Instrumente an Bord des Solar Orbiter wurden mit Daten des SDO kombiniert, um das koronale Plasma über ein breiteres Temperaturspektrum hinweg zu untersuchen. Die Ergebnisse zeigen, dass die Emission bei niedrigeren koronalen Temperaturen im gesamten dunklen Halo gleichmäßig verringert bleibt, während die heißere Komponente oberhalb von 1,6 MK ein klares radiales Gefälle aufweist: Die Emissionswerte sinken mit zunehmender Entfernung zur aktiven Region und nähern sich schließlich denen der ruhigen Sonne an. Auch das photosphärische Magnetfeld ist innerhalb des dunklen Halos insgesamt schwächer als in den benachbarten hellen Bereichen. In unmittelbarer Nähe der aktiven Region ist es zwar stärker als in der ruhigen Sonne, nimmt jedoch zum äußeren Rand des Halos hin kontinuierlich ab und unterschreitet dort den durchschnittlichen Wert der ruhigen Sonne. In diesen äußeren Bereichen erreicht es Magnetfeldstärken, die mit denen der Coronal Voids vergleichbar sind. Diese Ergebnisse deuten darauf hin, dass die verringerte Emission des dunklen Halos, insbesondere in seinen äußeren Regionen, auf die geringere Magnetfeldstärke zurückzuführen ist, die wahrscheinlich die lokale koronale Aufheizung begrenzt. In den Dark-Halo-Bereichen mit stärkeren Magnetfeldern, die näher an der aktiven Region liegen, dürften zusätzlich zu einer reduzierten Aufheizung weitere physikalische Mechanismen eine Rolle spielen.

Diese Arbeit liefert neue Erkenntnisse über die magnetischen und strahlungsphysikalischen Eigenschaften von EUV-dunklen Strukturen in der Sonnenkorona, basierend auf hochaufgelösten Momentaufnahmen. Zukünftige Untersuchungen unter Verwendung von Zeitreihendaten könnten eine detaillierte Analyse der zeitlichen Entwicklung und Dynamik dieser Strukturen ermöglichen. Aus diesem Grund werden in dieser Arbeit auch erste Ansätze für solche weiterführende Studien vorgestellt, die den Grundstein für ein vertieftes Verständnis dieser Phänomene und zukünftige Forschungsarbeiten legen.

Contents

Abstract	v
Zusammenfassung	vii
List of Figures	xiii
List of Tables	xv
1 Introduction	1
1.1 The Sun	1
1.1.1 The solar magnetic field	1
1.1.2 Different regions on the Sun	4
1.1.2.1 Active regions	4
1.1.2.2 Coronal holes	5
1.1.2.3 Quiet Sun	6
1.1.3 Coronal heating	7
1.1.3.1 Energetics in the corona	8
1.1.3.2 Heating models	11
1.1.4 Coronal dark halos and other EUV-dark structures in the vicinity of ARs	13
1.2 Diagnostics of the solar atmosphere	16
1.2.1 Measuring the photospheric magnetic field	16
1.2.1.1 Zeeman effect	16
1.2.1.2 Stokes Formalism	19
1.2.1.3 Magnetographs	20
1.2.2 Magnetic field extrapolations	21
1.3 Instruments	23

1.3.1	The Solar Orbiter Mission	23
1.3.1.1	SO/PHI	24
1.3.1.2	EUI	25
1.3.2	The Solar Dynamics Observatory	25
1.3.2.1	SDO/HMI	26
1.3.2.2	SDO/AIA	26
1.4	Motivation and thesis outline	27
2	Coronal voids and their magnetic nature	31
2.1	Introduction	31
2.2	Observations	32
2.2.1	SO/PHI observation	32
2.2.2	EUI observations	32
2.2.3	Alignment of PHI and EUI	33
2.3	Results	33
2.3.1	Defining coronal voids	34
2.3.2	Chromospheric counterparts of coronal voids	36
2.3.3	Photospheric magnetic field	38
2.3.3.1	Magnetic field in coronal voids and in the QS	38
2.3.3.2	Strong magnetic fields avoid coronal voids	39
2.3.3.3	Weak magnetic fields define coronal voids	42
2.3.4	Flux imbalance	44
2.3.5	Magnetic field extrapolation	48
2.4	Discussion and conclusions	50
3	Magnetic structure of coronal dark halos	53
3.1	Introduction	53
3.2	Observations	53
3.2.1	Photospheric magnetic field observed with SO/PHI	54
3.2.2	Coronal observations with EUI and SDO/AIA	54
3.2.3	Spatial alignment of the different data sets	55
3.3	Methods	56
3.3.1	Defining the dark halo boundaries	56

3.3.2	Determining the AR's magnetic centre and creating ring plots	57
3.4	Results	57
3.4.1	Dark halo and CH overlap	60
3.4.2	Coronal emission at different temperatures	60
3.4.2.1	Mean intensity's dependence on distance to AR centre	60
3.4.2.2	Coronal emission at different temperatures in individual dark halo patches	62
3.4.2.3	Bright loops over dark halos	64
3.4.3	Photospheric magnetic field	64
3.4.3.1	Average magnetic field strength	65
3.4.3.2	Magnetic field strength's dependence on distance to AR centre	66
3.4.3.3	Flux imbalance in dark halos	67
3.5	Discussion	68
3.5.1	Comparison of dark halos to CHs and coronal voids	68
3.5.2	Nature of dark halos	69
3.6	Conclusions	71
4	Conclusions and outlook	73
4.1	Conclusions	73
4.2	Outlook	75
4.2.1	Future research directions	75
4.2.2	Initial results of follow-up projects	76
4.2.2.1	Morphology of coronal void	78
4.2.2.2	Evolution of a coronal void	80
4.2.2.3	Coronal void at different plasma temperatures	82
	Appendix	85
A.1	Threshold of coronal voids	85
A.2	Determining the centre of the AR	87
A.3	SDO 2018 April 22 data set	90

Contents

Bibliography	93
Acknowledgments	103
Publications	105
Curriculum Vitae	107

List of Figures

1.1	Plasma β throughout the solar atmosphere	2
1.2	The solar corona observed at 1.6 MK	5
1.3	SO/PHI LOS magnetogram taken on 2021 February 23	8
1.4	Temperature and density throughout the solar atmosphere	9
1.5	The solar corona observed at 0.8 MK	14
1.6	Illustration of the transversal and longitudinal Zeeman effect	17
2.1	Overview of Solar Orbiter observations of 2021 February 23	34
2.2	Connectivity of coronal voids to the chromosphere	37
2.3	$ B_{\text{LOS}} $ in coronal voids	38
2.4	Locations of strong-field regions	39
2.5	Ratio, R , of areas of voids to QS	40
2.6	Histograms of $ B_{\text{LOS}} $ in coronal voids and in the QS	43
2.7	Distribution of $\langle B_{\text{LOS}} \rangle$ in QS areas	43
2.8	Coronal voids and weak magnetic fields	44
2.9	Relative magnetic flux imbalance illustrated for coronal voids and QS	45
2.10	Distribution of relative flux imbalance in QS areas	45
2.11	Magnetic field lines traced using a potential field extrapolation	48
3.1	Overview of 2021 November 5 observations	54
3.2	Emission from different SDO/AIA passbands	58
3.3	Relative mean HRI_{EUV} -intensity inside rings around the AR	58
3.4	Open fields originating from CH adjacent to AR	59
3.5	Relative mean HRI_{EUV} -intensity as a function of distance to the AR	59
3.6	Relative mean intensities inside individual dark halo patches	61
3.7	Enhanced images of images of SDO/AIA passbands	61

List of Figures

3.8	Mean $ B_{\text{LOS}} $ value of individual dark halo patches and QS . . .	65
3.9	$\langle B_{\text{LOS}} \rangle$ in dependence of distance to AR centre	66
3.10	$\langle B_{\text{LOS}} \rangle$ vs. distance to the AR centre for individual dark halo patches	67
4.1	Overview of the 2022 March 8 dataset	77
4.2	Cuts through a coronal void	78
4.3	Evolution of a coronal void for EUV-intensity and size	79
4.4	Evolution of the unsigned magnetic field of a coronal void . . .	79
4.5	Coronal void at different plasma temperatures	81
4.6	Relative emission in coronal void at different temperatures . . .	82
A.1	Different intensity-thresholds identifying coronal voids	85
A.2	Variations with intensity threshold in void no. 1	86
A.3	Centre of the AR determined with different methods	87
A.4	SDO/AIA 171 Å observation of 2018 April 22	89
A.5	$\langle B_{\text{LOS}} \rangle$ inside concentric rings around the AR on 2018 April 22	89
A.6	$\langle B_{\text{LOS}} \rangle$ vs. distance to the AR centre on 2018 April 22	90

List of Tables

1.1	Chromospheric and coronal energy losses	11
2.1	Properties of major coronal voids and surrounding QS	35
3.1	Magnetic field and coronal emission in individual dark halo patches	65

1. Introduction

The Sun has fascinated mankind for millennia and provides the energy that sustains life on Earth. The Sun's influence can also be felt at short time scales: Events like coronal mass ejections or flares have an almost immediate impact on us. While they can create stunning aurora, they also pose a serious hazard to satellite communication and infrastructure. As the closest star to Earth, the Sun further offers a unique opportunity for detailed observation. Unlike distant stars, it can be studied with high spatial resolution, allowing us to examine fine structures and uncover insights that can be applied to stellar physics more broadly. For these reasons, the Sun is the most important star for us to study.

1.1 The Sun

1.1.1 The solar magnetic field

The magnetic field plays a fundamental role in understanding the Sun. The field extends from the bottom of the convection zone far out into interplanetary space. Sunspots had been seen on the Sun even more than 2000 years ago by Chinese astronomer (Stephenson & Willis 1999). Their magnetic nature, however, was only discovered in 1908 by (Hale 1908).

The large-scale solar magnetic field has its origin at the bottom of the convection zone where the energy transport changes from radiation to convection (Aschwanden 2004). Through differential rotation and convection the magnetic field is created and maintained; this process is known as the solar dynamo. For a more detailed description we refer to e.g. Charbonneau (2020) and Solanki et al. (2006). The global magnetic field undergoes a reversal every 11 years and reaches its original configuration again after 22 years (extended cycle). At the beginning of each cycle (solar minimum) the magnetic field has a strong poloidal

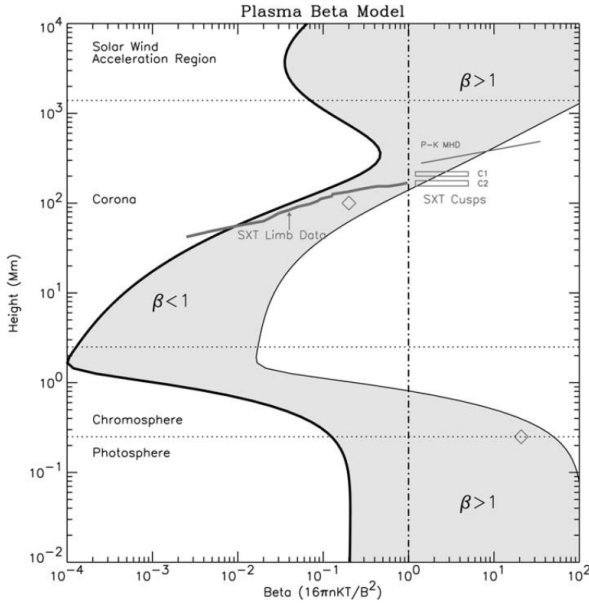


Figure 1.1: Plasma β show as a function of height above the photosphere over an AR (Gary 2001). Reproduced with permission from Springer Nature.

component, visible as unipolar fields at the poles. Due to the differential rotation in the convection zone this field becomes increasingly toroidal with increasing activity. Magnetic flux tubes with sufficient buoyancy can rise up and emerge as bipoles in the photosphere, the layer where the Sun turns from opaque to transparent at visible wavelengths. These bipoles appear most frequently during solar maximum. At the end of the cycle the field returns to a poloidal shape again. It is presumed that the Sun also possesses a small-scale dynamo (Petrovay & Szakaly 1993), which is driven by convective motions and is largely independent of the solar cycle (see, e.g. Rempel et al. (2023) for more details).

The magnetic fields that emerge in the photosphere are very inhomogeneous. Most magnetic elements are concentrated in vertically oriented flux tubes that only cover about 5% of the solar surface. The strongest fields can be found in the umbra of sunspots. These are typically 1.8 – 3.7 kG (Livingston 2002), while fields as strong as 8.2 G have also been reported by Castellanos Durán et al. (2020).

The penumbra still harbours fields of 0.7–2 kG (Solanki 1993) which are highly horizontally inclined. The smallest magnetic flux detected and traced in a feature is as low as $9 \cdot 10^{14}$ Mx (Anusha et al. 2017).

To characterise the dominant force in an atmospheric layer, we use plasma β (Wiegelmann & Sakurai 2012), which is defined as the ratio between the plasma pressure p and the magnetic pressure p_{mag} :

$$\beta = \frac{p}{p_{mag}} = \frac{nk_B T}{B^2/2\mu_0}, \quad (1.1)$$

with the particle number density n , the Boltzmann constant k_B , the magnetic field B , the temperature T , and the permeability in vacuum μ_0 .

Plasma β varies significantly throughout the solar atmosphere (Aschwanden 2004), also see Fig. 1.1). In the photosphere β is > 1 and plasma pressure is dominant. Within a flux tube, however, β can locally be reduced, e.g. to values of 0.2 – 0.4 (Solanki et al. 2006), so that in such regions the magnetic pressure governs the processes. The most prominent example is the dark umbra of sunspots, where convection is inhibited leading to a temperature reduction of 1000 – 1900 K (Solanki 1993) and consequently their dark appearance.

Towards the chromosphere β remains relatively constant because both the magnetic field and the plasma pressure decrease exponentially until the magnetic field reaches its maximum expansion filling all the available space (\sim middle chromosphere). Above this height β decreases slowly because low-laying loops reconnect to the photosphere, while the p keeps dropping rapidly. At the same time the magnetic field strength can no longer drop with height due to the maximum filling, and the balance between plasma and magnetic pressure is shifted towards a magnetic pressure dominated regime ($\beta < 1$). This low β value persists throughout the transition region and the corona. The $\beta \ll 1$ and high conductivity directs plasma flows mostly in field direction following individual field lines (frozen-in condition), while plasma flows across the field lines are strongly inhibited. In the outer corona (Wiegelmann & Sakurai 2012) β gradually increases again to above unity (typically at 2 – 3 solar radii), indicating a shift to a plasma-driven regime. This is, for example, apparent at the top of helmet

streamers where plasma is visible as it leaks out of the magnetic confinement.

1.1.2 Different regions on the Sun

The solar corona is by convention subdivided into three regions based on their magnetic topology and coronal appearance: active regions (ARs), coronal holes (CHs), and the quiet Sun (QS). This section describes each of them throughout the solar atmosphere.

1.1.2.1 Active regions

ARs are bipolar regions (or more complex structures) with magnetic fluxes of up to 10^{23} Mx in individual ARs (Hathaway 2015; Solanki et al. 2006). Large ARs often contain sunspots where the strongest magnetic flux concentrations are located, while smaller ones have pores. The suppression of convection in ephemeral regions ($< 10^{20}$ Mx) is typically lower and on smaller scales, so that they do not show reduced continuum emission like their larger counterparts. The lifetimes of ARs range from days to several months and are strongly correlated to their total magnetic flux. ARs first emerge at mid-latitudes around $\sim \pm 30^\circ$ when a new solar cycle begins (Hathaway 2015). As the cycle progresses, their formation locations migrate steadily toward the equator (Spörer's law; Spörer 1894), eventually reaching latitudes of $\sim \pm 5^\circ$ by the end of the cycle. The 11-year cycle can be defined via the sunspot number. This number peaks around solar activity maximum, while during solar activity minima the ARs can disappear completely. When ARs decay most of its magnetic flux is removed by cancellation between the two opposite magnetic polarities. Some of the remaining flux is transported towards the poles where it contributes to building up the polar field of the next solar cycle.

In the corona, ARs have a mainly closed magnetic configuration (Aschwanden 2004) with still very strong magnetic flux densities that in the lower corona can exceed 100 G (Solanki et al. 2006). The corona above ARs reaches temperatures between 1 – 10 MK and ARs are the objects with the strongest EUV and soft X-ray emission. The complexity and dynamics of their structure as well as their strong magnetic fields further make ARs the main source and trigger for coronal mass

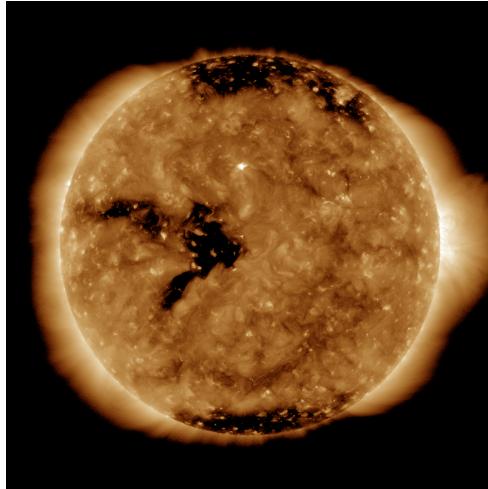


Figure 1.2: The solar corona observed at 1.6 MK in the SDO/AIA 193 Å passband on 2018 May 2 at 12:00 UTC. The polar CHs and an equatorial CH are clearly visible as areas of reduced emission.

ejection or flares (Hathaway 2015).

1.1.2.2 Coronal holes

CHs (Waldmeier 1956, 1957) are solar coronal regions that appear dark in X-ray and in ultraviolet (UV) observations (see Fig. 1.2) as they are less dense and have a lower temperature (of around 0.8 MK) than the corona anywhere else (Munro & Withbroe 1972; Cranmer 2009). Furthermore, they are structured by open magnetic fields and are the origin of the fast solar wind, the stream of charged particle emanating from the Sun at typically speeds around 600 km/s (with a range of 500 to 800 km/s; Cranmer 2009).

In solar eclipses CHs had been seen as regions above the poles and the shape of the streamers (dense radially elongated structures above magnetically closed loops; Aschwanden 2004) were already described to look like field lines of a magnet emanating from the poles (Serviss 1909). Waldmeier made a first quantitative analysis of CHs in coronagraphic observations in the 1950ies. Later,

in the 1960ies CHs were also discovered as dark structures visible on the solar disc.

During minima of solar activity, large CHs are visible at the solar poles. With the 11-year solar cycle they change. After minimum they start to decay and are completely gone at solar maximum. Towards the next solar minimum they form again. At times of non-minima, CHs also appear at lower latitudes. These on-disc or equatorial CHs are smaller in size and can sometimes be connected to the large polar CHs. They have further often been observed in close vicinity to complex ARs.

While CHs can be distinguished from QS and AR in the corona, in the photosphere, they are harder to be distinguished as the absolute magnetic flux density in CHs compares well to that of the QS (Wiegelmann & Solanki 2004). However, while the photospheric magnetic field in the QS is polarity balanced, the underlying fields of CHs on the other hand are clearly dominated by one polarity (e.g. Altschuler et al. 1972).

As a consequence, magnetic fields do not close within the CHs and magnetic field lines are locally open. With increasing height, they can further expand horizontally, contributing to a lower plasma density within the CHs. While plasma is trapped inside closed loops in the QS, the open field of the CHs opens a conduit to release energy. Gas is accelerated along the open magnetic field lines to escape the gravitational forces of the Sun. This lost energy can no longer contribute to coronal heating, resulting in a reduced emission in CHs compared to that of the QS visible at all coronal temperatures.

1.1.2.3 Quiet Sun

The areas outside of CHs and outside of sunspots and other strong magnetic flux concentrations (pores and plages) are called the QS. During solar minimum the QS dominates the solar topology.

In continuum images of the QS the typical granulation pattern can be seen (see e.g., Bellot Rubio & Orozco Suárez 2019). From the convection zone parcels of hot gas move upwards reaching the photosphere, where they appear as bright granules. The material cools down and submerges again at the edges of the

granular cells, in the intergranular lanes. Granulation is ubiquitous all over the solar surface, including in ARs. In the QS (and also in CHs) granules are typically 1–2 Mm in size and have lifetimes of 5–10 minutes.

The largest convective pattern found in the QS is supergranulation. Supergranules are about 30 Mm in diameter and have lifetimes of 1 – 2 days (Rincon & Rieutord 2018). Kilogauss magnetic field concentrations, the network, surround the supergranular cells like a web. The network is clearly visible in magnetic field map of the photosphere (see Fig. 1.3). The interior of the supergranular cells we refer to as the internetwork and it contains much fewer magnetic elements. Magnetic elements inside the internetwork move towards the boundaries of the supergranular cell. Due to their short lifetimes of a few minutes (see e.g., Hirzberger et al. 1999) only some reach the network. It is assumed that the network is sustained by the accumulation of these small-scale magnetic elements and the dispersal of ephemeral ARs (Gošić et al. 2016). The entire network contains $5.5 - 8.0 \times 10^{23}$ Mx (Gošić 2015) which compares to the total flux measured in ARs during solar maxima, see e.g. 6.0×10^{23} Mx by Jin et al. (2011) or 8.0×10^{23} Mx by Schrijver & Harvey (1994).

Since the magnetic field of the QS carries such a large amount of magnetic flux, it has a substantial contribution to coronal dynamics. The QS corona emits most of its radiation at a temperature range of 1 – 3 MK. Besides coronal loops, we see a variety of small-scale dynamics and heating events such as bright points or nanoflares (Aschwanden 2004). The QS corona further contains regions without the spatial structuring of these phenomena instead showing a diffuse emission (see, e.g., Gorman et al. 2023).

1.1.3 Coronal heating

Attempts to estimate the temperature of the solar corona from white-light observations began around the turn of the 20th century. These findings already suggested that the solar corona was much hotter (on the order of MK) than the photosphere (6,000 K). Around 1940 both Grotrian (1939) and Edlén (1943) identified coronal emission lines as forbidden atomic transitions of highly-ionised Fe, Ni, and Ca species, including the green line of Fe XIII at 5303 Å. The high

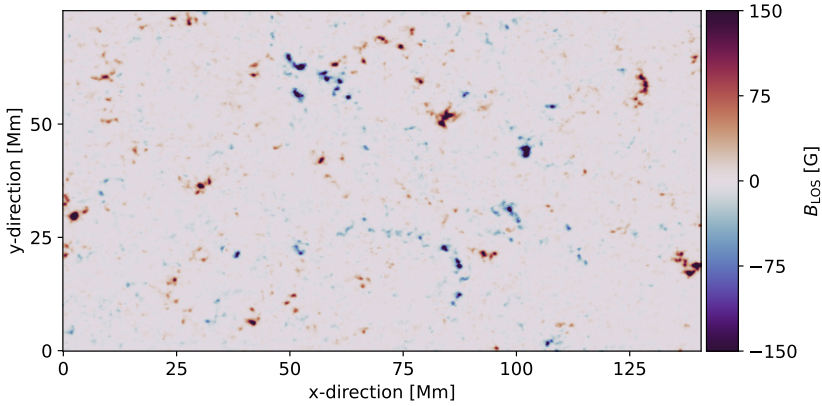


Figure 1.3: SO/PHI LOS magnetogram taken on 2021 February 23 at 17:00 UTC showing the magnetic network surrounding the supergranules.

ionization states of these ions indicated a coronal temperature far exceeding that of the photosphere. Around the same time Alfvén (1941) concluded from a six-point argumentation that the corona must be very hot (Peter & Dwivedi 2014). At first glance the change from a cooler to a hotter temperature seems to violate the second law of thermodynamics. However, this strong increase in temperature actually means that corona cannot be heated by thermal conduction and that alternative heating mechanisms must be responsible (Aschwanden 2004). Understanding the heating mechanisms of the solar corona is referred to as the ‘coronal heating problem’. A schematic of the temperature variations throughout the solar atmosphere can be found in Fig. 1.4.

1.1.3.1 Energetics in the corona

In the low $\beta \ll 1$ regime of the corona individual structures (loops and open flux tubes) remain thermally relatively isolated from each other because heat conduction is hindered transverse to the magnetic field. Heat conduction is possible along the magnetic field direction. This compensated for heat differences within a structure, while at the same time huge temperature differences can exist between neighbouring structures. The heating requirements are consequently

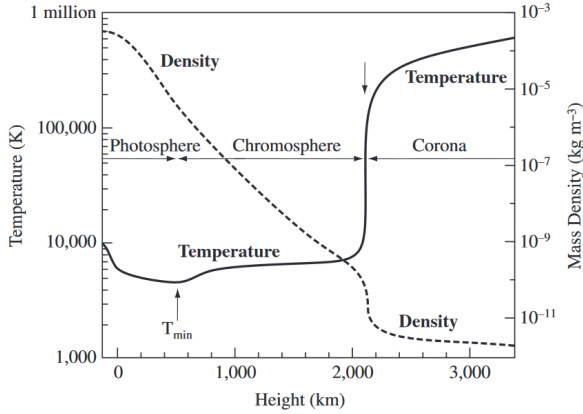


Figure 1.4: Temperature and density throughout the solar atmosphere. Reproduced from *Magnetohydrodynamics of the Sun* by Eric Priest (Priest 2014), © Cambridge University Press 2014. Reproduced with permission of The Licensor through PLSclear.

distinct for different structures and regions.

The heating rate E_H in the corona is balanced by the different loss terms, the radiative losses E_R , thermal conduction E_C , and losses to the solar wind E_{wind} :

$$E_H - E_R - E_C - E_{wind} = 0. \quad (1.2)$$

When only considering radiative losses, which is a reasonable approximation for closed loops regions, the radiative loss function can be treated as constant Λ across the temperature range of 0.5 – 3 MK, which covers most of the solar corona (Aschwanden 2004):

$$E_R = n_e^2 \Lambda(T) \approx 10^{-22} n_e^2 \quad (\text{erg cm}^{-3} \text{s}^{-1}), \quad (1.3)$$

with the density n_e inside the loop and the radiative loss function $\Lambda(T)$. This correlation further carries an important physical implication: Because the optically thin EUV emission scales with the square of the plasma density, and since the heating rate itself depends on n_e^2 , the observed EUV flux is directly proportional to the heating rate.

When additionally considering thermal losses $E_C = \nabla \cdot F_C$, with the heat flux F_C describing the energy transport along a field line, a similar dependence can be derived. Here we assume a special case (uniform heating without gravity) of the scaling laws developed by Rosner, Tucker, and Vaiana (RTV, Rosner et al. 1978) for loop heating. Inserting the ideal gas law for ionised hydrogen plasma

$$p = 2n_e k_B T, \quad (1.4)$$

where p is the pressure, n_e the electron number density, k_B the Boltzmann constant, and T the temperature, yields the dependence of the heating rate on the density:

$$E_H \propto n_e^{7/4}. \quad (1.5)$$

We now also want to consider the dependence of the temperature T on the heating rate. The temperature maximum of a loop in hydrostatic equilibrium (when the pressure gradient force and the gravitational force are balanced) lies at its apex. While most of the energy loss in a loop occurs through radiation E_R , the electron density n_e is lowest at the apex, where conductive losses E_C dominate. Therefore, the heating rate at the apex can be approximated as (Rosner et al. 1978):

$$E_H \approx E_C = \nabla \cdot F_C = \frac{\kappa_0 T^{7/2}}{L^2}, \quad (1.6)$$

with the Spitzer thermal conductivity coefficient κ_0 . From Eq. 1.6, we find that the temperature weakly scales with the heating rate $\sim E_H^{2/7}$.

Different regions on the Sun require different heating rates to be sustained. According to Withbroe & Noyes (1977) the QS requires with $3 \cdot 10^5 \text{ erg cm}^{-2} \text{ s}^{-1}$ (300 W m^{-2}) the least amount of energy. For ARs the required heat rate is $10^7 \text{ erg cm}^{-2} \text{ s}^{-1}$ ($10,000 \text{ W m}^{-2}$), and in CHs it is $7 \cdot 10^5 \text{ erg cm}^{-2} \text{ s}^{-1}$ (700 W m^{-2}). Also, the dominant loss term differs between closed and open field regions. While the dominant losses in the QS and in ARs are radiative losses, in CHs most of the energy is lost to accelerate the solar wind (see Table 1.1 for more details).

Parameter	Quiet Sun	Coronal hole	Active region
Transition layer pressure (dyn cm^{-2})	2×10^{-1}	7×10^{-2}	2
Coronal temperature (K, at $r \approx 1.1 R_0$)	$1.1\text{--}1.6 \times 10^6$	10^6	2.5×10^6
Coronal energy losses			
- Conduction flux F_c	2×10^5	6×10^4	$10^5\text{--}10^7$
- Radiative flux F_r	10^5	10^4	5×10^6
- Solar wind flux F_w	$\lesssim 5 \times 10^4$	7×10^5	$(< 10^5)$
- Total corona loss $F_c + F_r + F_w$	3×10^5	8×10^5	10^7
Chromospheric radiative losses			
- Low chromosphere	2×10^6	2×10^6	$\gtrsim 10^7$
- Middle chromosphere	2×10^6	2×10^6	10^7
- Upper chromosphere	3×10^5	3×10^5	2×10^6
- Total chromospheric loss	4×10^6	4×10^6	2×10^7
Solar wind mass loss ($\text{g cm}^{-2} \text{ s}^{-1}$)	$\lesssim 2 \times 10^{-11}$	2×10^{-10}	$(< 4 \times 10^{-11})$

Table 1.1: Chromospheric and coronal energy losses ($\text{erg cm}^{-2} \text{ s}^{-1}$). Adapted from Withbroe & Noyes (1977), with permission from Annual Reviews, Inc.

1.1.3.2 Heating models

Coronal heating models are typically categorised into direct current (DC) and alternating current (AC) types depending on the timescales of the magnetic driver in the photosphere (Cranmer & Winebarger 2019; Aschwanden 2004). Magnetic disturbances travel upwards into the corona as Alfvén waves at the characteristic speed of

$$v_A = \frac{B}{\sqrt{\mu_0 \rho}}, \quad (1.7)$$

where B represents the magnetic field strength, ρ the plasma density, and μ_0 the vacuum permeability. The time it takes for the disturbance to propagate along the full length of a coronal loop, L , is referred to as the Alfvén crossing time

$$\tau_A = \frac{L}{v_A}. \quad (1.8)$$

It is the critical timescale that sets the coronal response: In case of a slow magnetic driver ($< \tau_A$) the loop can react in a quasi-static way to adjust to the changes occurring in the photosphere. The coronal currents are therefore mostly direct ones (DC models). The loop can, however, not adjust to faster magnetic divers

leading to alternating currents (AC models). All models require that energy is both transported into the corona and there dissipated as thermal energy.

In DC heating random motions of the photospheric footpoints braid and twist the coronal magnetic field until it becomes increasingly non-potential (current-carrying). This stress at the boundaries between the different flux tubes leads to the formation of current sheets (Parker 1972, 1983, 1988). Through magnetic reconnection the magnetic field relaxes, and the energy stored in this topology is released. Parker (1988) estimate a typical energy release at $6 \cdot 10^{24}$ erg per event – nine orders of magnitude smaller than large observed flares. This is why the model is also known as the nanoflare model. Other models build on this model by extending or refining it. A notable example is the current cascade model (van Ballegooyen 1986) which proposes that within the formed current sheets the magnetic energy is transferred from large to smaller and smaller scales before it is released.

More recently, observations from the Sunrise I+II missions (Solanki et al. 2010a, 2017) revealed previously unresolved small opposite-polarity flux patches embedded within larger magnetic flux regions. Priest et al. (2018) conclude that photospheric flux cancellation is a more frequent and significant driver of magnetic reconnection than previously believed, and can release energy without the need for magnetic braiding. Chitta et al. (2017) could established a link between flux cancellation events and chromospheric jets. This suggests that jets could be instrumental in transporting material and energy into the chromosphere and corona.

AC heating describes the wave-driven energy transport into the corona. Early models focused on acoustic waves to explain coronal heating (see e.g. Schwarzschild 1948; Biermann 1948). However research by Athay & White (1978, 1979) demonstrated that these waves only carry an energy flux that is 2 – 3 orders of magnitude smaller than what is required to heat the corona. It became necessary to consider other waves as a potential heating mechanism, and due to the low plasma β regime in the corona magnetohydrodynamic (MHD) waves became a key focus.

There are three fundamental MHD wave modes: the fast magnetoacoustic

waves, slow magnetoacoustic waves, and Alfvén waves (more details on these modes can be found in Kippenhahn & Möllenhoff 1975). Of these three modes only Alfvén waves are capable of effectively delivering energy into the corona. The slow MHD waves experience strong damping in the lower corona. According to Hollweg (1978) fast MHD waves tend to reflect at the steep density gradient in the transition region. Even when they reach the corona they cannot be considered a viable source of heating due to their poor dissipation of energy. Alfvén waves, on the other hand, propagate efficiently along magnetic field lines into the corona and can dissipate their energy there. This is accomplished through the two primary mechanisms resonant absorption and phase mixing.

Phase mixing occurs because the speed of Alfvén waves varies across neighbouring magnetic field lines, partly due to differences in magnetic field strength but mainly because of variations in plasma density. This causes the waves to gradually lose synchronisation, creating shearing motions. These shearing motions then convert wave energy into thermal energy through resistive heating and viscous damping. Resonant absorption occurs when the frequency of an Alfvén wave matches the local plasma's continuum frequency, creating large oscillations at the resonant layer. These amplified oscillations induce strong currents and magnetic field gradients, also leading to energy dissipation via Ohmic heating and viscous damping.

Our current understanding of coronal heating suggests that no single mechanism is solely responsible but multiple interacting processes probably occur. The dominant process likely varies across different solar regions, depending on local magnetic field configurations and plasma conditions.

1.1.4 Coronal dark halos and other EUV-dark structures in the vicinity of ARs

ARs appear significantly brighter than the rest of the Sun across all coronal temperatures. However, structures near ARs can exhibit reduced emission, appearing not only darker than the ARs but also than the QS. These features vary widely in origin and are visible as dark structures at different temperatures. This section highlights several of them.

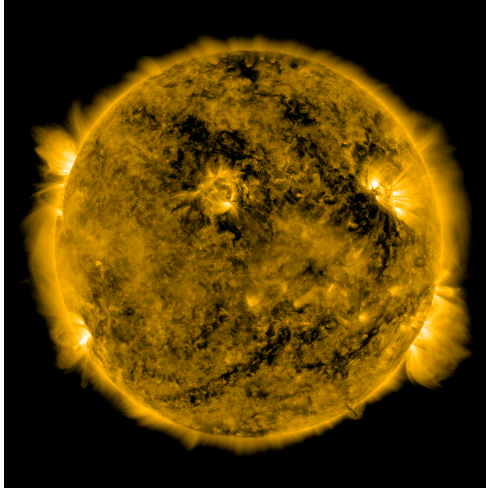


Figure 1.5: The solar corona observed at 0.8 MK in the SDO/AIA 171 Å passband on 2021 November 5 at 23:30 UTC. The ARs are surrounded by coronal dark halos, which are extended regions that exhibit reduced emission at this temperature.

At low coronal temperatures around or below 1 MK ARs are often surrounded by extended areas of significantly reduced emission as compared to the emission coming from the QS. This can be very prominently seen in data obtained by SDO/AIA at 171 Å or by the EUV HRI_{EUUV} channel. These areas of reduced emission have been referred to by different names: dark canopies (Wang et al. 2011), emerging dimmings (Zhang et al. 2012), dark halos (Andretta & Del Zanna 2014), or dark moats (Singh et al. 2021). For our work we have adapted the term dark halos. Dark halos are visible at all transition region temperatures and at low coronal temperatures. However, unlike CHs they cannot be distinguished from their surroundings at temperatures above 1 MK.

Several models have been proposed to explain the nature of the coronal dark halos. The model put forward by Wang et al. (2011) suggests that the dark halos show less emission due to the presence EUV absorbing material (i.e. neutral hydrogen or helium). However, as already shown by Andretta & Del Zanna (2014) and pointed out by Lezzi et al. (2023), the dark halos also appear darker at

wavelengths longer than the edge of the Lyman continuum at 912 Å.

Singh et al. (2021) conclude that the formation of the coronal dark halos results from a specific configuration of the magnetic field: The strong magnetic field from the AR reaching over the area of the dark halos presses the underlying magnetic loops down and thus restricts them in height. According to Antiochos & Noci (1986) loops below 5 Mm can only reach temperatures up to 10^5 K and, consequently, do not emit in the EUV around 1 MK. As a result, the bulk of this EUV emission is missing inside the dark halos. At 10^5 K the dark halos would be expected to show strong emission in the AIA 304 Å channel. However, Singh et al. (2021) observed the opposite and state that further research is required. Furthermore, modern 3D models produce an abundance of (transient) short loops that reach temperatures well above 10^5 K (e.g. Chen et al. 2021, 2024) invalidating the argument about missing cool loops based on old model considerations.

In their most recent study, Lezzi et al. (2024) have reported a fine structure within the dark halos consisting of interconnected EUV-bright bundles and dark regions. They found this fine structure also to be present in transition region lines and in Lyman-alpha. Further its signature can be seen in magnetograms. From this, the authors conclude that coronal dark halos could have their origin in the lower solar atmosphere.

Zhang et al. (2012) and Payne & Sun (2021) observed emerging dimmings, a reduction in emission around ARs that is similar in appearance to dark halos. However, these emerging dimmings only last for several hours and it is thus not clear whether coronal dark halos and emerging dimmings are the same phenomenon. Zhang et al. (2012) explain the reduced emission at lower coronal temperatures as a result of reconnection of the existing flux with the emerging flux. This reconfiguration of the magnetic field in the corona causes plasma to heat up leading to an increase in emission at higher temperatures and a decrease in the plasma density at lower temperatures.

Chromospheric counterparts of coronal dark halos were first identified in the early 20th century by Hale & Ellerman (1903) and St. John (1911). Later, Bumba & Howard (1965) linked these chromospheric structures to dark $H\alpha$ fibrils. However, it remains unclear whether or how they are connected to the coronal dark halos.

Coronal dark halos are only one type of EUV-dark structures in the solar corona. Other known EUV-dark structures close to ARs are CHs (a detailed description can be found in Sect. 1.1.2.2) and AR outflows. AR outflows are characterised by a strong blueshift in a Doppler velocity map at the edge of an AR (Doschek et al. 2007; Doschek et al. 2008; Sakao et al. 2007; Harra et al. 2008). The outflows typically last at least a day and are rooted in or near strong magnetic fields that are not entirely flux balanced. Additionally, they are associated with areas of reduced coronal emission due to the reduced density. Some of these outflows follow open magnetic field lines that extend into the heliosphere, while others are at the footpoints of large-scale closed loops (see, e.g., Baker et al. 2009).

1.2 Diagnostics of the solar atmosphere

1.2.1 Measuring the photospheric magnetic field

The photospheric magnetic field can be inferred by making use of the polarising properties of the Zeeman effect.

1.2.1.1 Zeeman effect

The splitting of spectral lines in the presence of an external magnetic field \mathbf{B} was first observed by Pieter Zeeman over a century ago (Zeeman 1897b,a,c). The external field induces a shift in the energy of degenerate quantum states, breaking their degeneracy. Applying a magnetic perturbation to the undisturbed Hamiltonian of an atom, yields the first-order correction due to the (linear) Zeeman effect (Solanki 1993; Stix 2002; del Toro Iniesta 2003):

$$\Delta E = mg\mu_B \mathbf{B}, \quad (1.9)$$

where μ_B is the Bohr magneton, m the magnetic quantum number (with $m = -J, -J + 1, \dots, J$), and g the Landé factor. This can also be expressed as a shift in wavelength λ

$$\Delta\lambda = -\frac{\lambda^2 mg\mu_B \mathbf{B}}{ch}, \quad (1.10)$$

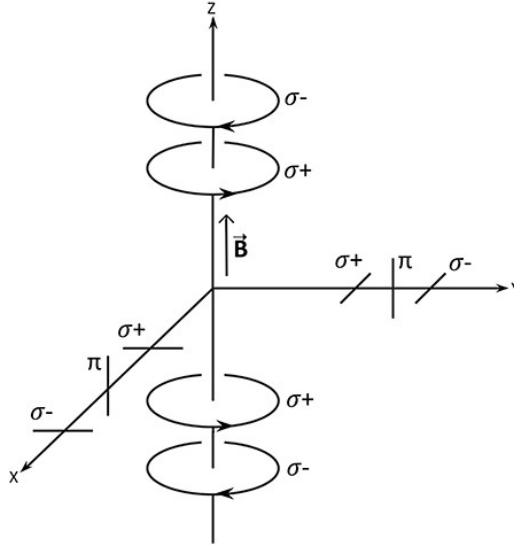


Figure 1.6: Illustration of the transversal and longitudinal Zeeman effect. The transversal Zeeman effect: A viewing angle in x- or y-direction is perpendicular to \mathbf{B} . The observer sees the linearly polarised components with different orientations for the π - and σ -components. Longitudinal Zeeman effect: The viewing angle is in z-direction parallel to \mathbf{B} and the circularly polarised σ -components can be observed. This figure has been adapted from Crutcher & Kemball (2019) under the Creative Commons Attribution License (CC BY).

with the speed of light c . The total orbital angular momentum L and the total spin S couple to form the total angular momentum $J = L + S$. In LS coupling the Landé factor of a level describes the contribution of the total angular momentum and its impact on the shift in energy:

$$g_{LS} = 1 + \frac{J(J+1) - L(L+1) + S(S+1)}{2J(J+1)} \quad (1.11)$$

One energy level J is split into $2J + 1$ components. The extent to which the components of a spectral line are shifted depends on the line's sensitivity to the total angular momentum, as determined by the magnitude of g_{LS} . Additionally, the splitting of the energy levels increases linearly with the strength of the external magnetic field and quadratically with the wavelength, meaning the shift

in wavelength is stronger at longer wavelengths. For stronger magnetic fields the dependence on the field strength is no longer linear and quadratic terms have to be considered additionally. This is referred to as the quadratic Zeeman effect. In the presence of strong magnetic fields, the LS-coupling fails leading to the emergence of different splitting patterns, which are described by the Paschen-Back effect. When this occurs strongly depends on the atomic structure and can also happen for relatively weak fields, e.g. for some transition lines seen in sunspots. From this point onwards, we limit our focus to the description of the linear Zeeman effect.

The case for $S \neq 0$ is referred to as the anomalous Zeeman effect, while in the case of $S = 0$ we have the normal Zeeman effect. Even though the anomalous Zeeman effect describes the more general case, and the normal Zeeman effect is a special case, the naming convention arises from its historic context: At the time of the discovery of the Zeeman effect the electron spin was not known and hence only the normal Zeeman effect was understood.

Possible transitions between two levels are given by the selection rule for the magnetic quantum number

$$\Delta m = \{-L, -L + 1, \dots, L - 1, L\}, \quad (1.12)$$

which simplifies for dipole transitions to:

$$\Delta m = 0, \pm 1. \quad (1.13)$$

For $S = 0$, the normal Zeeman effect results in a simple splitting into three different energy transitions, forming a triplet. In contrast, the anomalous Zeeman effect leads to the formation of more complex Zeeman multiplets. However, in weak fields multiplets can be treated as triplets by calculating an effective Landé factor.

In a triplet the π -component remains unshifted in wavelength, while the two σ components experience blue and red shifts. The observed splitting depends on the observer's perspective. This is illustrated in Fig. 1.6. In the transverse Zeeman effect, where the observer views the system perpendicular to the magnetic field,

the π -component is linearly polarised parallel to \mathbf{B} , while the σ -components are linearly polarised perpendicular to \mathbf{B} . In the longitudinal Zeeman effect, only the σ -components are visible, and they are circularly polarised in opposite directions to each other.

On the Sun due to line broadening by Doppler shifts and collisions we can only observe an actual splitting of the line if the magnetic field is strong enough. This is typically the case only in sunspots. However, the different components can still be observed due to their different polarisations.

1.2.1.2 Stokes Formalism

Natural light is unpolarised. However, polarisation can occur through processes like the Zeeman effect. A mathematical representation of polarised light (see, e.g., del Toro Iniesta 2003) is the Stokes vector \mathbf{I}

$$\mathbf{I} = \begin{pmatrix} I \\ Q \\ U \\ V \end{pmatrix} = \begin{pmatrix} I_{total} \\ I_{0^\circ} - I_{90^\circ} \\ I_{45^\circ} - I_{135^\circ} \\ I_{\odot} - I_{\ominus} \end{pmatrix}. \quad (1.14)$$

Its four components, the Stokes parameters, fully describe the polarisation: I is the total intensity, Q and U describe linear polarisation in the horizontal-vertical and diagonal directions, respectively, while V represents the circular polarisation. Partially polarised light can be seen as a combination of natural and fully polarised light:

$$I = I_{natural} + I_{polarised}. \quad (1.15)$$

The degree of polarisation p is the quotient of polarised intensity and total intensity

$$p = \frac{I_{polarised}}{I} = \frac{\sqrt{Q^2 + U^2 + V^2}}{I}, \quad (1.16)$$

with $p = 0$ for natural light and $p = 1$ for fully polarised light.

1.2.1.3 Magnetographs

We rely on measurements of intensities in different polarisation states to infer information about the photospheric magnetic field (Stix 2002). A polarimeter is an instrument designed to take these measurements. In solar physics a polarimeter providing images of the solar magnetic field is referred to as a magnetograph.

It is necessary to measure the full Stokes vector \mathbf{I} to infer the full magnetic field vector \mathbf{B} . The signal in the circular polarisation is generally stronger than in linear polarisation, due to the properties of the Zeeman effect. Measuring I and V is sufficient to obtain the line of sight (LOS) component.

Since we cannot measure the magnetic field directly, we instead measure the polarisation state of the light emerging from the photosphere. To make use of these measurements, we need to model how the radiation propagates through the medium before being emitted. Following del Toro Iniesta (2003) we can describe the transport of polarised radiative energy through a medium by the radiative transfer equation

$$\frac{d\mathbf{I}}{d\tau_c} = \mathbf{K}(\mathbf{I} - \mathbf{S}). \quad (1.17)$$

Here, \mathbf{I} is the Stokes vector and τ_c the continuum optical depth along propagation direction of the ray. The optical and physical depth are connected via $d\tau_c = \kappa ds$, with the absorption coefficient for the continuum, κ , and the physical path length s . τ_c serves as a measure to determine whether a medium is opaque ($\tau_c > 1$) or transparent ($\tau_c < 1$). The propagation matrix \mathbf{K} describes the absorption, dichroism, and dispersion effects the medium has on the Stokes vector as the radiation propagates through it. It includes the absorption properties both in the spectral line and of the continuum. Further, the source function vector $\mathbf{S} = \epsilon/\kappa$ is the ratio of the emission ϵ and absorption κ in the continuum. These effects are all wavelength dependent, therefore the measured Stokes \mathbf{I} has to be treated separately for each wavelength.

A widely used atmospheric model is the Milne-Eddington atmosphere, where the absorption coefficient (included in \mathbf{K}) remains constant and \mathbf{S} varies linearly with optical depth. A model atmosphere like this is necessary to infer atmospheric parameters through inversion. The atmospheric properties are iteratively

modified until the resulting synthetic Stokes vectors align with the observed measurements. From this optimised model, parameters like the magnetic field vector \mathbf{B} , or Doppler velocities can be inferred.

1.2.2 Magnetic field extrapolations

The solar corona is dominated by the magnetic field. Understanding its processes often requires knowledge of the magnetic field's configuration. However, unlike in the photosphere, the coronal field cannot be directly inferred from measurements, and we must rely on models to determine its structure (Wiegelmann & Sakurai 2012).

Since the magnetic force is the dominant one in the corona with $\beta \ll 1$, non-magnetic forces can be neglected at the lowest order. As a consequence, the Lorentz force vanishes:

$$\mathbf{j} \times \mathbf{B} = 0. \quad (1.18)$$

In the magnetostatic approximation of Ampère's Law, the displacement current density $\mathbf{j}_d = \epsilon_0 \frac{\partial \mathbf{E}}{\partial t}$ vanishes due to the time-independence of the fields (Priest 2014). Consequently, the electric current density reduces to $\mathbf{j} = \frac{1}{\mu_0} \nabla \times \mathbf{B}$, where ϵ_0 and μ_0 denote the vacuum permittivity and permeability, respectively. By inserting the expression for the electric current density, Eq. 1.18 transforms to

$$(\nabla \times \mathbf{B}) \times \mathbf{B} = 0. \quad (1.19)$$

This equation together with the Gauss-law

$$\nabla \cdot \mathbf{B} = 0 \quad (1.20)$$

are the conditions for magnetic fields in the force-free field approximation. Eq. 1.19 can be fulfilled in two ways: either by a potential or current-free field

$$\nabla \times \mathbf{B} = 0, \quad (1.21)$$

or by a magnetic field that is parallel to \mathbf{j} :

$$\mathbf{B} \parallel \nabla \times \mathbf{B}. \quad (1.22)$$

The solution for the simplest, the current-free case, is equivalent to the solution of a Laplace equation

$$\Delta\phi = 0. \quad (1.23)$$

with the scalar potential ϕ . As described in Alissandrakis (1981), Eq. (1.23) can be solved using a Fourier transform method. In the more general case the force-free field conditions can be written as:

$$\nabla \times \mathbf{B} = \alpha\mathbf{B}, \quad (1.24)$$

$$\mathbf{B} \cdot \nabla\alpha = 0. \quad (1.25)$$

α is the force-free function. For a constant α the field becomes a linear force-free field. This can be described with the Helmholtz equation

$$\Delta\mathbf{B} + \alpha^2\mathbf{B} = 0. \quad (1.26)$$

To compute the coronal magnetic field, boundary conditions are needed. At the lower boundary, typically the LOS magnetograms from the photosphere are used as a boundary condition from which the coronal magnetic field is extrapolated. However, if the magnetogram only covers part of the photosphere, one cannot assume it to be fully flux balanced. One way to ensure flux balance is to extend the original magnetogram by its three-point mirror image (Seehafer 1978).

In the outer corona, when β reaches a value of one and higher (Gary 2001), the magnetic field lines become predominantly radial through the effect of the outflowing solar wind. In Potential Field Source Surface (PFSS) models this transition, referred to as the ‘source surface’, is typically set at 2.5 solar radii and serves as the upper boundary condition (see e.g. Schatten et al. 1969; Altschuler & Newkirk 1969). Beyond the source surface, the magnetic field is often modelled as

purely radial and can therefore be treated independently from the more complex field configuration at lower heights.

1.3 Instruments

This thesis utilises photospheric magnetic field measurements as well as coronal and chromospheric images captured by instruments aboard two spacecraft, namely Solar Orbiter (Müller et al. 2020) and the Solar Dynamics Observatory (SDO; Pesnell et al. 2012). An overview of the specific features of their missions and instruments is provided here to better contextualise their data products.

1.3.1 The Solar Orbiter Mission

Solar Orbiter, a collaborative mission between ESA and NASA, was launched in 2020 with the goal of studying the Sun at close range and in high resolution as well as from outside the ecliptic plane. Its top-level scientific questions are derived from the overarching science objective to study how the Sun creates and controls the heliosphere and understand the variability of solar activity. So far, the mission has concentrated on doing close-up observations. As it advances into a new phase of its mission, Solar Orbiter has begun to leave the ecliptic plane. It is the first spacecraft with imaging instruments to capture a view of the solar poles and will reach a heliographic latitude of 33° . Solar Orbiter travels in an elliptic orbit around the Sun so that the spatial resolution of the on-board instruments changes throughout the orbit. At perihelion it approaches the Sun as close as 0.28 AU. The spacecraft carries ten scientific instruments. Six of these are remote sensing instruments to observe the Sun and heliosphere, and the other four are in-situ instruments designed to locally measure the solar wind and heliosphere. In this work, we utilised data from two of the remote sensing instruments: the Polarimetric and Helioseismic Imager (SO/PHI; Solanki et al. 2020) and the Extreme Ultraviolet Imager (EUI; see Rochus et al. 2020).

1.3.1.1 SO/PHI

SO/PHI is a vector-magnetograph and helioseismic instrument equipped with two telescopes that can observe alternately. While for the varying distances between 0.28 and 0.91 AU the Full Disc Telescope (FDT) always sees the entire solar disc, the field of view (FOV) of the High Resolution Telescope (HRT; Gandorfer et al. 2018) is $0.28^\circ \times 0.28^\circ$. The instrument's detector measures 2048×2048 pixel and the SO/PHI-HRT has an angular sampling of $0.5''$ per pixel. At the closest perihelion distance of 0.28 AU, this plate scale corresponds to a spatial resolution (2 pixels) of approximately 200 km on the solar surface.

To obtain one data set SO/PHI records 24 images. It scans the Fe I 6173 Å photospheric absorption line at five wavelengths within the line and at one wavelength in the continuum. At each scanning position a set of the four polarisation states is recorded. After the data reduction, the continuum intensity can be directly derived from the Stokes I parameter, while the other parameters require the inversion of the radiative transfer equation. For the processing of SO/PHI data a Milne-Eddington atmosphere is assumed and the inversion yields the magnetic field vector $\mathbf{B} = (B, \gamma, \phi)$ in the photosphere, along with the LOS velocity. The magnetic field vector \mathbf{B} consists of three components B , γ , and ϕ , which correspond to the field's strength, its inclination angle relative to the LOS, and its azimuthal direction, respectively.

Due to the relatively weak fields in QS regions there are significant uncertainties in both B and γ . The LOS magnetic field $B_{\text{LOS}} = B \cos \gamma$ however is less affected because the coupling of these uncertainties leaves the B_{LOS} much less affected. This makes B_{LOS} the most reliable measurement of the magnetic field that can be derived from polarimetric data using the Zeeman splitting of spectral lines. Further details are available in Gandorfer et al. (2018), Solanki et al. (2020), and Sinjan et al. (2022).

The SO/PHI-HRT can achieve a cadence of up to 60 seconds, albeit with a reduction in signal-to-noise ratio (S/N). An optimised cadence is 76 seconds.

1.3.1.2 EUI

The EUI instrument was designed to observe the solar corona and chromosphere both at high resolution and over the entire solar disc. EUI is equipped with three different telescopes that can observe simultaneously. The Full Sun Imager (FSI) features a single telescope capable of observing different solar layers. It can capture the chromosphere and lower transition region at 304 \AA , corresponding to the formation height of the He II line. Alternatively, it observes the corona in the extreme ultraviolet (EUV) around 174 \AA , in a band that includes a prominent Fe x line which samples gas near 1 MK. The High-Resolution instruments (HRIs) can be operated simultaneously since they employ two separate telescopes. One telescope (HRI_{Ly α}) images the chromosphere in the Ly- α line of hydrogen at 1216 \AA . Like the FSI the second EUI/HRI channel (HRI_{EUV}) is centred around 174 \AA .

EUI's plate scale is $0.492''$ and the detectors of its HRI telescopes record the images with 2048×2048 pixel. As a result, the EUI/HRIs have a FOV very similar in size to the SO/PHI-HRT and at closest perihelion can achieve a resolution of ~ 200 km on the Sun.

EUI is capable of recording full images at a 1-second cadence. The images are usually compressed to account for the limited telemetry. Level 2 data products are calibrated and corrected for instrumental effects, representing the science-quality data output.

1.3.2 The Solar Dynamics Observatory

The Solar Dynamics Observatory (SDO; Pesnell et al. 2012) was launched on 2010, February 10 into a geosynchronous Earth orbit that allows for nearly continuous solar observations. It was the first mission of NASA's living with a star programme and aims at understanding solar activity and variability, as well as space weather monitoring. To achieve these goals the spacecraft carries three scientific instruments: the Helioseismic and Magnetic Imager (HMI; Schou et al. 2012), the Atmospheric Imaging Assembly (AIA; Lemen et al. 2011), and the EUV Variability Experiment (EVE). After the end of its nominal 5-year mission phase, SDO began its extended mission phase and continues to provide invaluable solar data.

1.3.2.1 SDO/HMI

SDO/HMI is designed to study the Sun's magnetic field and solar oscillations. Like SO/PHI, SDO/HMI uses the Fe I 6173 Å line to infer the Doppler shifts, the intensity, the LOS magnetic field, and the vector magnetic field in the photosphere. At six different wavelength positions around the line core all four Stokes parameters are recorded. The cadence for the vector magnetic field is 12 minutes, the other data products are provided at a cadence of 45 seconds.

Data is recorded on two 4096×4096 detectors. SDO/HMI has a plate scale of $0.505''$ (corresponding to ~ 366 km per pixel on the solar surface), and can resolve elements as small as $1''$.

1.3.2.2 SDO/AIA

SDO/AIA has ten channels to observe the Sun at different wavelengths and enables us to probe the Sun's plasma at various temperatures. Three of the channels operate in the UV and visible and see the photosphere, chromosphere and transition region, while the other seven channels observe the transition region and corona in the EUV. Among these EUV channels, one uses the He II line at 304 Å, the same as the EUV/FSI instrument, whereas each of the other six channels is primarily dominated by distinct Fe emission lines. Consequently, a channel's sensitivity to plasma at specific temperatures is determined by the Fe lines within its pass band: 94 Å (6.3 MK, Fe XVIII), 131 Å (0.4 MK and 10 MK, Fe VIII, Fe XXI), 171 Å (0.8 MK, Fe IX), 193 Å (1.6 MK and 20 MK, Fe XII and Fe XXIV), 211 Å (2.0 MK, Fe XIV), 335 Å (2.5 MK, Fe XVI).

SDO/AIA observes with a cadence of 12 seconds across all channels. Like the SDO/HMI detectors SDO/AIA's four detectors are also 4096×4096 pixels in size, with each detector handling two or more of the instrument's channels. With a plate scale of $0.6''$ (435 km/pixel) SDO/AIA has a slightly lower plate scale than SDO/HMI. For alignments, the SDO/HMI resolution is down-scaled to match that of the SDO/AIA images.

1.4 Motivation and thesis outline

Historically, the solar corona could only be observed during solar eclipses. The brightness of the solar disc overwhelms the faint coronal light, and even scattered sunlight in the daytime sky hinders us from seeing the corona outside eclipses (Aschwanden 2004). Moreover, due to the corona's high temperature, most of its radiation is in the form of X-rays and EUV radiation, which is absorbed by Earth's atmosphere, allowing only the white-light corona to be seen. While this protects life on Earth from high-energy radiation, it also complicates direct observations of the solar corona. The advent of rocket-based observations in the late 1940s enabled the first short-duration (\sim minutes) observations of the Sun in the EUV, marking the beginning of a new era in coronal studies at previously unobtainable wavelengths. With space missions such as Orbiting Solar Observatory and Skylab in the 1960s and 1970s, long-term observations of the corona became possible, paving the way for further advances in the decades that followed.

In recent years, space missions have transformed our ability to observe the solar corona. SDO has provided nearly continuous, high-cadence observations of the corona and the photospheric magnetic field for the past 15 years, making it an essential tool for solar research. This thesis makes use of SDO data but focuses primarily on observations from the Solar Orbiter mission. Since its launch in 2020, Solar Orbiter has significantly advanced the field of solar observations. Equipped with imaging instrumentation it is capable of capturing high-resolution images at high cadence around its perihelia. The SO/PHI and EU1 instruments allow for co-temporal studies of the solar magnetic field and fine-scale coronal structures, offering new insights into the Sun's dynamic processes.

In Sects. 1.1.2.2 and 1.1.4, we have introduced various phenomena associated with reduced EUV emission, including CHs, coronal dark halos, and AR outflows. Further well-known phenomena are filaments and coronal dimmings. While all of these structures exhibit reduced EUV emission, they manifest in various regions of the Sun, and their underlying formation mechanisms can differ significantly. In some cases, these mechanisms remain not fully understood.

The first project (see Chapter 3) examines small EUV-dark structures embedded in the QS, which have so far not been the subject of detailed studies. To investigate their physical nature, we formulated two competing hypotheses. One hypothesis posits that these structures could be miniature analogues of CHs and consequently be structured by an open magnetic field configuration, thus contributing to the fast solar wind. If proven correct, this interpretation could shed light on the open flux problem (Linker et al. 2017) — the discrepancy between the open magnetic flux measured at 1 AU and estimates based on solar open field regions, which are lower by a factor of 2–3. The second hypothesis proposes that coronal voids may be regions that experience less coronal heating compared to their surroundings. This could occur in magnetically closed regions that exhibit reduced levels of photospheric magnetic flux. As a result, these areas would experience reduced coronal heating, which in turn leads to a decrease in EUV emission, giving the coronal voids their noticeably darker appearance. Our analysis has verified this latter interpretation, allowing us to identify and describe a new type of structure within the QS.

The second project investigates a different class of EUV-dark structures linked to ARs (see Chapter 3). Coronal dark halos are frequently observed around ARs at temperatures below or at 1 MK. Although several models have been proposed to explain this phenomenon (see Sect. 1.1.4), none of them can provide a comprehensive explanation that fully aligns with all observed data. In this work, we take a new perspective by analysing these structures not as a whole, but in terms of their variation with distance from the AR centre. This approach enables us to assess the radial dependence of the magnetic field and of coronal plasma at different temperatures. Based on these findings, we propose an additional mechanism explaining the dark appearance of the coronal dark halos.

In conclusion, Chapter 4 outlines opportunities for broadening the scope of our investigations and what further observations are needed to advance our comprehension of these phenomena. Our next phase of research will prioritise the temporal evolution of coronal voids and coronal dark halos, an area not previously emphasised in our work. This approach aims to document how these structures dynamically evolve and potentially capture their initial formation stages.

Additionally, we provide initial findings that shed light on the temporal aspects of coronal voids, setting the stage for future detailed studies.

2. Coronal voids and their magnetic nature

This chapter is based on the paper ‘Coronal voids and their magnetic nature’ published in *Astronomy & Astrophysics* (Nölke et al. 2023). Its content was reproduced under the terms of the Creative Commons Attribution License (<https://creativecommons.org/licenses/by/4.0>).

2.1 Introduction

CHs manifest as dark patches in UV and X-ray images of the solar corona, They are structured by open magnetic fields and characterised by lower temperatures and densities compared to surrounding regions. More detailed information on CH can be found in Sect 1.1.2.2.

High-resolution EUV imaging at approximately 174 \AA , conducted with the EUVI instrument on the Solar Orbiter, has revealed dark regions embedded within the QS. These areas, referred to here as coronal voids, display a wide range of sizes, from a few granules in scale to several supergranules (up to roughly 70 Mm), making them significantly smaller than typical CHs.

Two primary hypothesis have been proposed for the nature of coronal voids. One possibility is that they represent miniature versions of CHs. Alternatively, these voids may form due to a reduction in energy input from the underlying magnetic structures rooted in the photosphere, leading to lower plasma temperatures and densities. If the latter hypothesis holds, the photospheric magnetic field within these voids should be considerably weaker than in the surrounding QS. Prior studies (Martínez González et al. 2012) have identified so-called ‘dead calm’ regions, where magnetic activity is significantly reduced, based on data from the Imaging Magnetograph eXperiment (IMaX; Martínez Pillet et al. 2011) aboard the Sunrise observatory (Solanki et al. 2010b; Barthol et al. 2011; Berkefeld et al. 2011; Gandorfer et al. 2011). Coronal voids may be the coronal counterparts

of such magnetically quiet zones.

To evaluate these possibilities, this study examines the photospheric magnetic fields underlying the coronal voids detected in EUV data. We anticipated to either detect a localised reduction of magnetic activity — similar to the dead calm regions — or an imbalance in the net flux imbalance, as typically seen in coronal holes.

2.2 Observations

During the cruise phase of Solar Orbiter on 2021 February 23rd both the SO/PHI-HRT and the EUV/HRI's captured a QS region nearly simultaneously. At the time, Solar Orbiter was positioned at 0.53 AU from the Sun, with a Solar-Orbiter–Sun–Earth angle of 142° . The instruments were aimed at the centre of the solar disc. According to the FITS headers, the image orientations for HRI_{EUV}, HRI_{Ly α} channel, and SO/PHI-HRT relative to solar north were 0.3° , 0.5° , and 0.6° , respectively. All images presented here have north approximately at the top and west to the right.

2.2.1 SO/PHI observation

The SO/PHI-HRT recorded a full-FOV observation (2048×2048 pixels) at 17:00:45 UTC (here and in the following all times are given in UTC), with an exposure duration of 86 seconds. The instrument's plate scale is $0.5''$, corresponding to 191 km per pixel at the observing distance of 0.53 AU. The B_{LOS} magnetogram used in this study is a level 2 data product that has been corrected for geometric distortions. Since the observations were taken close to the solar disc centre, the strong vertical magnetic fields ensure that B_{LOS} provides a close approximation of the true field strength.

2.2.2 EUV observations

Because of technical difficulties, the two EUV/HRI channels did not operate simultaneously. The Ly- α channel recorded a time series from 16:55:15 to 16:58:55 with a 5-second cadence, while the 174 Å channel began its observations at 17:13:25,

capturing data every 2 seconds until 17:20:59. For our analysis, we selected the $HRI_{Ly\alpha}$ and HRI_{EUV} observations that were temporally closest to the chosen SO/PHI-HRT measurement. Specifically those taken at 16:58:55 and 17:13:25, respectively. The HRI_{EUV} data have a plate scale of $0.492''$, equivalent to 188 km per pixel on the Sun at a solar distance of 0.53 AU. In contrast, the $HRI_{Ly\alpha}$ images were binned by a factor of four, resulting in a plate scale of $1.028''$, corresponding to 392 km per pixel at the same solar distance. The EUV data utilised in this study are level 2 products.¹ Kahil et al. (2022) also included this HRI_{EUV} dataset along with the SO/PHI B_{LOS} map in their analysis.

2.2.3 Alignment of PHI and EUV

Thermal variations affecting both the spacecraft and its instruments lead to shifts in alignment between different channels and instruments over time. As such, the LOS magnetogram needs to be aligned with the EUV images utilised in this study. Since the magnetic network is visible in both B_{LOS} and $HRI_{Ly\alpha}$, a good alignment is achieved by performing the shift in sequence: B_{LOS} to $HRI_{Ly\alpha}$, followed by $HRI_{Ly\alpha}$ to HRI_{EUV} . We adopted the procedure described by Kahil et al. (2022), but in addition, we adjusted the plate scale of both the B_{LOS} and $HRI_{Ly\alpha}$ data by rescaling them to match the HRI_{EUV} plate scale of $0.492''$ (188 km per pixel on the Sun at 0.53 AU). The B_{LOS} image is shifted southward relative to the HRI_{EUV} data, owing to incomplete overlap between the two instruments' FOVs. Consequently, magnetic field information is not available for roughly the upper 10% of the HRI_{EUV} image. During alignment, the $HRI_{Ly\alpha}$ was slightly shifted westwards.

2.3 Results

Our initial step involved identifying the coronal voids using an intensity threshold. We then analysed the photospheric magnetic field to evaluate both hypotheses concerning the origin of these coronal voids.

¹<https://doi.org/10.24414/2qfw-tr95>

2. Coronal voids and their magnetic nature

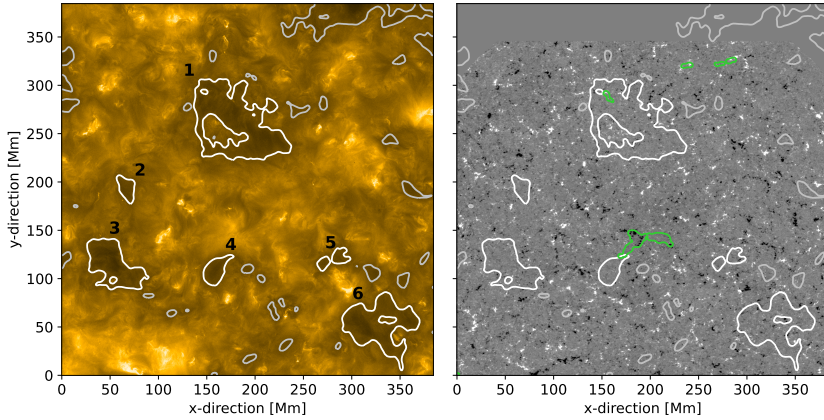


Figure 2.1: This figure provides an overview of the observations. The high-resolution images display nearly the entire FOV of EUI HRI_{EUV} (left) and SO/PHI-HRT (right), captured on 2021 February 23 at 17:13:26 and 17:00:45, respectively. The disc centre (from the perspective of Solar Orbiter) is located approximately at the centre of each image, with the north directed upwards. The coordinates are given in Mm relative to the Sun. The HRI_{EUV} image, taken at 174 Å, is presented on a linear scale, while the SO/PHI-HRT map represents the LOS magnetogram, which is saturated at ± 50 G, with white and black areas indicating positive and negative polarities, respectively. Due to a slight shift in the FOV of PHI towards the south compared to EUI, the upper portion of the magnetogram is devoid of data (appearing as flat grey). Contours in white or grey indicate EUI intensity levels at 75% of the average, highlighting the darker coronal voids observed in the HRI_{EUV}. The six prominent voids are outlined in thick white lines and numbered according to the list in Table 2.1 (refer to Sect. 2.3.1). The green contours denote the areas on the solar surface where the open field lines originate. For further discussion, see Sect. 2.3.5.

2.3.1 Defining coronal voids

The coronal voids are clearly visible with the naked eye in the HRI_{EUV} images (Fig. 2.1, left panel). To determine their extent — both in shape and size — we applied an iso-contour to a smoothed version of the intensity map. Smoothing was necessary to prevent the contours from appearing excessively jagged. For this purpose, we convolved the HRI_{EUV} image with a Gaussian kernel with a full width at half maximum (FWHM) of approximately 4 Mm, corresponding to the characteristic size of network structures visible in the QS EUV data. An intensity threshold of 75% of the mean value across the FOV was then applied.

Table 2.1: The properties of the major coronal voids and the surrounding QS are listed here for each individual structure.

Coronal void ^a	Size ^c [Mm]	Avg. coronal intensity ^d [DN/s]	$\langle B_{\text{LOS}} \rangle^e$ [G]	Imbalance in magn. flux ^f rel. δF [%]	abs. ΔF [G]
1	77	735	12.1	12.2	+1.5
2	21	756	10.1	11.3	+1.2
3	49	708	11.2	16.1	-1.8
4	26	739	9.8	26.1	-2.6
5	21	773	12.2	42.5	-5.2
6	60	741	12.0	8.2	-1.0
Surr. QS		1122	15.9	0.9	+0.1
Whole FOV		1094	15.7	1.0	+0.2

^a The outlines of the major coronal voids are shown in Fig. 2.1.

^b The surrounding QS is the whole FOV displayed in Fig. 2.1 without the major coronal voids.

^c The size is the diameter of a circle covering the same area as the void (see Sect. 2.3.1).

^d Average intensity seen by HRI_{EUV} in the 174 Å channel of EU1.

^e For the definition of $\langle |B_{\text{LOS}}| \rangle$, see Sect. 2.3.3.1.

^f Flux imbalances as defined in Eqs. 2.2 and 2.3 (see Sect. 2.3.4).

This threshold outlines the dark regions effectively, as illustrated in Fig. 2.1 (left panel), where the contour derived from the smoothed data is overlaid onto the original HRI_{EUV} image. A coronal void is defined as the area enclosed by this contour. While we tested other threshold values, the overall results remained largely consistent (see Appendix A.1 for further details). Naturally, varying the threshold affects the inferred size of the voids — with higher thresholds yielding slightly larger regions.

Overall, the coronal voids occupy roughly 10% of the entire FOV and display mean intensities between 60% and 70% of the QS level. Table 2.1 provides a detailed overview of the identified voids (labelled in Fig. 2.1) along with corresponding data for the QS.

Coronal voids come in a range of sizes and shapes. To easily compare individual structures, for instance on a supergranular scale, we characterised each void by its linear dimension as the diameter of a circle possessing the same area as the respective coronal void.

For the purpose of this study, we focused on the larger examples. We refer to voids with dimensions equal to or exceeding that of a typical supergranule (approximately 20 Mm) as major voids (Table 2.1), identifying five such structures (voids no. 1 to 4 and 6 in Fig. 2.1). We also classified void no. 5 as major, although it comprises two smaller voids situated so closely together that they nearly merge together exceeding the 20 Mm size threshold. A larger void partially visible at the upper right was excluded from the analysis, as it lies at the boundary of the EUV FOV and is not captured by SO/PHI-HRT.

Altogether, we identified six distinct major coronal voids suitable for studying their magnetic properties. Smaller dark features below the supergranular scale were not included, as they may correspond to darker inter-network regions (see the small grey outlines in Fig. 2.1).

To place the chosen threshold into perspective, we compared it with those typically used for detecting polar or equatorial CHs. Threshold values for CH identification vary depending on the plasma temperature sensitivity of the imaging channel. A common choice is the 193 Å passband of the Atmospheric Imaging Assembly on board the Solar Dynamics Observatory, which responds primarily to Fe XII emission around 1.6 MK (Lemen et al. 2011). In this channel, thresholds ranging from 35% to 40% of the median solar disc intensity are frequently applied (e.g. Hofmeister et al. 2017; Heinemann et al. 2019). For cooler plasma, as imaged in the 171 Å channel of AIA, which traces emission below 1 MK, the contrast is lower, requiring a relatively higher threshold to outline CHs (Garton et al. 2018).

In summary, the threshold applied to coronal voids is larger than typical CH definitions, yet still remains compatible with them.

2.3.2 Chromospheric counterparts of coronal voids

The Ly- α channel of EUV/HRI offers a means to examine whether coronal voids have counterparts in the chromosphere. In the upper panel of Fig. 2.2, the HRI_{Ly α} intensity map is shown with the void boundaries, as determined from the HRI_{EUV} image, overlaid. Overall, regions identified as coronal voids in the 174 Å channel also appear dimmer in Ly- α . Within these areas, only faint structures are visible in the HRI_{Ly α} image.

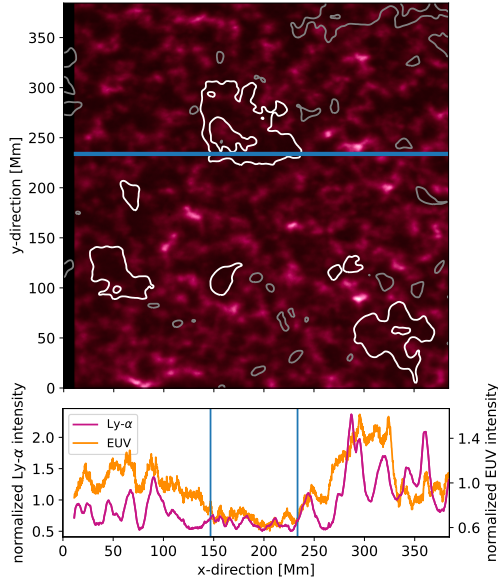


Figure 2.2: Connectivity of coronal voids to the chromosphere. The upper panel shows the region of interest in Ly- α , captured on 2021 February 23 at 16:58:55 by the HRI_{Ly α} instrument. The FOV matches that shown in Fig. 2.1 and was acquired within roughly 15 minutes of the HRI_{EUV}-snapshots displayed there. The contours tracing the coronal voids are the same as those used in Fig. 2.1. In the lower panel, a one-dimensional cut is shown along the blue line marked in the Ly- α image. This plot compares intensity profiles from the HRI_{Ly α} (red) and HRI_{EUV} (orange) channels. As a means of noise reduction, the data were averaged over 10 pixels along the y -axis. The dark coronal void appears clearly in both the Ly- α and EUV (174 Å) profiles. The part of the coronal void which was intersected by the cut is indicated by two vertical blue lines. Further details are provided in Sect. 2.3.2.

To quantify the coronal voids' reduced emission in both EUV/HRI channels, we analysed a horizontal cut through the largest void (red and orange profiles in the lower panel of Fig. 2.2 for HRI_{Ly α} and HRI_{EUV}, respectively). Prior to plotting, we averaged the data over 10 pixels along the y -axis to reduce noise. Comparable patterns were observed in the other major voids as well.

Within the coronal void, the Ly- α emission is below that in adjacent QS regions. While some weak brightness variations are present, they are considerably less pronounced than the strong fluctuations typical of the QS. Beyond

2. Coronal voids and their magnetic nature

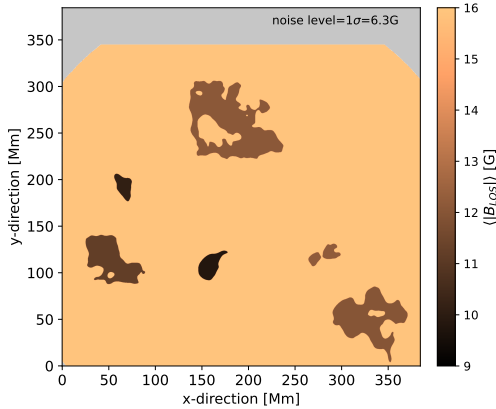


Figure 2.3: The absolute LOS magnetic field strength illustrated for the six major coronal voids and the surrounding QS. For each void, the mean value of $|B_{\text{LOS}}|$ is computed and represented as a single value positioned within the corresponding contour (We refer you also to Fig. 2.1 and Table 2.1.). The QS area is similarly coloured to reflect its $\langle |B_{\text{LOS}}| \rangle$. See Sect. 2.3.3.1 for further details.

the boundaries of the void, the brightest Ly- α features align with the magnetic network, consistent with the expected correlation between magnetic flux and chromospheric Ly- α emission. In contrast, within the voids there is little indication of prominent magnetic network elements (see Sect. 2.3.3), and it seems unlikely that the slight enhancements in Ly- α emission observed there are related to such structures.

2.3.3 Photospheric magnetic field

To assess whether the reduced EUV emission within the coronal voids could be linked to reduced heating caused by weaker magnetic fields in the photosphere, we examined B_{LOS} map recorded with SO/PHI-HRT.

2.3.3.1 Magnetic field in coronal voids and in the QS

To determine the mean unsigned LOS magnetic field in both the major coronal voids and the surrounding QS, we followed a multi-step procedure. First, the outlines of the voids were projected onto the B_{LOS} map. We then calculated the

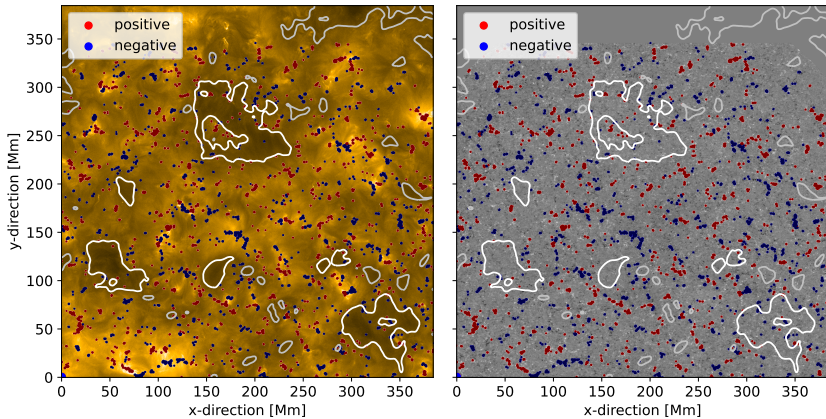


Figure 2.4: Strong-field regions highlighted for the full FOV to indicate differences between the voids and QS. The background images are identical to those in Fig. 2.1: the HRI_{EUV} channel showing the solar corona in its 174 Å passband (left) and the SO/PHI-HRT B_{LOS} map (right). To highlight areas of strong magnetic field, regions exceeding ± 50 G are indicated in red (positive polarity) and blue (negative polarity). See Sect. 2.3.3.2 for further discussion.

absolute value of B_{LOS} at all locations where the signal exceeds the noise level threshold of $1\sigma = 6.3$ G (Sinjan et al. 2022). The mean was then taken over each selected region, i.e. either an individual void or the surrounding QS.

Fig. 2.3 visualises these results by assigning the respective average value to the entire area covered by a structure (individual coronal void or the QS). All values are also provided in Table 2.1.

The range of $\langle |B_{\text{LOS}}| \rangle$ values inside the coronal voids lies between 9.8 and 12.2 G, while we derive a value of 15.9 G for the QS. This means that the photospheric magnetic field in the voids is, on average, by a factor of 1.3 to 1.6 weaker compared to the QS. Consequently, the coronal voids exhibit a consistently weaker photospheric magnetic flux compared to the QS surrounding them.

2.3.3.2 Strong magnetic fields avoid coronal voids

Inside the coronal voids, pixels exhibiting stronger $|B_{\text{LOS}}|$ values occur far less frequently than in the surrounding QS. This is illustrated in Fig. 2.4, where regions

2. Coronal voids and their magnetic nature

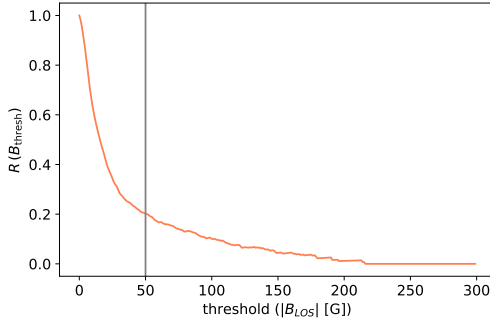


Figure 2.5: Ratio, R , of areas of voids to QS that have $|B_{\text{LOS}}|$ values exceeding a specified threshold in $|B_{\text{LOS}}|$, plotted as a function of this threshold. The area ratio is normalised to reach unity as $|B_{\text{LOS}}|$ approaches zero (see Eq. 2.1). The vertical line indicates the distribution of pixels at 50 G, as shown in Fig. 2.4.

with $|B_{\text{LOS}}| > 50$ G are highlighted by colour both in the HRI_{EUV} image and on the B_{LOS} map. It can clearly be seen that only a few such strong-field patches are present inside the voids. Moreover, the few strong magnetic concentrations found within the voids tend to be smaller in size compared to those in the QS. This suggests that the magnetic network is either significantly weakened or completely absent in these regions.

In a next step, we quantified how the area covered by magnetic fields of varying strengths differs between the coronal voids and the QS. To accomplish this, we counted the number of pixels with an absolute LOS magnetic field strength, $|B_{\text{LOS}}|$, exceeding a given threshold B_{thresh} . This calculation was performed separately for the combined set of six major voids and for the QS region excluding these voids. This ratio represents the fraction of area within the voids covered by magnetic fields above B_{thresh} , relative to the corresponding area in the QS. To account for the overall area-size difference between voids and QS, we normalised this ratio by its value at $B_{\text{thresh}}=0$ G, denoted as R_0 , which simply corresponds to the area ratio of voids to QS. Thus, a normalised area ratio for pixels exceeding

the threshold B_{thresh} is defined as

$$R(B_{\text{thresh}}) = \frac{1}{R_0} \frac{\sum \text{pixels in voids } (|B_{\text{LOS}}| > B_{\text{thresh}})}{\sum \text{pixels in QS } (|B_{\text{LOS}}| > B_{\text{thresh}})}. \quad (2.1)$$

We computed this ratio across a range of B_{thresh} values from 0 to 300 G, and present the result in Fig. 2.5.

As the threshold B_{thresh} increases, the area fraction in the voids covered by magnetic fields above this threshold declines rapidly. At $B_{\text{thresh}} = 50$ G, the normalised area ratio has already fallen to roughly one-fifth (see the vertical line in Fig. 2.5). This means that, for equally sized regions, the QS contains about five times more pixels with $|B_{\text{LOS}}|$ above 50 G than the voids do. Above the threshold of 200 G, the ratio R drops to zero, indicating that no pixels inside the coronal voids display $|B_{\text{LOS}}|$ values at or above this strength, while such strong-field pixels are still present in the QS. These observations demonstrate that, within coronal voids, the magnetic field is not only weak on average but it also characterised by a significantly low number of regions with strong LOS field strength.

The difference in distribution of stronger magnetic fields in the coronal voids and the QS is apparent in a double-logarithmic histogram of $|B_{\text{LOS}}|$ (equally spaced in $\log(|B_{\text{LOS}}|)$ were used that have a width of 0.05; this is shown on the right panel in Fig. 2.6). We created one histogram combining all coronal voids (i.e. one histogram represents all voids) and another for the QS (i.e. the full FOV excluding the voids). Both histograms follow a power-law trend; however, the voids' histogram declines with a much steeper slope. This indicates that the number of pixels with strong magnetic fields falls off much more rapidly in the voids than in the QS., visualising the significantly lower spatial density of strong-field patches in the voids compared to the QS.

Given that the QS covers a considerably larger area than the voids, small sub-regions within the QS might also exhibit a low density of strong-field patches. To assess this, we constructed histograms for three QS regions, each approximately the size of the largest void. These regions, randomly selected and marked as rectangles 1 to 3 in the left panel of Fig. 2.6, display power-law distributions nearly identical to that of the entire QS. This confirms that the observed differences

between the voids' and QS's histograms are intrinsic and not merely a result of the different area sizes.

To further investigate the distribution of $\langle |B_{\text{LOS}}| \rangle$ within areas of the QS, we divided the QS portion of the full FOV into a grid of square tiles, each approximately matching the size of a coronal void. Within each tile, we computed the mean of the absolute LOS magnetic field, considering only pixels above the noise threshold of 1σ . To improve the statistical robustness by increasing the number of samples, we allowed the tiles to overlap, shifting them by 5 Mm between placements. This analysis was performed using two tile sizes: one corresponding to the smallest major void (20 Mm diameter, yielding a square with side length $\sqrt{\pi}/2 \times 20$ Mm), and another matching the extent of the largest void (77 Mm). From these, we generated two separate histograms of the $\langle |B_{\text{LOS}}| \rangle$ for each tile size sample, which were then compared with the values calculated for the major coronal voids (see Fig. 2.7). These results highlight a noticeable difference: all major voids exhibit $\langle |B_{\text{LOS}}| \rangle$ values lower than those typically found in the QS. In fact, they appear at the lower end of the QS histograms, reinforcing the conclusion that regions with strong magnetic fields tend to be located outside the coronal voids.

2.3.3.3 Weak magnetic fields define coronal voids

Having established in Sect. 2.3.3.2 that coronal voids are areas with reduced magnetic activity, we now investigate whether all regions with weak magnetic fields are associated with coronal voids. The magnetic field in the QS typically appears as a small-scale salt-and-pepper pattern. To focus on larger-scale trends, we used the unsigned LOS magnetic field, $|B_{\text{LOS}}|$, and applied spatial averaging to suppress local noise. Since the major voids we were studying span at least 20 Mm (cf. Table 2.1), we smoothed the $|B_{\text{LOS}}|$ map using a Gaussian kernel with a full width at half maximum of about 20 Mm (115 pixels). The resulting smoothed map is shown in Fig. 2.8. Naturally, the smoothing reduces the field strengths in this version of the map compared to the original data shown in, for example, Figs. 2.5 and 2.6. The smoothed map reveals that many weak-field regions coincide with the locations of coronal voids. In Fig. 2.8, the major voids

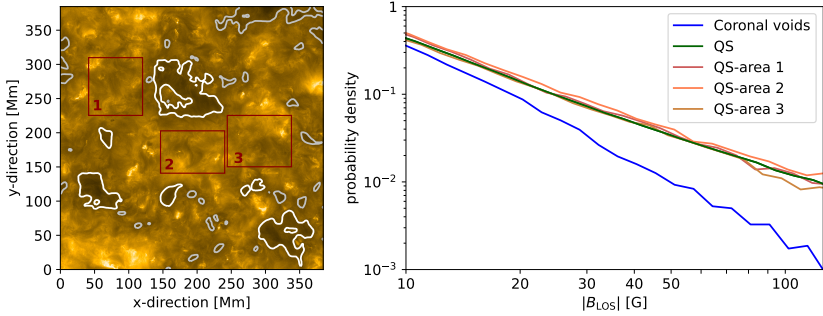


Figure 2.6: Histograms of $|B_{\text{LOS}}|$ in coronal voids and in the QS. The HRI_{EUV} image is shown in the left panel, similar to Fig. 2.1, the regions of interest for which the $|B_{\text{LOS}}|$ histograms—displayed here—were derived (right panel) are indicated here. The combined histogram for all major voids is represented by the blue line (the voids are outlined by thick white contours in the left panel). The red, orange, and brown curves correspond to the three rectangular regions within the QS, each covering a different small subsection of the QS. The green curve shows the histogram for the entire FOV, excluding the major voids. See Sect. 2.3.3.2.

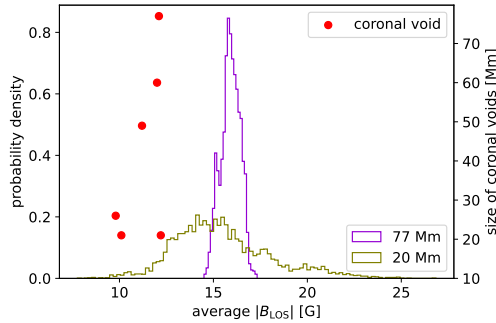


Figure 2.7: Distribution of $\langle |B_{\text{LOS}}| \rangle$ in QS areas. The QS portion of the whole FOV is sub-divided into uniform tiles, and the $\langle |B_{\text{LOS}}| \rangle$ is computed for each tile. Histograms of these mean values are displayed in olive and purple for tile sizes corresponding to 20 and 77 Mm, respectively. Red dots indicate the $\langle |B_{\text{LOS}}| \rangle$ values for the six major coronal voids (cf. Table 2.1), plotted as a function of void size on the right-hand axis. See Sect. 2.3.3.2.

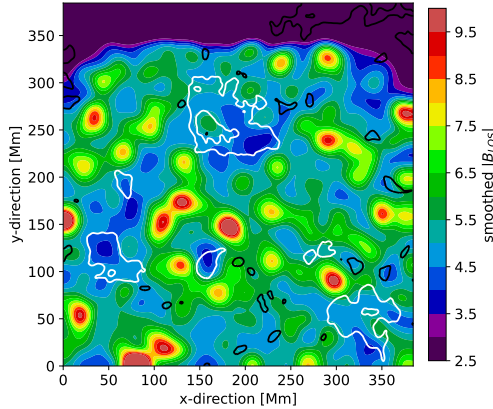


Figure 2.8: Coronal voids and weak magnetic fields. To visualise areas with reduced magnetic field, we applied a Gaussian kernel with a FWHM of 20 Mm to smooth the $|B_{\text{LOS}}|$ map. By using a discrete colour scale structural patterns are emphasised. Regions dominated by weaker fields appear primarily in blue. Contours outlining the coronal voids are overlaid: the six major voids listed in Table 2.1 are shown with thick white outlines, while smaller voids are indicated in black using the same contours shown in Fig. 2.1. See Sect. 2.3.3.3.

overlap with the larger low-field patches, shown in dark to light blue. Most of the remaining weak-field areas are covered by smaller coronal voids (sizes below 20 Mm) which are outlined in black. However, there are some weak-field regions where no coronal void is present, neither large nor small. Examples include a patch around $x=80$ Mm and $y=170$ Mm, as well as an area near the lower-left corner of the FOV in Fig. 2.8. In these and similar cases, it appears that coronal loops reach over the weak-field areas connecting magnetic patches of opposite polarity on either side of the weak-field areas. As a result, coronal voids do not form in these regions due to the overlaying brighter coronal structures.

2.3.4 Flux imbalance

To explore whether coronal voids might represent miniaturised versions of CHs, we assessed the degree of magnetic flux imbalance within each void and compared these values to those observed in actual CHs. A substantial imbalance in

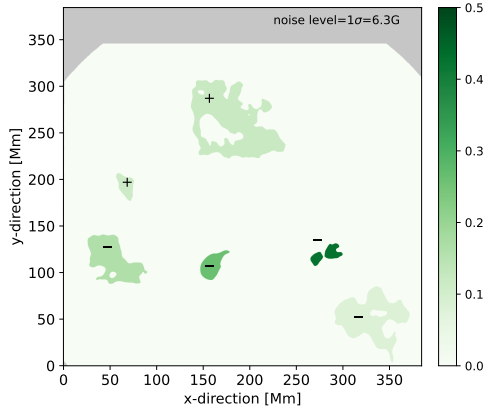


Figure 2.9: The relative magnetic flux imbalance illustrated for the major coronal voids and the QS. For each of the six major voids, the relative flux imbalance, as defined in Eq. 2.2, was calculated and plotted as a single representative value placed inside the corresponding contour (see also Fig. 2.1 and Table 2.1). The + and – symbols, positioned on or near each void, indicate the void’s dominant magnetic polarity. The QS region is also coloured according to its (negligible) flux imbalance. See Sect. 2.3.4.

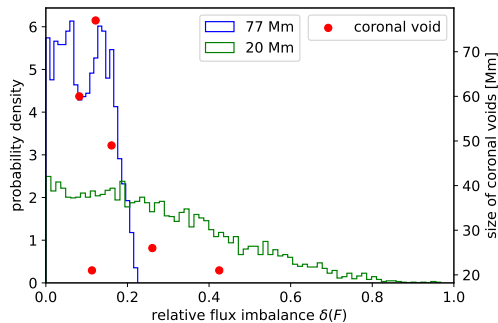


Figure 2.10: Distribution of relative flux imbalance in QS areas. The QS region of the entire FOV is sub-divided into uniform tiles, and the relative flux imbalance in each tile is computed using Eq. 2.2. Histograms of these imbalance values are shown in blue and green for tile sizes corresponding to 77 and 20 Mm, respectively. Red dots indicate the flux imbalances of the six major coronal voids (cf. Table 2.1), plotted as a function of their size along the right-hand axis. See Sect. 2.3.4.

magnetic flux is a necessary condition for drawing such an analogy. A further step would involve evaluating whether the magnetic fields in the voids are open or reconnect with other areas, such as other coronal voids or QS regions.

We defined the relative magnetic flux imbalance as the ratio between the absolute value of the averaged B_{LOS} and the average of the absolute B_{LOS} values,

$$\delta F = \frac{|\langle B_{\text{LOS},t} \rangle|}{\langle |B_{\text{LOS},t}| \rangle}, \quad (2.2)$$

where the brackets $\langle \dots \rangle$ denote spatial averaging and $B_{\text{LOS},t}$ refers to B_{LOS} values exceeding a threshold. We adopted a threshold of 6.3 G, following Sinjan et al. (2022), to mitigate the impact of noise. We computed this relative imbalance, δF , for each major coronal void individually, as well as for the QS excluding these voids. The results are shown in Fig. 2.9, with corresponding values listed in Table 2.1. Across the voids, δF ranges from about 10% to 25% (see Table 2.1), with one outlier of approximately 40% by the smallest void (number 5). In contrast, the flux imbalance in the QS is negligible at around 1% or less. Although the measured imbalances in the voids appear significant, they are still clearly smaller than those observed in low-latitude CHs, where Wiegelmann & Solanki (2004) and Hofmeister et al. (2017) reported net flux imbalances of $77\% \pm 14\%$ and $49\% \pm 16\%$, respectively.

To better assess how significant these results are, we also calculated the absolute magnetic flux imbalance, defined as the mean B_{LOS} computed over all values above the noise threshold within a given area:

$$\Delta F = \langle B_{\text{LOS},t} \rangle. \quad (2.3)$$

The corresponding values for both the major voids and the QS are also included in Table 2.1. As expected, the full FOV of the this QS observation, spanning nearly 400×400 Mm, is essentially flux balanced. In contrast, the absolute flux imbalance ΔF within the major voids ranges from about 1 to 2 G, with void 5 again standing out at around 5 G. These values, like the relative ones, remain considerably lower than those found in CHs (e.g. 7.6 G in Wiegelmann & Solanki

2004).

Different voids have different magnetic polarities which is indicated by the sign of ΔF (cf. Table 2.1). The lack of a common polarity suggests that the magnetic fields of different voids are not part of a larger coherent open-field structure that could, collectively, connect to the solar wind.

It is also possible that the flux imbalances observed in the major voids arise from their relatively small sizes, which limits statistical sampling of magnetic patches. While the overall QS (excluding the major voids) is nearly flux-balanced, it also spans more than ten times the area of all six major voids combined. To evaluate whether the imbalances found in the voids are significant or simply reflect statistical variation, we compared them with flux imbalances in smaller QS regions of similar size.

For this purpose, following the approach used in Sect. 2.3.3.2, we sub-divided the QS into square tiles with areas equivalent to those of the voids. We calculated the relative flux imbalance in each tile, and then created histograms of these values for two tile sizes, one matching the smallest void (20 Mm diameter) and one corresponding to the largest (77 Mm). Consistent with the earlier approach, we permitted an overlap between tiles by offsetting them by 5 Mm.

In the histogram derived from the smaller tiles (equivalent to a void size of 20 Mm), relative flux imbalance values reach as high as 0.8, whereas the histogram for the larger tiles (77 Mm) only extends up to about 0.2 (The histograms illustrating this are shown in Fig. 2.10). This is in line with expectations: the larger the sampled QS region, and the more balanced the magnetic flux becomes on average. Most of the flux imbalance values measured in the major voids fall within the range defined by the 77 Mm QS tiles. The two smallest voids fall outside that range, but lie well within the distribution associated with the 20 Mm tiles.

These findings suggest that the flux imbalances observed in the major voids are in line with those found in QS regions of similar size. Accordingly, our data do not indicate any significant flux imbalance in the major voids; their values remain fully consistent with those observed in the QS.

2. Coronal voids and their magnetic nature

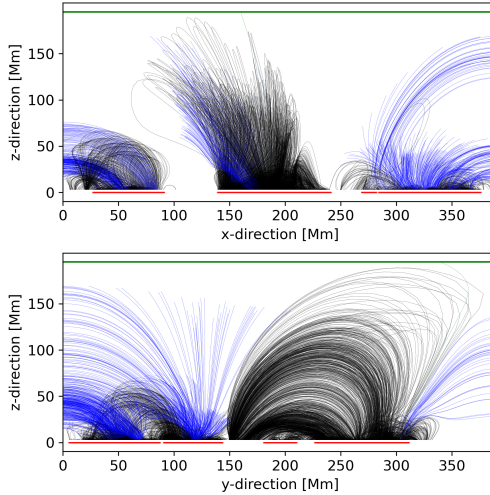


Figure 2.11: Magnetic field lines traced using a potential field extrapolation. The seeds for the field lines were placed in a regularly spaced horizontal grid (2-pixel spacing) positioned 2 Mm above the photosphere, but only from points located within coronal voids (although the field lines may connect to footpoints outside the voids). For image clarity, only every tenth field line is shown. The lines are projected onto the $x - z$ and $y - z$ planes. The field lines that extend to the top boundary, reach the side boundaries of the simulation box, or return to the solar surface are coloured green, blue, and black, respectively. The upper boundary of the simulation box is indicated by a horizontal green line, while the red marks along the bottom of both panels show the positions of the coronal voids.

2.3.5 Magnetic field extrapolation

In order to further distinguish coronal voids from CHs, we computed a potential field with the original magnetogram as the lower boundary condition. The top boundary of the simulation box was set at 195 Mm. This corresponds to a horizontal span of 1023 pixels. Within the limitations of our model, field lines that reach this height are regarded as open. The potential field equations were solved using a fast Fourier transform method, following the procedure of Alissandrakis (1981); for more details on the method see also Sect. 1.2.2. Since the original HRT magnetogram does not exhibit global flux balance, we adopted a method similar to that of Seehafer (1978). Specifically, we created a flux-balanced magnetogram

by extending the B_{LOS} map by its three-point mirror images before applying the fast Fourier method.

We started from the seed points located exclusively above the voids at 2 Mm height (placed in both x and y directions at every second horizontal grid point). From there the field lines were traced yielding nearly 75,000 field lines in total.

Only 0.007% of the traced field lines, which is equivalent to just five field lines, reach the upper boundary of the simulation domain at 195 Mm (see Fig. 2.11). The vast majority of field lines either close within a single void or extend from a void to the photosphere in surrounding QS regions. No field lines were found to connecting two voids of opposite net magnetic polarity. Some field lines exit the simulation box at the lateral boundaries; however, since this behaviour may be affected by the three-point mirroring used in setting the boundary conditions, no conclusions can be drawn from these cases. A magnetogram covering a substantially larger FOV would be needed for that.

We examined the origin of the field lines that reach the upper simulation boundary at 195 Mm in more detail (considering both those that emerge from the voids and the QS). While field lines that extend to this height are considered open in our model, this does not necessarily imply they are truly open, as they could still reconnect beyond the limits of the simulation box. To investigate the connectivity of these ‘open’ field lines, we placed seed points across the entire upper boundary, spaced every fifth horizontal grid point, and traced the field lines downward to their footpoints in the photosphere. Over 83% of these field lines originate from a prominent flux concentration located near $x=200$, $y=140$ at the centre of the FOV (see green contours in Fig. 2.1). A further 15% are traced back to QS regions in the upper right of the magnetogram. Fewer than 2% originate within the largest coronal void, around $x=160$, $y=280$ in Fig. 2.1. However, even these few field lines are rooted in a stronger magnetic concentration adjacent to an EUV-bright structure at the void’s boundary. Based on this analysis, we conclude that the coronal voids have a closed magnetic configuration, distinguishing them from CHs, which are generally dominated by open magnetic fields at coronal heights.

2.4 Discussion and conclusions

We identified regions in HRI_{EUV} images (which are sampled around the wavelength of 174 \AA) of the QS that appear significantly darker than their surroundings. These regions, which we refer to as ‘coronal voids’, are clearly outlined by an iso-contour set at 75% of the average QS intensity in this 174 \AA channel (see Sect. 2.3.1). The $\text{Ly-}\alpha$ emission, originating from chromospheric heights, is also reduced within these voids (Sect. 2.3.2). The voids identified in our dataset span sizes on the order of one to several supergranular cells. A previous study by November & Koutchmy (1996) reported dark thread-like features that were projected against coronal loops near the limb. However, any potential connection between those dark threads and the coronal voids analysed here remains unclear, particularly given that the dark threads appear to be notably smaller in extent.

We began our investigation with two working hypotheses to explain the reduced EUV brightness in the coronal voids: (1) The underlying magnetic field in the photosphere is weaker, leading to reduced magnetic heating, which in turn results in lower coronal temperatures, densities, and hence emission relative to the QS; (2) The voids represent miniaturised versions of CHs, with open magnetic field structures sustained by a notable flux imbalance in the underlying magnetic field.

Our results show that the mean unsigned LOS magnetic field strength, $|B_{\text{LOS}}|$, derived within the coronal voids is lower by a factor of 1.3 to 1.6 compared to the surrounding QS (see Sect. 2.3.3.1). Equally notable is the near absence of strong magnetic field concentrations in the major voids, even though these features are abundant throughout the QS network (Sect. 2.3.3.2). In addition, many areas with weak average magnetic fields are spatially associated with both large and small coronal voids (Sect. 2.3.3.3). Collectively, these findings indicate that the magnetic activity beneath and within the voids is significantly reduced.

As a consequence, the magnetic energy transported into the upper atmosphere above these regions is also reduced, resulting in lower heating rates in both the chromosphere and corona when compared to the surrounding QS. According to established scaling laws (Rosner et al. 1978), this reduced energy

input leads to lower temperatures and densities, and, therefore, to a decrease in coronal emission (Zhuleku et al. 2020). See Sect. 1.1.3.1 for more background on this.

We detect a certain degree of magnetic flux imbalance within the coronal voids. Although this imbalance is significantly smaller than what has been reported for CHs, it is nonetheless present (Sect. 2.3.4). This raises the possibility that, similar to CHs, the reduced coronal emission in the voids might be linked to a flux imbalance, which could indicate the presence of open magnetic field lines. If so, part of the magnetic energy could be diverted into accelerating plasma away from the Sun, thereby reducing the energy available for local heating of gas. As a result, this would lead to a reduction in coronal temperature, density and emission compared to the surrounding QS. However, further analyses revealed that the levels of flux imbalance observed in the voids are comparable to those found in QS regions of similar size. On this basis, we consider the imbalance detected in the voids to be insignificant. In addition, potential field extrapolation shows no evidence for open field structures originating from within the voids. Taken together, these results suggest that coronal voids are unlikely to represent small-scale counterparts of CHs.

To strengthen our conclusions, future observations of more coronal voids combining coronal imaging with spectroscopic measurements would be valuable. Measuring Doppler shifts within the voids and comparing them with those in the surrounding QS could help determine whether outflows, similar to those observed in CHs, are present in these regions.

Expanded observational coverage of the QS would also be highly beneficial. A larger dataset would improve statistics on the properties of coronal voids, including the distribution in flux imbalance and the with voids associated reduction in magnetic flux.

Tracking the evolution of individual coronal voids over periods ranging from several hours to a few days could reveal how stable they are, and shed light on their lifetimes. Furthermore, coordinated observations involving other instruments, such as SDO/AIA, would enable the exploration of coronal voids across a broader range of coronal temperatures.

2. Coronal voids and their magnetic nature

In summary, by combining observations from EUI and SO/PHI, we have identified coronal voids, regions that appear darker in the QS corona and are linked to unusually low magnetic flux densities. This implies that a decreased supply of magnetic energy to the coronal plasma is the main reason for the reduced brightness in these regions. Overall, our findings indicate that coronal voids are not simply miniature versions of CHs, but rather represent a separate class of coronal structures with a distinct physical origin.

3. Magnetic structure of coronal dark halos

3.1 Introduction

When observed at low coronal temperatures around or below 1 MK, AR are often surrounded by extended regions of significantly reduced emission compared to the QS. These dim regions are called coronal dark halos, but are sometimes also referred to by different names. For further details on coronal dark halos as well as similar-looking but distinct features see Sect. 1.1.4 of the introduction.

Our study focuses on examining the magnetic field and coronal emission of the dark halos, specifically exploring their correlation with distance from the AR centre. We aim to understand how the magnetic field inside the dark halos is structured and how the large-scale field of the AR facilitates the formation of these dark halos. Additionally, we compare our findings on the dark halos with those of CHs and coronal voids.

3.2 Observations

A cross-calibration campaign for Solar Orbiter with observatories in Earth orbit was performed during the mission's cruise phase on 2021 November 5. At this time Solar Orbiter was almost in the Sun–Earth line, with an angle of only 0.57° and the distance to the Sun measured 0.86 AU. Solar Orbiter was pointing at solar disc centre. SO/PHI-HRT and EUV observed at several times during this day. In this study we consider the periods that contain co-temporal observations from both instruments. Because of the advantageous orbit position we complemented the Solar Orbiter data with observations from AIA onboard SDO.

3. Magnetic structure of coronal dark halos

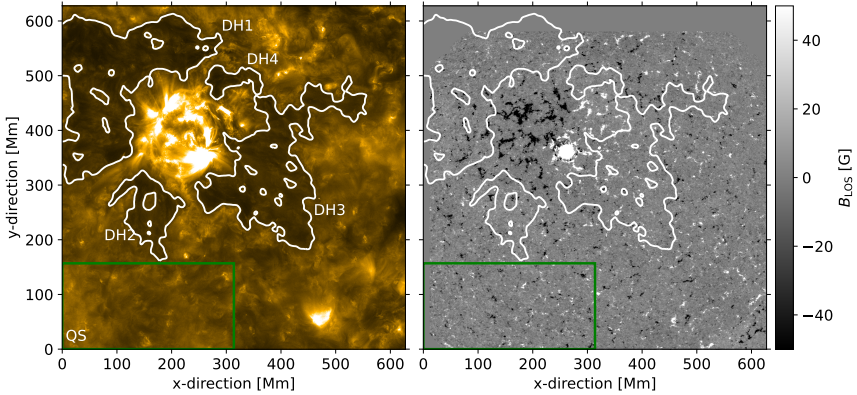


Figure 3.1: The HRI_{EUV}-image (left) and SO/PHI-HRT-magnetogram (right) taken 2021 November 5 at 23:00. The 75% intensity contours of the dark halo are plotted in white on the HRI_{EUV}-image and are projected onto the SO/PHI-HRT's B_{LOS} -map. The individual dark halo patches are labelled in white on the HRI_{EUV} image. The green rectangle on the bottom indicates the area of the reference QS.

3.2.1 Photospheric magnetic field observed with SO/PHI

The SO/PHI-HRT instrument observed between 22:46 and 23:34 with a cadence of 2.5 minutes. In this study we used a single magnetogram. The SO/PHI spectral scan to obtain this magnetogram was started at 23:29:35 and its total duration was 66 seconds. At the observing distance of 0.86 AU SO/PHI-HRT's plate scale of $0.5''$ corresponds to 311 km/pixel on the solar surface. The LOS magnetogram we used is a level 2 data product and shows the full FOV of 2048×2048 pixels.

3.2.2 Coronal observations with EUV and SDO/AIA

EUV's high-resolution telescope in the EUV (HRI_{EUV}) observed between 22:58 and 23:59 with a cadence of 5 seconds. We chose a snapshot at 23:30:00 with an exposure time of 2.8 s that was taken around mid-observation of the SO/PHI-HRT magnetogram. Like SO/PHI-HRT the HRI_{EUV} records 2048×2048 pixels. With its slightly different plate scale of $0.492''$ each pixel corresponds to 307 km/pixel on the Sun at the observing distance. HRI_{EUV}'s FOV, therefore,

covered 629×629 Mm. We used level 2 data.¹

The observation time at 23:30:00 onboard Solar Orbiter corresponds to an observation time on Earth of 23:31:07 due to the different light travel times. Hence, for our analysis we selected observations taken at this time from three different SDO/AIA passbands: 171 Å, 193 Å, and 211 Å. For the 171 Å and the 193 Å channels observations at 23:31:09 and at 23:31:04, respectively, are used. To reduce the noise level in the 211 Å channel we averaged five images, spanning one minute, around 23:31 (from 23:30:31 to 23:31:21). To study structural details we produced contrast enhanced images. Creating a contrast enhanced image requires a very an image with a very high S/N. This was achieved by averaging a time series of 30 minutes (~ 180 images) for each of the three channels. Specifically, we averaged data around 23:31 that had been corrected for solar rotation. We produced level 1.5 data and additionally normalised the data to the exposure time. Therefore, intensities for each pixel are given in the same unit DN/s as the level 2 HRI_{EUV} intensities.

3.2.3 Spatial alignment of the different data sets

Since EUI has different telescopes for each of the two high-resolution channels in the EUV and in the Lyman-alpha line, the HRI_{EUV} and the $\text{HRI}_{\text{Ly}\alpha}$, it can obtain simultaneous observations for the different channels. As described in Nölke et al. (2023) and Kahil et al. (2022) we aligned the SO/PHI-HRT LOS magnetogram to $\text{HRI}_{\text{Ly}\alpha}$ because the magnetic or chromospheric network is visible in both, and then we aligned $\text{HRI}_{\text{Ly}\alpha}$ with HRI_{EUV} . Unlike in Nölke et al. (2023) and Kahil et al. (2022) we did not apply a geometric distortion correction to the B_{LOS} map because it did not noticeably improve the data quality. To remove bad pixels a binary mask was applied to the B_{LOS} map and we additionally removed faulty pixels within two small squares at the right and left upper boundaries of the FOV. In the alignment process all data were re-scaled to the HRI_{EUV} plate scale and later cropped to the HRI_{EUV} FOV. As a result of this alignment, the B_{LOS} map needed to be shifted in the south-east direction and hence no magnetic field data is available in the upper part of the EUI FOV.

¹<https://doi.org/10.24414/z818-4163>

To align the SDO/AIA data with the HRI_{EUV} observation, we first re-projected the SDO/AIA observations using the SunPy routine (The SunPy Community et al. 2020). The rotation of the HRI_{EUV} image against the solar north and hence also between the HRI_{EUV} and SDO/AIA 171 Å image was 21.5°. Next, we correlated the re-projected 171 Å image with the HRI_{EUV} image and corrected all re-projected data for this small remaining shift.

3.3 Methods

3.3.1 Defining the dark halo boundaries

The Solar Orbiter HRI_{EUV} channel observed an area of 650×650 Mm at disc centre. Within this FOV the AR NOAA 12893 can be seen in the upper part, while the lower part shows a QS area. We define the area of the left bottom quarter below $y = 157$ Mm and left of $x = 314$ Mm as our reference QS (see Fig. 3.1). We chose this area because it is the largest connected QS areas within the FOV. We further sought to ensure that we did not include any non-QS structures: On the right an on-disc CH is present (see Fig. 3.2) and the bottom right contains a strong bipolar region which harbours a small pore.

We defined the threshold for the dark halo the same way as the threshold for coronal voids (Nölke et al. 2023): 75% of the mean QS intensity. Since we selected a QS area that exhibits a roughly symmetrical distribution of its EUV-intensities, the mean and median value do not differ greatly.

To obtain smooth iso-contours, we convolved the HRI_{EUV}-image with a Gaussian kernel with a FWHM of 7.2 Mm (corresponding to a σ of 3 Mm or 10 pixels). We then applied the intensity threshold of 75% of the mean QS intensity to this convolved image. The dark halo was identified as the EUV-dark areas surrounding the AR. We varied the threshold slightly to test for its robustness and found that our results remain consistent against small changes. Fig. 3.1 shows the HRI_{EUV}-image and SO/PHI-HRT magnetogram. The contours of the dark halo patches have been projected onto both images.

3.3.2 Determining the AR's magnetic centre and creating ring plots

Since the dark halos form in proximity to ARs it is plausible to assume that a dark halo is not uniform throughout its entire structure. Therefore, to see how the properties of the dark halo are correlated with distance to the AR, we derived these values inside concentric rings around the AR.

First, we determined the magnetic centre of the AR which is used as the centre of the rings. Here we used the geometric centre or centroid which is calculated as the average position of the pixels, treating each pixel equally by considering only their coordinates and not the pixel values. This is achieved by calculating the geometric centre of all pixels with a field strength $|B|$ of at least 100 G within 215 Mm (700 pixels) around the AR. We started at the clearly visible leading sunspot and iterated several times until the derived centre did not change any more. Next, concentric rings were drawn around this centre starting roughly at the inner boundaries of the dark halo at 92 Mm (300 pixels) distance to this centre. The rings have a width of 15 Mm (50 pixels) each on the HRI_{EUV}-image to which we have geometrically re-scaled all other images. An example of the EUV brightness in the set of rings can be seen in Fig. 3.3 for the average intensities of the HRI_{EUV}-image. Within each ring the average intensity or unsigned magnetic field was calculated either purely as a function of distance, not differentiating between individual dark halo patches, or for an individual dark halo patch, or for the brighter areas in-between the dark halo patches. For the dark halo the innermost and outermost rings are slightly larger to fully encompass the inner and outer edges of the dark halo.

3.4 Results

In this section we study the coronal emission and unsigned magnetic field of the coronal dark halo and the brighter areas in-between, as well as individual dark halo patches including a dark halo patch which overlaps with an equatorial CH. We determine how these properties behave as a function of distance to the AR.

3. Magnetic structure of coronal dark halos

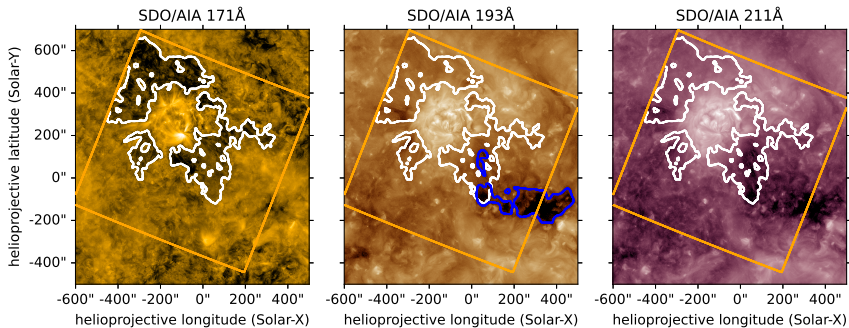


Figure 3.2: The EUV emissions for three different SDO/AIA passbands: 171 Å (left), 193 Å (middle), and 211 Å (right). The contours of the dark halo (white) have been projected onto each of the images and the orange square shows the FOV of the HRI_{EUV} observation. In the 193 Å image we also show the extent of the equatorial CH (blue) derived by an intensity-threshold of 40% of the channels mean disc-intensity.

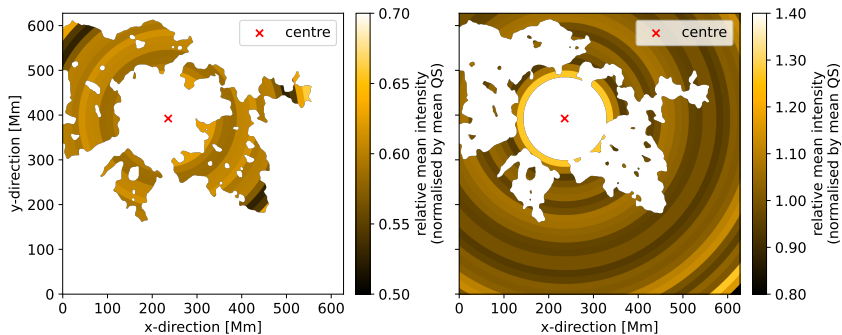


Figure 3.3: The relative mean HRI_{EUV}-intensity inside rings around the AR. The mean intensity has been normalised by the mean value of the reference QS. The panels on the left and on the right show the relative mean intensity inside the dark halo (i.e., we averaged over all dark halo patches at a certain distance to the AR and do not treat them separately) and for the brighter areas in-between the dark halo, respectively. Please note the different colour tables used for the dark halo (left) and the brighter regions between the dark halo (right).

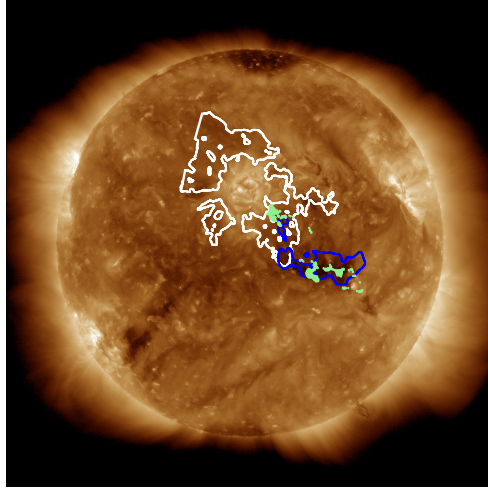


Figure 3.4: Open magnetic field originating from the CH adjacent to the AR (blue contours), including from within the dark halo patch DH3 (white contours). The image shows the SDO/AIA 193 Å channel on 2021 November 6 12:00 with the footpoints of open field lines in green.

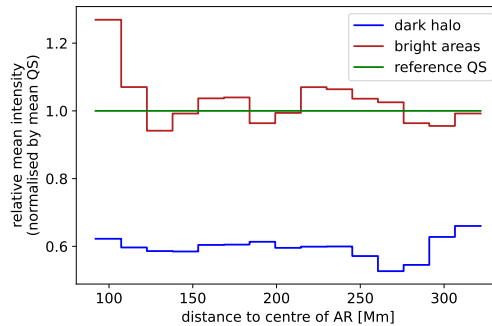


Figure 3.5: The relative mean HRI_{EUV}-intensity as a function of distance to the AR. The mean intensity has been normalised by the mean value derived for the reference QS. The relative mean intensity inside the dark halo (blue) and for the brighter areas in-between the dark halo (dark-red) are shown. The green line denotes the value for the reference QS.

3.4.1 Dark halo and CH overlap

The AR is surrounded by four dark halo patches, two larger ones and two smaller in size. We label the different dark halo patches DH1, DH2, DH3, and DH4 (see Fig. 3.1 for the labels). One of these larger dark halo patches, DH3, is a complex structure since it partially overlaps with a CH. The boundaries of the CH were identified via an intensity threshold of 40% of the median disc-intensity in the SDO/AIA 193 Å channel. This CH is adjacent to the AR and a smaller separate part of the CH overlaps with a dark halo patch. The contours of both the CH and the dark halo are displayed in Fig. 3.2. Subsequently, to confirm whether the structure is indeed a CH, we checked for the presence of open magnetic fields. To achieve this, we conducted magnetic field extrapolations using pfsspy (Stansby et al. 2020) on the Daily Update Synoptic Frames map of 2021 November 6 taken with the Helioseismic and Magnetic Imager (HMI; Schou et al. 2012) onboard SDO, and placed seeds in the areas covered by the dark halo patch DH3 and the larger CH. We then traced the field lines from these seeds at a height of 2 Mm above the photosphere and set the source surface to 2.5 solar radii. This way we could determine that any open field originates from within the area of the CH and also from the dark-halo–CH complex DH3. Fig. 3.4 displays the open field lines in green on the SDO/AIA 193 Å image.

3.4.2 Coronal emission at different temperatures

Inside the individual dark halo patches the emission in the HRI_{EUV} -channel is strongly reduced. In particular, the dark halo patches emit only between 57% and 64% of the mean emission coming from the reference QS (see Table 3.1 for absolute values).

3.4.2.1 Mean intensity's dependence on distance to AR centre

Inside each individual ring around the magnetic centre of the AR we derived the relative mean HRI_{EUV} -intensity (i.e. the mean intensity inside a ring divided by the mean intensity in the reference QS). In Fig. 3.3 we illustrate this for the dark halo and for the bright areas in-between. The area inside each ring is coloured according to the derived relative mean value for the area the ring covers. The

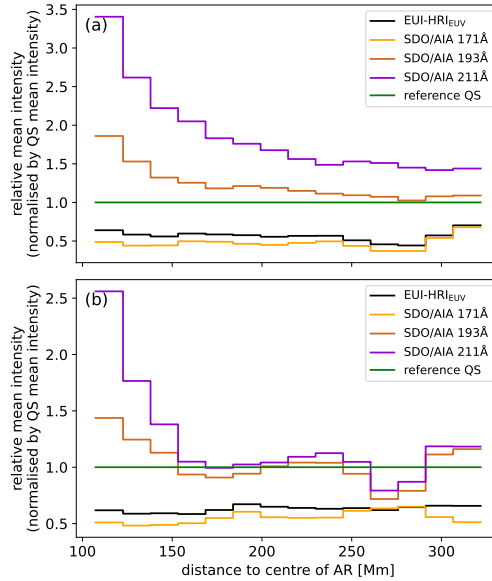


Figure 3.6: The relative mean intensities inside individual dark halo patches as a function of distance to the AR shown for HR1_{EUV} and the SDO/AIA 171 Å, 193 Å, and 211 Å channels. The mean intensity has been normalised by the mean value of the reference QS. This mean value of the QS is indicated by the green line. Panel (a) shows the emission from DH1, and panel (b) from the dark-halo–CH complex, DH3.

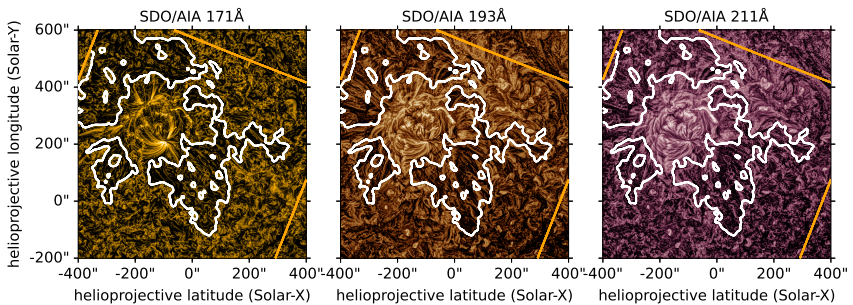


Figure 3.7: Enhanced images of the three SDO/AIA passbands 171 Å (left), 193 Å (middle), and 211 Å (right). The white contours outline the dark halo surrounding the AR and the orange square indicates the HR1_{EUV} 's FOV.

dark halo and bright areas exhibit very different behaviours. On the one hand, the intensity inside the dark halo stays clearly below QS level and does not vary much. It merely increases slightly towards the inner and outer boundaries. The intensity in the brighter areas, on the other hand, is 1.3 times that of the QS at its inner part. With increasing distance to the AR the intensity then drops towards a QS-intensity level. Additionally, the rings on the bottom right, covering a bipolar region, show higher intensities again.

Radial cuts through the the two areas displayed in Fig. 3.3 are shown in Fig. 3.5. The range over the dark halos is plotted from 92 – 330 Mm distance. For each value we determined the uncertainty of the mean σ_M as the standard deviation σ divided by the square root of the number of data points N :

$$\sigma_M = \frac{\sigma}{\sqrt{N}}. \quad (3.1)$$

The relative mean intensities for the dark halos are clearly much lower and stay below 0.7 at all times. As described above, the relative mean intensities in the brighter region initially drop from a higher than QS values to approximately the QS value and remain relatively constant at greater distances to the AR. At all distances there is a difference of at least 0.3 times the QS intensity between the dark halo and the brighter areas in-between.

3.4.2.2 Coronal emission at different temperatures in individual dark halo patches

We further wanted to see whether individual dark halo patches behave differently, in particular if DH3, the dark-halo–CH complex, shows any significant deviation. Additionally, it is essential to understand how the relative intensity behaves at different temperatures. For this we looked at co-temporal SDO/AIA observations. We chose three different SDO/AIA-passbands: 171 Å, 193 Å, and 211 Å. The HRI_{EUV} and SDO/AIA 171 Å channels are very similar yet not identical. While HRI_{EUV} has a passband at 174 Å and samples the solar corona at 1 MK with contributions from both the Fe IX and Fe X lines (Rochus et al. 2020), the 171 Å SDO/AIA channel has most of its contributions from the Fe IX line and probes the corona just below 1 MK (Lemen et al. 2011; Peter et al. 2012). The SDO/AIA 193 Å and 211 Å channels

see the corona at the higher temperatures of 1.6 MK, and 2.0 MK, respectively.

Iso-contours of the individual dark halo patches overlaid to the SDO/AIA-image are shown in Fig. 3.2 onto each SDO/AIA-image. Similarly to our approach with the HRI_{EUV} data, we calculated the mean intensity within each ring. This allows us to present the relative intensity as a function of distance for the different temperature channels, as shown in Fig. 3.6. To have a direct comparison with the HRI_{EUV} -channel and the reference QS, they are both included in the figure.

We conducted an analysis of the emission coming from the dark halo patch DH1 (see Fig. 3.6a). The cooler 171 Å SDO/AIA channel shows a rather uniformly reduced emission inside the dark halo patch, very similar to the HRI_{EUV} -channel. At hotter temperatures the emission from the dark halo patch DH1 has a very different behaviour: For The 193 Å channel the relative intensity at the inner boundary is nearly twice that of the QS. In the 211 Å channel the dark halo patch is even brighter and the relative intensity is more than three times as intense as in the QS. In both channels the relative mean intensity then decreases with increasing distance to the AR centre. Both channels exhibit emission above the QS level at all distances. At the outer boundary of the dark halo patch the relative intensities in the 193 Å passband are at about the level as the QS, while the 211 Å channels still shows more emission from the outer boundaries of the dark halo patch than from the mean QS.

The second dark halo patch for which we analysed the emission at different temperatures is the dark-halo-CH complex DH3 (Fig. 3.6b). We aimed to determine whether this structure behaves differently due to its CH contribution. At coronal temperatures around 1 MK DH3 shows a very similar behaviour to DH1. In the channels imaging hotter plasma (193 Å and 211 Å), the general trend also resembles that of DH1, showing mostly emission stronger than the QS-level and a decrease towards larger distances from the AR. However, two notable divergences are observed: at distances of 175 Mm and 280 Mm from the AR centre the intensities drop to or below the QS level before increasing again. These distances coincide with the areas where the embedded CH is located. While the CH's presence is distinctly visible in specific locations, the overall behaviour of DH3 is very similar to that of DH1.

3.4.2.3 Bright loops over dark halos

To better highlight coronal structures in and around the dark halo patches, we applied the method described by Morgan & Druckmüller (2014) which uses a multi-scale Gaussian normalisation to enhance the image contrast. It is implemented in the python packages `sunkit_image.enhance` and we used this package to create contrast enhanced images of the three different SDO/AIA channels. In the enhanced image of the SDO/AIA 171 Å channel bright loops originating from the periphery of the AR terminate approximately at the inner boundaries of the dark halo. There are no bright loops visible which cross over the dark halo patches or reach deep inside. At this temperature around 0.8 MK the corona is dominated by small-scale loops. Fewer of these small-scale loops appear within the dark halo than outside. The enhanced images of the passbands probing hotter plasma, on the other hand, show bright loops over the dark halo patches. Similar observations were also made by Singh et al. (2021). A discussion of their and our interpretation of this result can be found in Sect. 3.5.2. In detail we note that elongated brighter loops extend radially from the AR. They begin at the periphery of the AR and either cross the dark halo or terminate within it — some ending inside the halo itself or within the brighter islands it encloses. Other bright loops extend from within the dark halo, connecting either to the halo itself or to the bright islands it encloses, while some originate in these regions and stretch outward beyond the halo's boundaries. The bright loops are rooted in strong polarity patches located inside the dark halo, the bright islands, and outside the dark halo boundaries. In fact, the most of the stronger polarity patches within the dark halo and the bright islands seem to be footpoints of such bright and hot loops.

3.4.3 Photospheric magnetic field

Next, we study photospheric magnetic field of the dark halo patches and compare it to the magnetic field of the bright areas between them, and to the QS magnetic field.

Dark halo patch	$\langle B_{\text{LOS}} \rangle$ [G]	Imbalance in magn. flux		Emission (HRI _{EUV})	
		abs. ΔF [G]	rel. δF [%]	abs. [DN/s]	rel. to QS [%]
DH1	15.7	-1.6	10	339	57
DH2	14.1	+3.0	21	381	64
DH3	14.7	+2.2	15	373	62
DH4	14.2	+5.2	37	355	59
Entire dark halo ^a	15.1	+0.6	4	357	60
QS	15.0	+0.8	6	599	100

^a Averaged over all area covered by the dark halo patches.

Table 3.1: Magnetic field and coronal emission in individual dark halo patches.

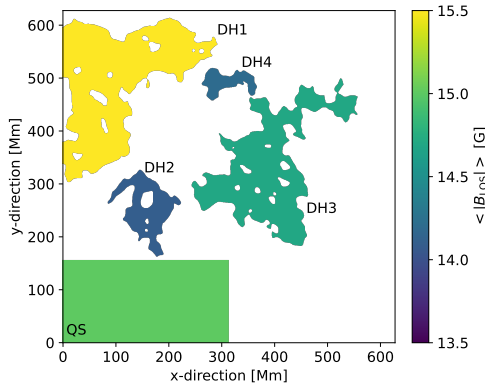


Figure 3.8: The mean $|B_{\text{LOS}}|$ value above the noise level of $1\sigma = 7.4$ G of individual dark halo patches and for the reference QS.

3.4.3.1 Average magnetic field strength

For each of the dark halo patches we derived the unsigned magnetic field, $\langle |B_{\text{LOS}}| \rangle$, individually and compared them to the reference QS. The $\langle |B_{\text{LOS}}| \rangle$ in each dark halo patch was obtained from the LOS magnetogram by calculating the mean of the absolute values above the noise level of $1\sigma = 7.4$ G (see Sinjan et al. (2022) for a sensitivity analysis of SO/PHI data).

The values for the individual dark halo patches are shown in Fig. 3.8 and listed in Table 3.1. The $\langle |B_{\text{LOS}}| \rangle$ values inside dark halo patches DH2, DH3, and DH4 are slightly below the 15.0 G we derived for the reference QS. DH1 lies above this

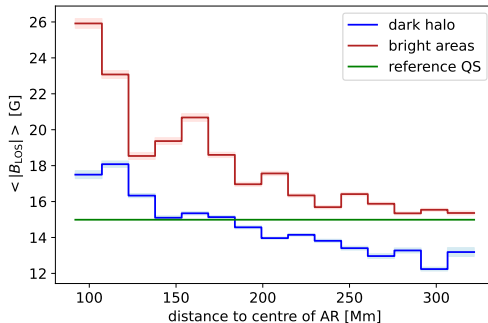


Figure 3.9: Unsigned LOS magnetic field, $\langle |B_{\text{LOS}}| \rangle$, in dependence of distance to the AR centre above the noise level of $1\sigma = 7.4$ G. The $\langle |B_{\text{LOS}}| \rangle$ inside the dark halo (i.e., we averaged over all dark halo patches at a certain distance to the AR and do not treat them separately) is shown in blue, the red curve shows the $\langle |B_{\text{LOS}}| \rangle$ for the bright areas in-between the dark halo patches. Lighter colours denote the uncertainty of the mean σ_M . The mean value of the QS is shown in green.

reference QS value; however, the outer parts of this particular dark halo patch are not covered by the SO/PHI-HRT magnetogram. As we will show in Sect. 3.4.3.2 the magnetic elements are not distributed evenly within the dark halo patch. Only considering the dark halo partially could lead to a higher $\langle |B_{\text{LOS}}| \rangle$ value. The average of all dark halo patches is 15.1 G. Therefore, the $\langle |B_{\text{LOS}}| \rangle$ inside the dark halo patches is on average very close to that of the QS.

3.4.3.2 Magnetic field strength's dependence on distance to AR centre

The coronal emission at higher temperatures strongly depends on the distance to the centre of the AR. Therefore, we also study the dependence of the underlying magnetic field on distance. For this, we calculated $\langle |B_{\text{LOS}}| \rangle$ in rings around the AR in the same way as we did for the coronal intensities described in Sect. 3.4.2.1. Once again we determine the properties both inside the dark halo and in the brighter areas surrounding them. For both regimes separately, we calculated $\langle |B_{\text{LOS}}| \rangle$ in each ring by including only those pixels who have field strengths above the noise level of $1\sigma = 7.4$ G.

However, $\langle |B_{\text{LOS}}| \rangle$ inside the dark halo is significantly lower than in the brighter in-between areas (see Fig. 3.9). For both the dark halo and for the

brighter areas in-between we see a strong decrease away from the AR of the measured $\langle |B_{\text{LOS}}| \rangle$ closest to the AR. However, $\langle |B_{\text{LOS}}| \rangle$ inside the dark halo is significantly lower than in the brighter in-between areas (see Fig. 3.9). Specifically, inside the dark halo $\langle |B_{\text{LOS}}| \rangle$ drops below the QS level at a distance to the AR centre of 150 - 200 Mm and decreases further. In the bright in-between areas $\langle |B_{\text{LOS}}| \rangle$ remains above the QS everywhere. The $\langle |B_{\text{LOS}}| \rangle$ in these areas gradually trends towards the QS level with increasing distance to the AR centre. We further examined $\langle |B_{\text{LOS}}| \rangle$ within the individual dark halo patches DH1, DH2, and DH3 (shown in Fig. 3.10). DH4 was excluded from the analysis due to its small size. The analysis also focused on potential differences between dark halo patches DH1 and DH2 on the one hand, and DH3 on the other, which includes the CH contribution. We can report that none were found: All three dark halo patches exhibit trends consistent with that observed for the averaged dark halo in Fig. 3.9. In conclusion, the common behaviour among all individual dark halo patches and the averaged dark halo is that $\langle |B_{\text{LOS}}| \rangle$ consistently drops below the QS level.

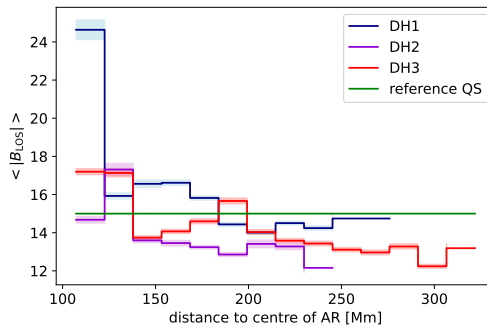


Figure 3.10: The $\langle |B_{\text{LOS}}| \rangle$ as a function of distance to the AR centre for individual dark halo patches. The lighter colours denote the uncertainty of the mean σ_M . The mean value of the QS is shown in green.

3.4.3.3 Flux imbalance in dark halos

Following Nölke et al. (2023) for coronal voids, we examined the imbalance in the magnetic flux within the dark halo patches and derived the relative and absolute flux imbalances (according to Eqs. 2.2 and 2.3, respectively) for the entire

dark halo as well as for the four large dark halo patches individually, comparing these with our reference QS area. The entire area covered by the dark halo is relatively flux balanced. The relative imbalance derived is 4% corresponding to 0.6 G. The reference QS area shows a very similar value of 6% corresponding to 0.8 G of absolute flux imbalance. The individual dark halo patches exhibit different strengths of imbalance and even different signs, which can be found in Table 3.1. DH1 partially overlaps with a negative polarity plage region at its innermost part, while the other dark halo patches have flux imbalances with a positive sign. Overall, the measured flux imbalances are small. The variation of these values might be due to limited statistics, as the areas covered by the individual dark halo patches are relatively small.

3.5 Discussion

3.5.1 Comparison of dark halos to CHs and coronal voids

Besides coronal dark halos, CHs and coronal voids are structures that also exhibit reduced emission in the EUV. CHs show lower emission and hence an increasing difference to their surroundings towards higher coronal temperatures. In contrast, at low coronal temperatures the dark halo studied here generally displays a uniformly reduced emission below the QS-level, while at higher temperatures its emission is significantly stronger than in the QS and shows a negative intensity gradient with distance from the centre of the AR. Still, the emission from the dark halo patch DH1 in the 193 Å and 211 Å SDO/AIA channels consistently remains above or at the QS-level. At these higher temperatures the equatorial CH becomes distinctly visible in the coronal emission from the dark halo patch DH3, where two clear dips in emission correlate with the location of the CH. This creates a noticeable contrast between dark halos and CHs at higher temperatures, making higher-temperature channels useful for distinguishing between the two. The dark halo and coronal voids both show a strong reduction in emission at 1 MK compared to the QS. Most of the individual dark halo patches have a $\langle |B_{LOS}| \rangle$ that is slightly lower than that of the QS (see Sect. 3.4.3.1). In contrast, the $\langle |B_{LOS}| \rangle$

inside coronal voids is with only 76% significantly below the QS level (Nölke et al. 2023). However, we see a significant difference between $\langle |B_{\text{LOS}}| \rangle$ inside the dark halo and in the bright areas surrounding the dark halo patches (see Sect. 3.4.3.2).

In addition to the 2021 November 5 Solar Orbiter observations, we further analysed SDO/HMI observations of 2018 April 22 studied by Lezzi et al. (2023). By applying a noise level threshold of 8 G, we derive $\langle |B_{\text{LOS}}| \rangle = 16.1$ G for the QS and a $\langle |B_{\text{LOS}}| \rangle$ value of 15.6 G inside the dark halo. This value for the dark halo is slightly lower than the 17.0 G reported by Lezzi et al. (2023) (see Appendix A.3). The QS $\langle |B_{\text{LOS}}| \rangle$ value of 16.1 G is 0.5 G above the value we obtained for the dark halos, which is in agreement with the values we derived from the 2021 November 5 Solar Orbiter data.

Unlike CHs and coronal voids, dark halos typically show a systematic trend of the unsigned magnetic field dropping with radial distance from the AR, i.e. from their boundaries closest to the AR centre to their outer boundaries (see Sect. 3.4.3.2 and Appendix A.3). Close to the boundary to the AR the magnetic field is significantly stronger than in the QS. Then it drops to field strengths below the QS, and hence to values that compare well to coronal voids. In CHs and coronal voids the magnetic elements are more uniformly distributed than in the dark halos.

The dark halo patches show flux imbalances ranging from 10% to 37% (see Table 3.1 and Sect. 3.4.3.3). Equatorial CHs on the other hand typically show much stronger flux imbalances of at least 50% (Wiegmann & Solanki 2004; Hofmeister et al. 2017). DH3, which overlaps with the equatorial CH, shows no significant deviation from the other dark halo patches.

3.5.2 Nature of dark halos

We confirm the finding of Wang et al. (2011) that in the dark halos on average the $\langle |B_{\text{LOS}}| \rangle$ is slightly weaker than in the QS. However, our detailed analysis shows a more complex picture. The $\langle |B_{\text{LOS}}| \rangle$ drops with distance from the AR, and only in the outer parts of the dark halos the $\langle |B_{\text{LOS}}| \rangle$ is weaker than the AR. Still, at the same distance from the AR the $\langle |B_{\text{LOS}}| \rangle$ in the dark halo is weaker than in the bright areas between them (see Sect. 3.4.3.2)

The consistently lower value of $\langle |B_{\text{LOS}}| \rangle$ in the dark halo compared to the brighter regions between them could explain why the dark halos show reduced emission by direct comparison. A weaker magnetic field is indicative of less heating of coronal plasma and hence a lower intensity from plasma around 1 MK. In the outer parts of the dark halo where the magnetic field is weaker than in the QS reduced coronal heating, similar to coronal voids in the QS (Nölke et al. 2023), could be a mechanism contributing to the reduced emission. However, while the magnetic field drops with distance from the AR, the emission seen in the SDO/AIA 171 Å and EUV channels is almost constant with distance. Moreover, because the $\langle |B_{\text{LOS}}| \rangle$ in the inner part of the dark halo is stronger than in the QS, one would naively expect the the SDO/AIA 171 Å and EUV emission to be stronger in the inner part of the dark halo than in the QS, in contrast to our observations. One might consider at least two possible scenarios that might explain this.

Firstly, the heating of the corona depends not only on the magnetic field, but also on horizontal flows, that together set the vertical Poynting flux and hence the energy flux into the corona. Smaller horizontal flows near the AR could compensate for an increasing magnetic flux and keep the heating rate stable throughout the dark halo. This would in turn lead to the uniformly reduced intensity seen in the SDO/AIA 171 Å and EUV channels. Future research could explore this possibility further by investigating the horizontal flows in the vicinity of ARs.

Secondly, the emission from cooler plasma (≤ 1 MK), as seen in the structures in the enhanced image of the SDO/AIA 171 Å channel (see Fig. 3.7), is organised in short loops. Within the dark halo less of these loops are visible. This is in direct contrast to plasma at hotter temperatures (≥ 1.6 MK) probed by the SDO/AIA 193 Å, and 211 Å channels, where the emission is organised in longer loops that often spread radially away from the AR. Interestingly, the emission observed in these hotter passbands exhibits a similar radial dependence to that of the magnetic field. These longer loops predominantly connect to the stronger magnetic patches within the dark halo or to the brighter islands within the dark halo structure. It is therefore possible that different magnetic structures are visible at different coronal temperatures. Hot long-ranging loops have previously

also been observed by Singh et al. (2021). Their model explains the difference between the hotter and cooler plasma seen in the different passbands with strong magnetic pressure exerted onto the small scale loops that are then confined to stable heights below 5 Mm.

3.6 Conclusions

We studied the coronal dark halo around the AR NOAA 12893. Specifically, we analysed the coronal emission at different temperatures and the photospheric magnetic field as a function of distance to the AR centre.

We report a radial profile in emission for the dark halo that varies with distance for higher coronal temperatures (≥ 1.6 MK) and shows reduced emission throughout the dark halo at temperatures ≤ 1 MK (Sect. 3.4.2). Similarly, we detected variations in the unsigned magnetic field, $\langle |B_{\text{LOS}}| \rangle$, with distance (Sect. 3.4.3). These radial dependencies of the emission and magnetic field imply that studies should not solely rely on mean values, as done before.

The data set further allowed us to analyse an equatorial CH adjacent to the AR (see Sects. 3.4.1, 3.4.2.2, and 3.5.1). Dark halos and CHs can clearly be distinguished via their emission at different coronal temperatures because CHs show a strong contrast above 1 MK, whereas dark halos are only visible below these temperatures. This was also reported by Lezzi et al. (2023).

In Sects. 3.1 and 3.5.2 we discuss existing models explaining the dark halos and propose an additional explanation: The source regions of hotter emission (≥ 1.6 MK; see Sect. 3.4.2.2) with visible loops over and reaching inside the dark halo (Sect. 3.4.2.3) are likely less dominated by the local magnetic field of the dark halo, but rather by the large-scale magnetic field of the AR. The dark halo shows a clear reduction of $\langle |B_{\text{LOS}}| \rangle$ compared to its brighter surroundings (Sect. 3.4.3.2). At its outer boundaries it falls below the QS level. We suggest that reduced coronal heating might locally contribute to the dark halos dark appearance. While this could explain the reduced emission at the outer boundaries, another mechanism must be responsible for the reduced emission closer to the AR centre where the $\langle |B_{\text{LOS}}| \rangle$ is stronger than in the QS.

3. Magnetic structure of coronal dark halos

Future work could include an analysis of horizontal flows around ARs to test whether reduced flows within dark halo near the AR lead to a smaller Poynting flux, resulting in lower heating and thus reduced coronal emission. Obtaining new observations that include coronal spectroscopic measurements, for example from the SPICE instrument (SPICE Consortium et al. 2020), would be immensely beneficial. These data would allow us to identify potential outflows by examining Doppler shifts within a dark halo. This would help us to either identify clear boundaries of dark halos, CHs, and outflow areas or reveal where these phenomena converge, allowing for further characterisation of this region. Studying more dark halos would also enable us to gather statistical data on the correlation between the radial distance to an AR and the $\langle |B_{\text{LOS}}| \rangle$ or the coronal emission.

4. Conclusions and outlook

4.1 Conclusions

In this thesis two projects were presented that study the magnetic field and emission of extended areas in the solar corona with reduced emission. Each project explored a different region of the corona.

The first project (see Chapter 2) focused on the discovery and first description of dark regions in EUV-images of the QS, which we termed ‘coronal voids’. These features are clearly defined by an intensity contour set at 75% of the average QS emission in the 174 Å passband and their sizes range from one to several supergranular cells. We also observed reduced chromospheric Ly- α emission within these voids, supporting their identification as distinct low-emission structures.

We initially considered two possible explanations for the diminished EUV emission in these voids. The first proposed that weaker photospheric magnetic fields in these regions result in reduced magnetic heating, leading to lower temperatures and densities, and thus fainter coronal emission. The second hypothesis suggested that the voids might function as small-scale CHs, where open magnetic field lines allow plasma to escape, diminishing heating and emission.

Our analysis of the photospheric magnetic field reveals that the mean LOS field strength within the voids is 1.3 to 1.6 times weaker than in the surrounding QS. Crucially, the voids also lack the stronger magnetic flux concentrations typically found in the QS network. These findings indicate that the upper atmosphere in these regions receives less magnetic energy, leading to lower heating rates and reduced emission. The RTV scaling relations (Rosner et al. 1978) further support this, confirming that weaker magnetic flux should yield lower temperatures, densities, and coronal brightness.

Although we detect some magnetic flux imbalance in the voids the degree

of imbalance is consistent with that of similarly sized QS regions, and can be attributed to a small sample bias. Additionally, potential field extrapolations show no evidence of open field lines within the voids. We therefore conclude that coronal voids are not miniature CHs but rather distinct features arising from locally suppressed magnetic flux and the consequent reduction in coronal heating.

In a second project (see Chapter 3) we investigated coronal dark halos surrounding ARs, specifically the one surrounding NOAA 12893. We focused on the coronal emission across various temperatures by combining HRI_{EUV} and SDO/AIA observations and on the behaviour of the photospheric magnetic field as a function of distance from the AR centre.

An equatorial CH adjacent to the AR was also within the FOV and partially overlapped with the dark halo. We compared the plasma emission at various temperatures in both the CH and the dark halo. While CHs exhibit strong contrast at temperatures above 1 MK, dark halos are primarily distinguishable at lower temperatures. This distinction is consistent with the findings of Lezzi et al. (2023).

Our analysis reveals a radial dependence of the hotter coronal emission (≥ 1.6 MK) within the dark halo, whereas at lower plasma temperatures (≤ 1 MK), the dark halo consistently exhibits reduced emission. A comparable radial trend was observed in the unsigned magnetic field, $\langle |B_{\text{LOS}}| \rangle$. These findings indicate that relying solely on average values, as in previous studies, may overlook significant spatial variations.

The reduced emission in dark halos compared to surrounding brighter regions may be linked to the consistently lower $\langle |B_{\text{LOS}}| \rangle$, suggesting weaker magnetic fields and thus reduced coronal heating around 1 MK. In the outer halo, where the magnetic field is even weaker than in the QS, this mechanism resembles that proposed for coronal voids (Nölke et al. 2023). However, the observed emission in the SDO/AIA 171 Å and EUV channels remains nearly constant with distance, despite a declining magnetic field. Moreover, the inner dark halo, where $\langle |B_{\text{LOS}}| \rangle$ exceeds QS levels, still shows lower emission than the QS, contradicting expectations based solely on magnetic flux density.

Two possible explanations are considered that need to be tested in future

work. Firstly, reduced horizontal flows near the AR may limit the vertical Poynting flux leading to uniformly low coronal heating across the halo. Secondly, emission at lower temperatures (≤ 1 MK) arises from short loops, which are less prevalent within the dark halo. In contrast, hotter plasma (≥ 1.6 MK) loops are more elongated, extending from the AR into the halo, and align well with the magnetic field distribution. These structures likely connect to stronger magnetic patches or bright islands within the halo, implying a temperature-dependent magnetic topology.

4.2 Outlook

4.2.1 Future research directions

This section outlines directions for future research that build upon and extend the work presented in this thesis. Several avenues are proposed that may contribute to a deeper understanding of the physical conditions within and surrounding coronal voids and dark halos. In Sect. 4.2.2 we present initial findings from some follow-up studies that are already underway.

One possible follow-up study could be a spectroscopic analysis, for instance using data from the SPICE instrument. Given SPICE's low spectral resolution, it's unclear whether this is feasible. Therefore, a feasibility study will have to be conducted first to assess its viability. A spectroscopic analysis would allow to search for outflows in both coronal voids and dark halos by examining Doppler shifts within these structures.

A statistical analysis of coronal voids could help to better understand their physical properties. Important parameters to investigate include size, magnetic field strength, and emission, as well as possible correlations between them. For this, a large set of QS observations is needed. Since Solar Orbiter was launched only recently, the amount of suitable QS data is still limited. As an alternative, SDO/AIA observations could be used. However, a careful comparison between the HRI_{EUV} and SDO/AIA 171 Å channels would be needed to define an intensity threshold for identifying coronal voids in SDO/AIA data that matches

the definition used for HRI_{EUV} .

A possible avenue of investigation concerns the Poynting flux in coronal dark halos. As noted in Sect. 3.5.2, a reduced Poynting flux at the inner boundary of these halos may account for their uniformly reduced emission, despite the presence of stronger magnetic fields compared to the outer regions. This could be examined by analysing horizontal flows near the AR by through motion tracking.

An analysis of the morphology of coronal voids would provide valuable insights into the distribution of both emission and magnetic elements within these structures (see also Sect. 4.2.2.1). This could involve investigating whether the emission is darkest in the centre of the voids, or whether there are other patterns in how emission and magnetic field strength vary across the void. Such an analysis could further illuminate the underlying physical processes governing these structures.

Studying the evolution of coronal voids could provide a deeper understanding of their formation processes and help estimate their lifetimes. This would involve examining changes in emission, magnetic field strength, and size over time, and determining the relevant timescales. Initial work in this direction has already been conducted for a timescale of three hours, and some of these findings are presented in Sect. 4.2.2.2.

Coronal voids could be examined at multiple temperatures using co-temporal HRI_{EUV} and SDO/AIA observations. However, this was not feasible for the 2021 February 23 dataset due to Solar Orbiter’s position behind the Sun. More recent observations, however, include co-observations with SDO/AIA (see also Sect. 4.2.2.3).

4.2.2 Initial results of follow-up projects

In this section, we present preliminary results from selected follow-up projects introduced in Sect.4.2.1, using a time series acquired by Solar Orbiter. The dataset was recorded on 2022 March 8, when Solar Orbiter was positioned at 0.49 AU, nearly aligned with the Sun–Earth line, at an angle of 1.2° . SO/PHI-HRT observed continuously for two hours with a cadence of 1 minute, from 00:00 to 02:00. EUV started at the same time and continued observing until 03:00.

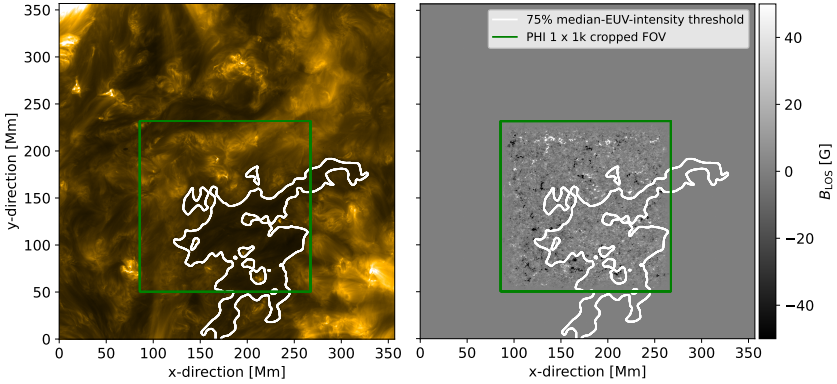


Figure 4.1: Overview of the 2022 March 8 dataset. The HRI_{EUV} (left) and $\text{SO}/\text{PHI-HRT}$ (right) observations at the beginning of the time series at 00:00. The contours of the coronal void are outlined in white and the green square indicates the cropped FOV of the $\text{SO}/\text{PHI-HRT}$ observation.

The cadence of the HRI_{EUV} instrument varied between 2 and 20 s. To match the cadence of $\text{SO}/\text{PHI-HRT}$, we combined HRI_{EUV} images to achieve a uniform 1-minute cadence. All HRI_{EUV} and $\text{SO}/\text{PHI-HRT}$ images were co-aligned to the first HRI_{EUV} frame at 00:00 and spatially rescaled to the HRI_{EUV} resolution of 174 km/pixel. Due to limited telemetry the $\text{SO}/\text{PHI-HRT}$ observations have been cropped to $1\text{k}\times 1\text{k}$, only showing the centre of the FOV. At 00:30, the EUI filter setting changed from ‘Aluminium_174_1’ to ‘open’ together with an increase in exposure time from 1.65 s to 2.8 s. Images taken with this second setting show pixel saturation in several regions.

The EUI observations show a QS region surrounded by four ARs. Both HRI_{EUV} and $\text{SO}/\text{PHI-HRT}$ see a coronal void; however $\text{SO}/\text{PHI-HRT}$ does not cover the full extend of it. Despite the ARs visible at the edge of the FOV, this void is at a considerable distance to them and shows the void-typical absence of any network structures. Fig. 4.1 provides an overview of the observations at the start of the time series, indicating the location of the coronal void and the cropped $\text{SO}/\text{PHI-HRT}$ FOV. Due to the presence of ARs, the intensity distribution deviates

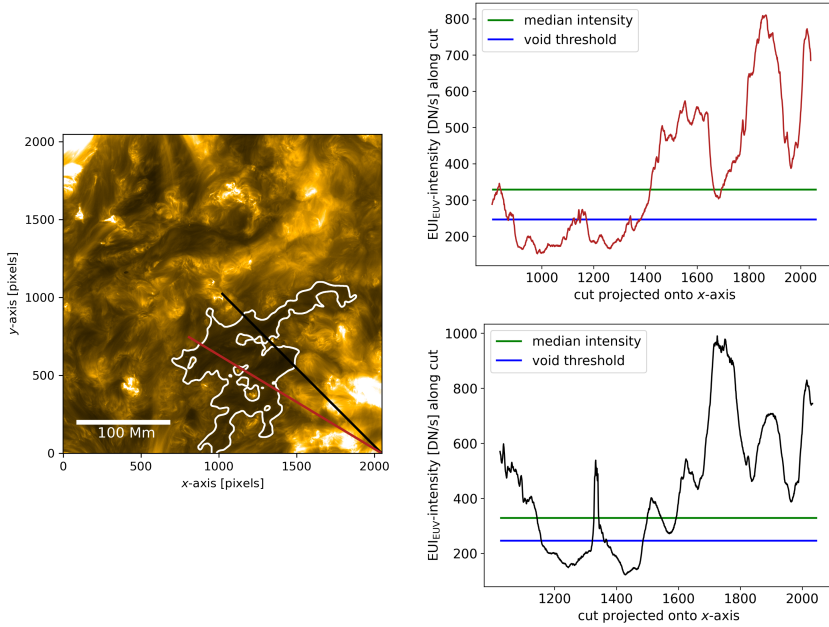


Figure 4.2: Left panel: The HRI_{EUV} observation at 00:00 is overlaid with the coronal void's boundary (white contour). Two cuts through the void are marked by the black and red lines. Right panels: The plots show the HRI_{EUV} intensities along the cuts (red and black lines), projected onto the x -axis.

from a log-normal shape. For this reason, we adopt the median rather than the mean as a reference value for the coronal void specific intensity-threshold throughout this analysis.

4.2.2.1 Morphology of coronal void

We examined two cuts through the coronal void, similar to the approach taken in Sect. 2.3.2 for the $\text{HRI}_{\text{Ly}\alpha}$ and HRI_{EUV} -images. This method provides a clearer picture of the internal structure of the void, rather than considering it as a single, uniform feature. For our analysis we used a single snapshot HRI_{EUV} -image taken at 00:00.

We computed the EUV-intensity along each cut (with a width of 20 pixels)

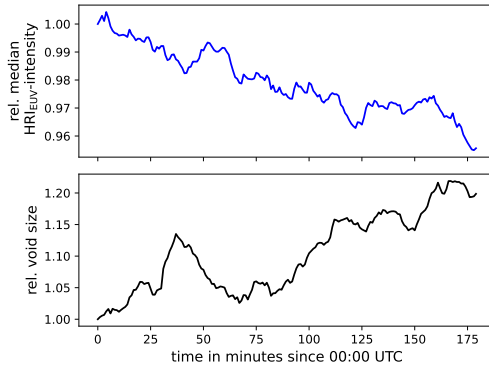


Figure 4.3: The evolution of a coronal void for EUV-intensity and size. The evolution of the coronal void is traced both in EUV-intensity (top panel) and in size (bottom panel) from 2022 March 8 00:00 to 03:00. We normalised the plotted values to the initial values at 00:00 to highlight the relative changes.

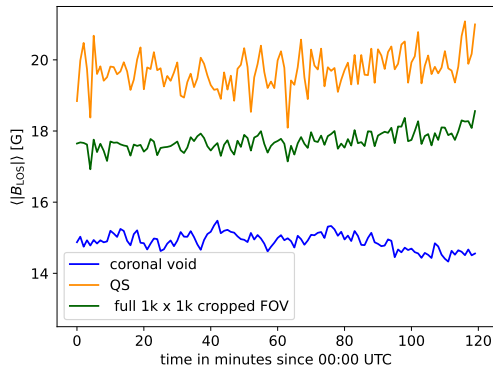


Figure 4.4: The evolution of the unsigned magnetic field of a coronal void. $\langle |B_{LOS}| \rangle$ is shown for the coronal void (blue), the QS (orange), and for the entire $1k \times 1k$ FOV of the SO/PHI-HRT instrument (green) over two hours covering the period between 2022 March 8 00:00 and 02:00.

to investigate how the emission varies across different regions within the void. The positions of these cuts, overlaid on the HRI_{EUV} -image, are shown in Fig. 4.2, left panel. The corresponding intensity profiles, projected onto the x -axis, are displayed in the same figure in the panels on the right.

It is evident that, as the cut approaches the coronal void, the EUV-emission falls below the average or median level, eventually dropping beneath the threshold of 75% used to define the void itself. The intensity varies along the cuts, rising again where the slice intersects a brighter region within the void. The deepest point reached corresponds to $\sim 70\%$ of the HRI_{EUV} intensity.

While this analysis has so far focused on the HRI_{EUV} channel, it could be extended to include SDO/AIA data, allowing for a comparison of the void's structure across different temperature ranges.

4.2.2.2 Evolution of a coronal void

We looked at the the time evolution of the coronal void. We first focused on the coronal emission in the HRI_{EUV} channel and observed how the void's size and average intensity varied during the three hour observing time span.

As mentioned above the filter setting and exposure time changed after 30 minutes, resulting in saturated pixels. We compensated for that by increasing the coronal void threshold from 75 to 78% and by adjusting the intensity by a factor of 0.935. In this way we could correct for the offsets that occurred due to the different settings.

Over the three hours the coronal void grew in size by 20%, and over the same time span its average intensity decreases by 5%. We can conclude that the void persists for at least this amount of time. It would be extremely beneficial to follow the void over a longer period of time. This could be achieved by further tracing the void in the SDO/AIA 171 Å channel. However, this is not trivial as the HRI_{EUV} and 171 Å channels do not probe plasma at the exact same temperature (see Sect. 3.4.2.2). A detailed comparison of how to identify voids in both channels is needed beforehand. The observations of 2022 March 8 are suitable for this purpose.

We further examined the temporal evolution of the coronal void's magnetic

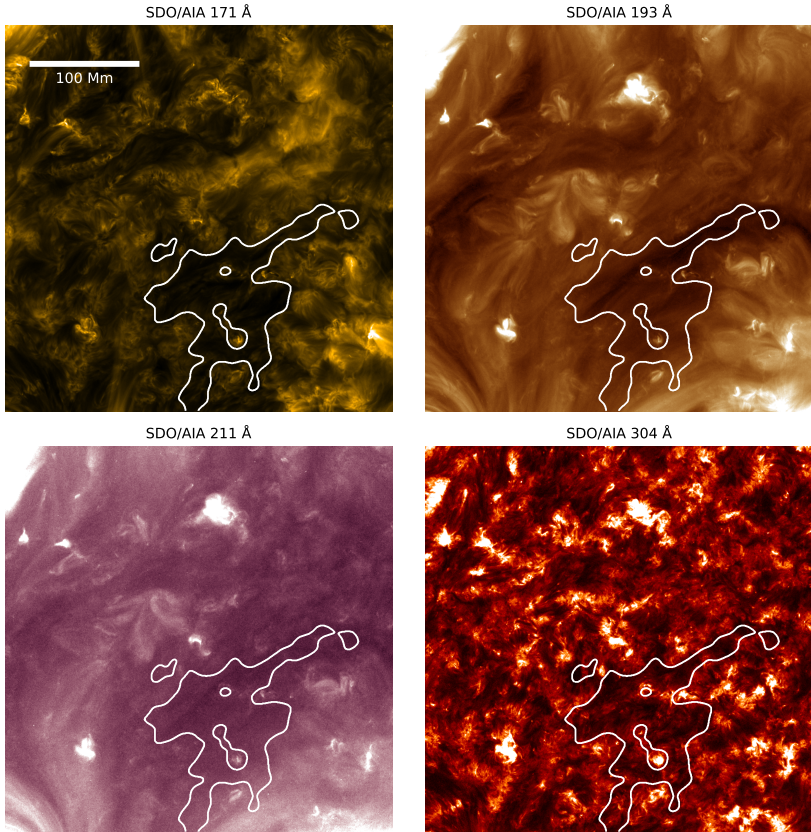


Figure 4.5: A coronal void at different plasma temperatures. The four panels show the HRI_{EUV} FOV for different SDO/AIA channels on 2022 March 8 at 00:00. The contours of the coronal void are overlaid in white.

field. We used a single contour that covers all the space ever occupied by the void during these two hours. Within the void, the surrounding QS, and for the full FOV we calculate the unsigned magnetic field, $\langle |B_{\text{LOS}}| \rangle$, as the average absolute values in pixels above the noise level of $1\sigma = 8.3$ G. This is shown in Fig. 4.4. The unsigned magnetic field does not show any significant changes in either of the areas. Within the void, it decreased marginally from 15.0 G to 14.5 G, remaining

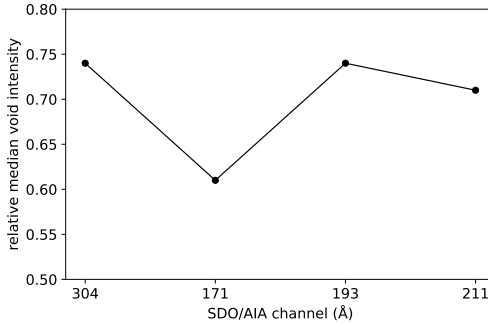


Figure 4.6: The relative emission in a coronal void at different temperatures. The normalised the median emission inside the coronal void by the median emission inside the entire HRI_{EUV} FOV. This is shown for four different SDO/AIA channels.

consistently lower than the QS value of ~ 20 G. The average of the entire FOV lies in between these values at ~ 17.5 G.

Extending this analysis to SDO/HMI data would allow for a full coverage of the void and a longer time series beyond the two-hour window provided by SO/PHI-HRT.

We also examined how the flux imbalance evolved over time within the void and the cropped FOV of SO/PHI. The observed FOV maintains a flux imbalance of about 25% throughout the two-hour period. A similar trend is evident in the coronal void. However, the FOV is too small to determine with certainty whether the imbalance arises from its limited size or is intrinsic to the magnetic field structure in that region. To draw more reliable conclusions, a larger area would need to be considered. In future work, this could also be addressed by extending our analysis to SDO/HMI data.

4.2.2.3 Coronal void at different plasma temperatures

Thanks to Solar Orbiter’s favourable position, nearly aligned with the Sun–Earth line, we were able to complement the EUV observations with SDO/AIA data from multiple channels, each sensitive to coronal plasma at different temperatures. The HRI_{EUV} FOV of the relevant SDO/AIA channels are shown in Fig. 4.5. Compared to the surrounding regions, emission within the void appears reduced across

all channels. We quantified this by calculating the relative median intensity within the void for each plasma temperature, normalising it by the median intensity across the full HRI_{EUV} FOV. The results, presented in Fig. 4.6, show that the 171 Å channel exhibits the strongest reduction, with a relative value of 0.61. The remaining channels still show significant reductions ranging from 0.71 to 0.74. Lezzi et al. (2023) carried out a similar analysis on a coronal dark halo. They found the strongest reduction in emission at temperatures up to 0.8 MK, while at higher temperatures no significant reduction was observed. Their method differs somewhat from ours, as they normalised the emission by the average QS intensity after applying a centre-to-limb correction to account for limb brightening. Therefore, the relative emission values are not directly comparable. Nonetheless, the similarities between our observations are clearly apparent. Future studies should build on this work by examining additional coronal voids as well as dark halos, to better understand where the structures are alike or differ, and to clarify whether the feature we analysed can indeed be classified as a coronal void.

Appendix

A.1 Threshold of coronal voids

To evaluate the robustness of our method for identifying coronal voids, we varied the intensity threshold applied to the intensity images. Fig. A.1 displays contours outlining the voids for a range of threshold values. At lower thresholds, many of the void regions are only partially captured or entirely missed. A threshold of at least 75% is recommended, as it consistently identifies the voids. For thresholds above 75%, numerous small and spatially scattered regions begin to emerge. Overall, by eye 75% offers a good balance between under- and over-identification of structures, though slightly higher or lower thresholds could also be reasonable choice.

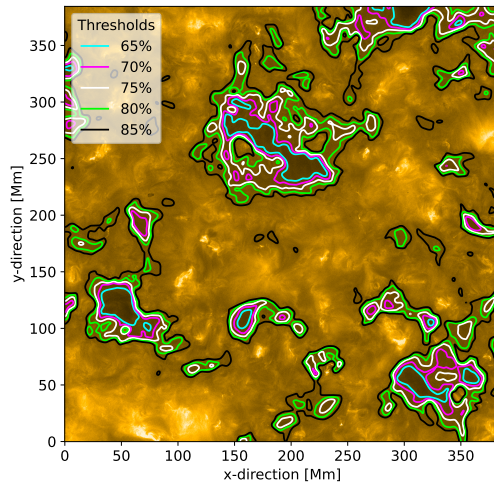


Figure A.1: Different intensity-thresholds identifying coronal voids. Five different intensity-thresholds are show that outline the coronal voids in the HRI_{EUV}-image.

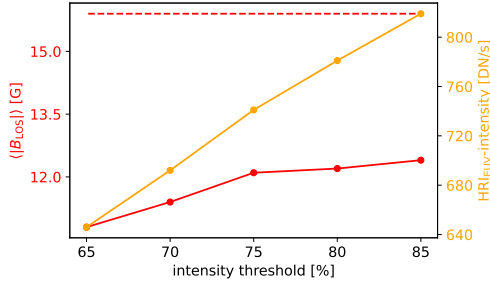


Figure A.2: Variation with intensity threshold in void no. 1. The average unsigned magnetic field, $\langle |B_{LOS}| \rangle$, is shown in red as a function of the applied intensity threshold. The dashed line marks the corresponding value for the QS. The mean HRI_{EUV} intensity within the void is plotted in orange as a function of the threshold.

We tested the robustness of both intensity and unsigned magnetic field, $\langle |B_{LOS}| \rangle$, with respect to the chosen intensity threshold. This is illustrated in Fig. A.2 for the largest void (no. 1) within the observational FOV. As expected, the mean intensity inside the void increases with increasing threshold. The correlation that we see is nearly linear. The average unsigned magnetic field, $\langle |B_{LOS}| \rangle$, also shows an increase, although it remains relatively moderate when compared to its contrast with the QS value. Across a threshold range of 20%, from 65% to 85%, $\langle |B_{LOS}| \rangle$ increases by only 1.6 G, whereas the difference between the void and the QS at a 75% threshold is 3.8 G. We can therefore assume a robustness of our results with respect to the intensity threshold.

A.2 Determining the centre of the AR

To calculate the properties of the dark halo as a function of distance from the AR centre, we first needed to determine the AR's central position. Several approaches were tested in this context. Specifically, we considered the geometric centre of pixels exceeding a magnetic field threshold, the centre of gravity, and the centroid of the brightest HRI_{EUV} emission. Some of these results are shown in Fig. A.3.

For the geometric centre, defined as the centroid of all pixels with magnetic field strength above a given threshold, we explored multiple threshold values. Fig. A.3 illustrates this for thresholds of 100 G. At 500 G, the resulting centre lies very close to the strong leading sunspot rather than at what we would by eye identify as the centre of the AR. This is why we also opted against using the centre

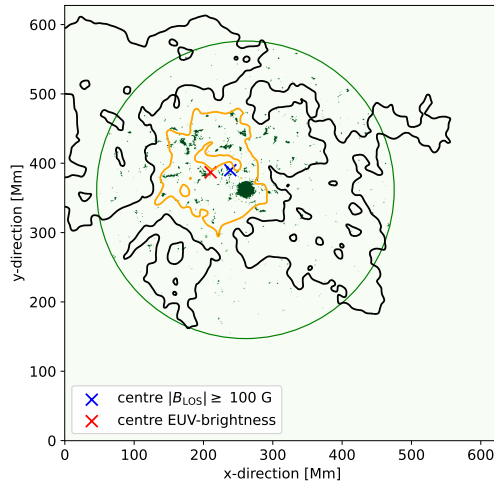


Figure A.3: The centre of the AR was determined using different methods. The black contours indicate the extent of the dark halo. Pixels with magnetic field strength exceeding 100 G and located within the green circle (with a radius 700 pixels) are highlighted in green. The blue 'X' marks the geometric centre of these pixels. The orange contours outline the EUV-brightest parts in the HRI_{EUV} observation. The orange contours outline the brightest areas in the HRI_{EUV} observations, with their geometric centre indicated by a red 'X'.

of gravity, which would disproportionately weight the sunspot's strong field. A threshold of 100 G, on the other hand, provides a more balanced representation by including both the intense sunspot fields and the more dispersed opposite polarity flux.

The final centre was computed by selecting all pixels with field strength above 100 G within a radius of 700 pixels around the leading sunspot. This position was then iteratively refined until convergence. To avoid convergence towards a local extremum, we additionally tested various initial positions.

The centroid based on the brightest HRI_{EUV} regions (twice the median value) yielded comparable results and may also serve as a viable centre definition. However, we chose the geometric centre of pixels with fields above 100 G in this study, as it offers a more robust measure; in particular when applied to other ARs, where the bright loops may be inclined above the surface and thus shift the apparent centre in HRI_{EUV} observations.

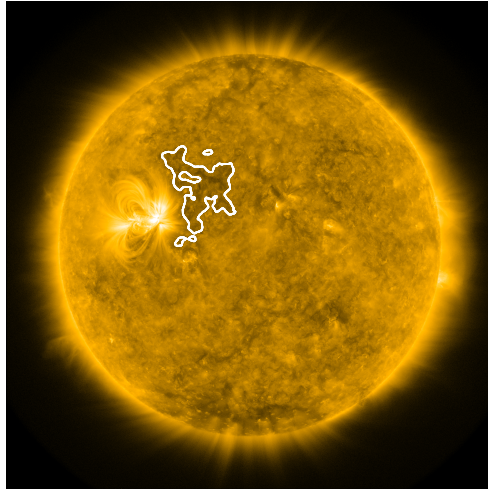


Figure A.4: SDO/AIA 171 Å observation of 2018 April 22 19:24. The dark halo adjacent to AR NOAA 12706 is outlined in white.

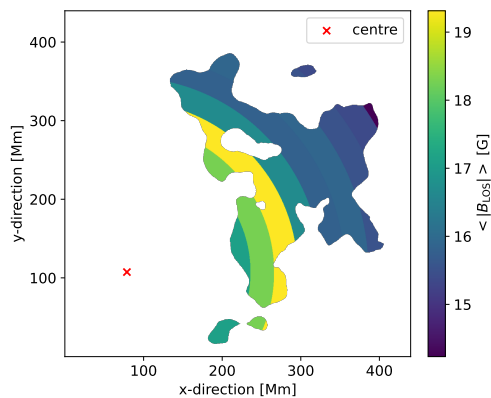


Figure A.5: The $\langle |B_{\text{LOS}}| \rangle$ inside concentric rings around the AR given as a function of distance to the AR centre for the SDO observations taken on 2018 April 22 19:24.

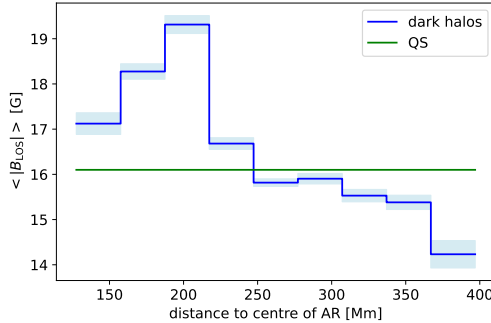


Figure A.6: The $\langle |B_{\text{LOS}}| \rangle$ in dependence of distance to the AR for the 2018 April 22 SDO observations. We show the $\langle |B_{\text{LOS}}| \rangle$ inside the dark halo in blue. The lighter blue colour denotes the uncertainty of the mean σ_M of these values. The $\langle |B_{\text{LOS}}| \rangle$ for the QS is given in green.

A.3 SDO 2018 April 22 data set

We studied the same SDO data set from 2018 April 22 19:24 (with the HMI magnetogram from 19:24:24, and the three AIA channels at 171 Å, 193 Å, and 211 Å from 19:24:09, 19:24:04, and 19:24:09, respectively) as Lezzi et al. (2023). It contains AR NOAA 12706 and a dark halo adjacent to it in the west (see Fig. A.4). We aim to analyse the photospheric magnetic field of this dark halo and compare the results to the dark halos analysed in Sect. 3.4.3.2 and by Lezzi et al. (2023). For this purpose we produced level 1.5 data for the 171 Å observation and additionally normalised the intensity to the exposure time. The co-temporal SDO/HMI LOS magnetogram was re-scaled and re-projected to the SDO/AIA image using the SunPy reproject package.

In order to re-create their contours we tested different filters and filter settings and found that a uniform filter with a size of 40 pixels yields the closest result to theirs. We first convolved the 171 Å image with this uniform filter and then applied a 55% mean disc intensity threshold to identify the dark halo next to the AR NOAA 12706. These contours are very similar to the ones we would obtain by convoluting the image with a Gaussian filter and then applying an intensity-threshold of 75% of the mean QS intensity at disc centre (as we did in Sect. 3.3.1).

We also selected the same reference QS area in the north-east of the solar disc which has a size of $250'' \times 337''$.

We applied the same noise level of 8 G as used by Lezzi et al. (2023) to derive the unsigned magnetic field, $\langle |B_{\text{LOS}}| \rangle$, by averaging the absolute values in the pixels above this noise level. We obtained $\langle |B_{\text{LOS}}| \rangle = 15.6$ G in the dark halo and $\langle |B_{\text{LOS}}| \rangle = 16.1$ G in the QS. The QS value compares well to the one presented in Lezzi et al. (2023), however, the value for the dark halo is 1.4 G lower than theirs. This result is consistent with our previous findings for the 2021 November 5 Solar Orbiter observations in the sense that the $\langle |B_{\text{LOS}}| \rangle$ in the DH is somewhat lower than in the QS.

In the same way as for the 2021 November 5 Solar Orbiter observation, we calculated the $\langle |B_{\text{LOS}}| \rangle$ inside concentric rings around the AR. We derived the centre of the AR by computing the geometric centre of magnetic elements with field strengths above 100 G within an area of ~ 175 Mm (400 pixels) around the clearly visible leading sunspot. As in Sect. 3.4.3.2 we calculated the $\langle |B_{\text{LOS}}| \rangle$ inside each concentric ring with a width of 30 Mm starting at ~ 130 Mm (29 pixel). This is shown in Fig. A.5.

Although we do not observe a gradual decrease in the unsigned magnetic field from the inner to the outer boundaries of the dark halo, the magnetic field is clearly strong close to the AR centre and weakest at its maximum distance. This $\langle |B_{\text{LOS}}| \rangle$ -distance dependence is shown in Fig. A.6. In the ring closest to the AR centre the dark halo has a value of 17.1 G, which rises to 19.3 G at $d=200$ Mm, but then continuously decreases. At a distance of ~ 250 Mm the $\langle |B_{\text{LOS}}| \rangle$ drops below the mean QS value. This general trend agrees with that already observed in the 2021 November 5 Solar Orbiter observations (see Fig. 3.9). It is noteworthy that also for this data set the variation of the $\langle |B_{\text{LOS}}| \rangle$ distribution within the dark halo itself is more pronounced than the difference between the $\langle |B_{\text{LOS}}| \rangle$ averaged over the entire dark halo and in the QS.

Bibliography

- Alfvén, H. 1941, On the solar corona, *Arkiv for Matematik, Astronomi och Fysik*, **27A**, 1
- Alissandrakis, C. E. 1981, On the computation of constant alpha force-free magnetic field, *Astronomy & Astrophysics*, **100**, 197
- Altschuler, M. D. & Newkirk, G. 1969, Magnetic Fields and the Structure of the Solar Corona. I: Methods of Calculating Coronal Fields, *Solar Physics*, **9**, 131
- Altschuler, M. D., Trotter, D. E., & Orrall, F. Q. 1972, Coronal Holes, *Solar Physics*, **26**, 354
- Andretta, V. & Del Zanna, G. 2014, The EUV spectrum of the Sun: SOHO CDS NIS radiances during solar cycle 23, *Astronomy & Astrophysics*, **563**, A26
- Antiochos, S. K. & Noci, G. 1986, The Structure of the Static Corona and Transition Region, *Astrophysical Journal*, **301**, 440
- Anusha, L. S., Solanki, S. K., Hirzberger, J., et al. 2017, Statistical evolution of quiet-Sun small-scale magnetic features using Sunrise observations, *Astronomy & Astrophysics*, **598**, A47
- Aschwanden, M. J. 2004, *Physics of the solar corona: an introduction*, Springer-Praxis books in geophysical sciences (Springer Berlin, Heidelberg)
- Athay, R. G. & White, O. R. 1978, Chromospheric and coronal heating by sound waves., *Astrophysical Journal*, **226**, 1135
- Athay, R. G. & White, O. R. 1979, Chromospheric oscillations observed with OSO 8. IV. Power and phase spectra for C IV., *Astrophysical Journal*, **229**, 1147

- Baker, D., van Driel-Gesztelyi, L., Mandrini, C. H., et al. 2009, MAGNETIC RECONNECTION ALONG QUASI-SEPARATRIX LAYERS AS A DRIVER OF UBIQUITOUS ACTIVE REGION OUTFLOWS, *The Astrophysical Journal*, **705**, 926
- Barthol, P., Gandorfer, A. M., Solanki, S. K., et al. 2011, The Sunrise Mission, *Solar Physics*, **268**, 1
- Bellot Rubio, L. & Orozco Suárez, D. 2019, Quiet Sun magnetic fields: an observational view, *Living Reviews in Solar Physics*, **16**, 1
- Berkefeld, T., Schmidt, W., Soltau, D., et al. 2011, The wave-front correction system for the sunrise balloon-borne solar observatory, *Solar Physics*, **268**, 103
- Biermann, L. 1948, Über die Ursache der chromosphärischen Turbulenz und des UV-Exzesses der Sonnenstrahlung, *Zeitschrift für Astrophysik*, **25**, 161
- Bumba, V. & Howard, R. 1965, A Study of the Development of Active Regions on the Sun., *Astrophysical Journal*, **141**, 1492
- Castellanos Durán, J., Lagg, A., Solanki, S. K., et al. 2020, Detection of the strongest magnetic field in a sunspot light bridge, *The Astrophysical Journal*, **895**, 129
- Charbonneau, P. 2020, Dynamo models of the solar cycle, *Living Reviews in Solar Physics*, **17**, 1
- Chen, Y., Peter, H., & Przybylski, D. 2024, Investigating explosive events in a 3D quiet-Sun model: Transition region and coronal response, *arXiv e-prints*, arXiv:2411.11068
- Chen, Y., Przybylski, D., Peter, H., et al. 2021, Transient small-scale brightenings in the quiet solar corona: A model for campfires observed with Solar Orbiter, *Astronomy & Astrophysics*, **656**, L7
- Chitta, L., Peter, H., Solanki, S., et al. 2017, Solar coronal loops associated with small-scale mixed polarity surface magnetic fields, *The Astrophysical Journal Supplement Series*, **229**, 4

- Cranmer, S. R. 2009, Coronal Holes, *Living Reviews in Solar Physics*, **6**, 3
- Cranmer, S. R. & Winebarger, A. R. 2019, The properties of the solar corona and its connection to the solar wind, *Annual Review of Astronomy and Astrophysics*, **57**, 157
- Crutcher, R. M. & Kemball, A. J. 2019, Review of Zeeman Effect Observations of Regions of Star Formation, *Frontiers in Astronomy and Space Sciences*, **6**
- del Toro Iniesta, J. C. 2003, Introduction to Spectropolarimetry (Cambridge University Press)
- Doschek, G. A., Mariska, J. T., Warren, H. P., et al. 2007, Nonthermal Velocities in Solar Active Regions Observed with the Extreme-Ultraviolet Imaging Spectrometer on Hinode, *The Astrophysical Journal*, **667**, L109
- Doschek, G. A., Warren, H. P., Mariska, J. T., et al. 2008, Flows and Nonthermal Velocities in Solar Active Regions Observed with the EUV Imaging Spectrometer on Hinode: A Tracer of Active Region Sources of Heliospheric Magnetic Fields?, *Astrophysical Journal*, **686**, 1362
- Edlén, B. 1943, Die Deutung der Emissionslinien im Spektrum der Sonnenkorona. Mit 6 Abbildungen., *Zeitschrift für Astrophysik*, **22**, 30
- Gandorfer, A., Grauf, B., Barthol, P., et al. 2011, The filter imager SuFI and the image stabilization and light distribution system ISLiD of the sunrise balloon-borne observatory: instrument description, *Solar Physics*, **268**, 35
- Gandorfer, A., Grauf, B., Staub, J., et al. 2018, The High Resolution Telescope (HRT) of the Polarimetric and Helioseismic Imager (PHI) onboard Solar Orbiter, in *Space Telescopes and Instrumentation 2018: Optical, Infrared, and Millimeter Wave*, ed. M. Lystrup, H. A. MacEwen, G. G. Fazio, N. Batalha, N. Siegler, & E. C. Tong, Vol. 10698, International Society for Optics and Photonics (SPIE), 106984N

- Garton, T. M., Gallagher, P. T., & Murray, S. A. 2018, Automated coronal hole identification via multi-thermal intensity segmentation, *Journal of Space Weather and Space Climate*, **8**, A02
- Gary, G. A. 2001, Plasma Beta above a Solar Active Region: Rethinking the Paradigm, *Solar Physics*, **203**, 71
- Gorman, J., Chitta, L. P., Peter, H., et al. 2023, Beyond small-scale transients: A closer look at the diffuse quiet solar corona, *Astronomy & Astrophysics*, **678**, A188
- Gošić, M., Bellot Rubio, L. R., del Toro Iniesta, J. C., et al. 2016, The Solar Internetwork. II. Flux Appearance and Disappearance Rates, *Astrophysical Journal*, **820**, 35
- Gošić, M. 2015, The Solar Internetwork, PhD thesis, University of Granada, Granada, Spain
- Grotian, W. 1939, Zur Frage der Deutung der Linien im Spektrum der Sonnenkorona, *Naturwissenschaften*, **27**, 214
- Hale, G. E. 1908, On the Probable Existence of a Magnetic Field in Sun-Spots, *Astrophysical Journal*, **28**, 315
- Hale, G. E. & Ellerman, F. 1903, The Rumford spectroheliograph of the Yerkes Observatory, *Publications of the Yerkes Observatory*, **3**, 1.1
- Harra, L. K., Sakao, T., Mandrini, C. H., et al. 2008, Outflows at the Edges of Active Regions: Contribution to Solar Wind Formation?, *The Astrophysical Journal*, **676**, L147
- Hathaway, D. H. 2015, The solar cycle, *Living reviews in solar physics*, **12**, 4
- Heinemann, S. G., Temmer, M., Heinemann, N., et al. 2019, Statistical Analysis and Catalog of Non-polar Coronal Holes Covering the SDO-Era Using CATCH, *Solar Physics*, **294**, 144

- Hirzberger, J., Bonet, J. A., Vázquez, M., et al. 1999, Time Series of Solar Granulation Images. II. Evolution of Individual Granules, *Astrophysical Journal*, **515**, 441
- Hofmeister, S. J., Veronig, A., Reiss, M. A., et al. 2017, Characteristics of Low-latitude Coronal Holes near the Maximum of Solar Cycle 24, *The Astrophysical Journal*, **835**, 268
- Hollweg, J. V. 1978, Fast wave evanescence in the solar corona, *Geophysical Research Letters*, **5**, 731
- Jin, C. L., Wang, J. X., Song, Q., et al. 2011, The Sun's Small-scale Magnetic Elements in Solar Cycle 23, *Astrophysical Journal*, **731**, 37
- Kahil, F., Hirzberger, J., Solanki, S. K., et al. 2022, The magnetic drivers of campfires seen by the Polarimetric and Helioseismic Imager (PHI) on Solar Orbiter, *Astronomy & Astrophysics*, **660**, A143
- Kippenhahn, R. & Möllenhoff, C. 1975, *Elementare Plasmaphysik* (Mannheim, Wien, Zürich: Bibliographisches Institut)
- Lemen, J., Title, A., Akin, D., et al. 2011, The Atmospheric Imaging Assembly (AIA) on the Solar Dynamics Observatory (SDO), *Solar Physics*, **275**, 17
- Lezzi, S. M., Andretta, V., Murabito, M., et al. 2023, Dark halos around solar active regions. I. Emission properties of the dark halo around NOAA 12706, *Astronomy & Astrophysics*, **680**, A61
- Lezzi, S. M., Long, D. M., Andretta, V., et al. 2024, First Solar Orbiter observation of a dark halo in the solar atmosphere, *Astronomy & Astrophysics*, **690**, A342
- Linker, J. A., Caplan, R. M., Downs, C., et al. 2017, The Open Flux Problem, *The Astrophysical Journal*, **848**, 70
- Livingston, W. 2002, Sunspots observed to physically weaken in 2000–2001, *Solar Physics*, **207**, 41

- Martínez Pillet, V., del Toro Iniesta, J. C., Álvarez-Herrero, A., et al. 2011, The Imaging Magnetograph eXperiment (IMaX) for the Sunrise Balloon-Borne Solar Observatory, *Solar Physics*, **268**, 57
- Martínez González, M. J., Manso Sainz, R., Asensio Ramos, A., et al. 2012, DEAD CALM AREAS IN THE VERY QUIET SUN, *The Astrophysical Journal*, **755**, 175
- Morgan, H. & Druckmüller, M. 2014, Multi-Scale Gaussian Normalization for Solar Image Processing, *Solar Physics*, **289**, 2945
- Müller, D., St. Cyr, O. C., Zouganelis, I., et al. 2020, The Solar Orbiter mission. Science overview, *Astronomy & Astrophysics*, **642**, A1
- Munro, R. H. & Withbroe, G. L. 1972, Properties of a Coronal “hole” Derived from Extreme-Ultraviolet Observations, *Astrophysical Journal*, **176**, 511
- November, L. J. & Koutchmy, S. 1996, White-Light Coronal Dark Threads and Density Fine Structure, *Astrophysical Journal*, **466**, 512
- Nölke, J. D., Solanki, S. K., Hirzberger, J., et al. 2023, Coronal voids and their magnetic nature, *Astronomy & Astrophysics*, **678**, A196
- Parker, E. N. 1972, Topological dissipation and the small-scale fields in turbulent gases, *Astrophysical Journal*, **174**, 499
- Parker, E. N. 1983, Magnetic neutral sheets in evolving fields-part two-formation of the solar corona, *Astrophysical Journal*, **264**, 642
- Parker, E. N. 1988, Nanoflares and the solar X-ray corona, *The Astrophysical Journal*, **330**, 474
- Payne, A. V. & Sun, X. 2021, Emerging Dimming as Coronal Heating Episodes, *Astrophysical Journal*, **912**, 1
- Pesnell, W. D., Thompson, B. J., & Chamberlin, P. C. 2012, The Solar Dynamics Observatory (SDO), *Solar Physics*, **275**, 3
- Peter, H., Bingert, S., & Kamio, S. 2012, Catastrophic cooling and cessation of heating in the solar corona, *Astronomy & Astrophysics*, **537**, A152

- Peter, H. & Dwivedi, B. N. 2014, Discovery of the Sun's million-degree hot corona, *Frontiers in Astronomy and Space Sciences*, **1**, 2
- Petrovay, K. & Szakaly, G. 1993, The origin of intranetwork fields: a small-scale solar dynamo, *Astronomy & Astrophysics*, **274**, 543
- Priest, E. 2014, *Magnetohydrodynamics of the Sun* (Cambridge University Press)
- Priest, E., Chitta, L., & Syntelis, P. 2018, A cancellation nanoflare model for solar chromospheric and coronal heating, *The Astrophysical Journal Letters*, **862**, L24
- Rempel, M., Bhatia, T., Bellot Rubio, L., et al. 2023, Small-scale dynamos: from idealized models to solar and stellar applications, *Space Science Reviews*, **219**, 36
- Rincon, F. & Rieutord, M. 2018, The Sun's supergranulation, *Living Reviews in Solar Physics*, **15**, 6
- Rochus, P., Auchère, F., Berghmans, D., et al. 2020, The Solar Orbiter EUV instrument: The Extreme Ultraviolet Imager, *Astronomy & Astrophysics*, **642**, A8
- Rosner, R., Tucker, W. H., & Vaiana, G. S. 1978, Dynamics of the quiescent solar corona., *Astrophysical Journal*, **220**, 643
- Sakao, T., Kano, R., Narukage, N., et al. 2007, Continuous Plasma Outflows from the Edge of a Solar Active Region as a Possible Source of Solar Wind, *Science*, **318**, 1585
- Schatten, K. H., Wilcox, J. M., & Ness, N. F. 1969, A model of interplanetary and coronal magnetic fields, *Solar Physics*, **6**, 442
- Schou, J., Scherrer, P. H., Bush, R. I., et al. 2012, Design and Ground Calibration of the Helioseismic and Magnetic Imager (HMI) Instrument on the Solar Dynamics Observatory (SDO), *Solar Physics*, **275**, 229
- Schrijver, C. J. & Harvey, K. L. 1994, The Photospheric Magnetic Flux Budget, *Solar Physics*, **150**, 1

- Schwarzschild, M. 1948, On Noise Arising from the Solar Granulation., *Astrophysical Journal*, **107**, 1
- Seehafer, N. 1978, Determination of constant α force-free solar magnetic fields from magnetograph data, *Solar Physics*, **58**, 215
- Serviss, G. P. 1909, Curiosities of the sky: A popular presentation of the great riddles and mysteries of astronomy (Createspace Independent Publishing Platform)
- Singh, T., Sterling, A. C., & Moore, R. L. 2021, The Missing Cool Corona in the Flat Magnetic Field around Solar Active Regions, *The Astrophysical Journal*, **909**, 57
- Sinjan, J., Calchetti, D., Hirzberger, J., et al. 2022, The on-ground data reduction and calibration pipeline for SO/PHI-HRT, in Society of Photo-Optical Instrumentation Engineers (SPIE) Conference Series, Vol. 12189, Software and Cyberinfrastructure for Astronomy VII, 121891J
- Sinjan, J., Calchetti, D., Hirzberger, J., et al. 2022, The on-ground data reduction and calibration pipeline for SO/PHI-HRT, in Software and Cyberinfrastructure for Astronomy VII, Vol. 12189, SPIE, 612–628
- Solanki, S., Barthol, P., Danilovic, S., et al. 2010a, SUNRISE: instrument, mission, data, and first results, *The Astrophysical Journal Letters*, **723**, L127
- Solanki, S., Riethmüller, T., Barthol, P., et al. 2017, The second flight of the SUNRISE balloon-borne solar observatory: overview of instrument updates, the flight, the data, and first results, *The Astrophysical Journal Supplement Series*, **229**, 2
- Solanki, S. K. 1993, Smallscale Solar Magnetic Fields - an Overview, *Space Science Reviews*, **63**, 1
- Solanki, S. K., Barthol, P., Danilovic, S., et al. 2010b, Sunrise: INSTRUMENT, MISSION, DATA, AND FIRST RESULTS, *The Astrophysical Journal Letters*, **723**, L127

- Solanki, S. K., del Toro Iniesta, J. C., Woch, J., et al. 2020, The Polarimetric and Helioseismic Imager on Solar Orbiter, *Astronomy & Astrophysics*, **642**, A11
- Solanki, S. K., Inhester, B., & Schüssler, M. 2006, The solar magnetic field, *Reports on Progress in Physics*, **69**, 563
- SPICE Consortium, Anderson, M., Appourchaux, T., et al. 2020, The Solar Orbiter SPICE instrument - An extreme UV imaging spectrometer, *Astronomy & Astrophysics*, **642**, A14
- Spörer, G. 1894, Beobachtungen von Sonnenflecken in den Jahren 1885 bis 1893, *Publikationen des Astrophysikalischen Observatoriums zu Potsdam*, **32**
- St. John, C. E. 1911, Motion and Condition of Calcium Vapor Over Sun-Spots and Other Special Regions. I., *Astrophysical Journal*, **34**, 57
- Stansby, D., Yeates, A., & Badman, S. T. 2020, pfsspy: A Python package for potential field source surface modelling, *Journal of Open Source Software*, **5**, 2732
- Stephenson, F. R. & Willis, D. M. 1999, The earliest drawing of sunspots, *Astronomy and Geophysics*, **40**, 21
- Stix, M. 2002, *The Sun An Introduction*, Astronomy and Astrophysics Library (Springer Berlin, Heidelberg)
- The SunPy Community, Barnes, W. T., Bobra, M. G., et al. 2020, The SunPy Project: Open Source Development and Status of the Version 1.0 Core Package, *The Astrophysical Journal*, **890**, 68
- van Ballegooijen, A. A. 1986, Cascade of Magnetic Energy as a Mechanism of Coronal Heating, *Astrophysical Journal*, **311**, 1001
- Waldmeier, M. 1956, Synoptische Karten der Sonnenkorona. Mit 16 Textabbildungen, *Zeitschrift für Astrophysik*, **38**, 219
- Waldmeier, M. 1957, *Die Sonnenkorona II*, Geophysik und Astrophysik Monographien (Birkhäuser Verlag, Basel)

- Wang, Y. M., Robbrecht, E., & Muglach, K. 2011, The Evolution of Dark Canopies Around Active Regions, *Astrophysical Journal*, **733**, 20
- Wiegelmann, T. & Sakurai, T. 2012, Solar Force-free Magnetic Fields, *Living Reviews in Solar Physics*, **9**, 5
- Wiegelmann, T. & Solanki, S. K. 2004, Similarities and Differences between Coronal Holes and the Quiet Sun: Are Loop Statistics the Key?, *Solar Physics*, **225**, 227
- Withbroe, G. L. & Noyes, R. W. 1977, Mass and energy flow in the solar chromosphere and corona, *Annual review of astronomy and astrophysics*, **15**, 363
- Zeeman, P. 1897a, VII. Doublets and triplets in the spectrum produced by external magnetic forces, *The London, Edinburgh, and Dublin Philosophical Magazine and Journal of Science*, **44**, 55
- Zeeman, P. 1897b, XXXII. On the influence of magnetism on the nature of the light emitted by a substance, *The London, Edinburgh, and Dublin Philosophical Magazine and Journal of Science*, **43**, 226
- Zeeman, P. 1897c, XXXIII. Doublets and triplets in the spectrum produced by external magnetic forces.—(II.), *The London, Edinburgh, and Dublin Philosophical Magazine and Journal of Science*, **44**, 255
- Zhang, J., Yang, S., Liu, Y., et al. 2012, EMERGING DIMMINGS OF ACTIVE REGIONS OBSERVED BY THE SOLAR DYNAMICS OBSERVATORY, *The Astrophysical Journal Letters*, **760**, L29
- Zhuleku, J., Warnecke, J., & Peter, H. 2020, Stellar coronal X-ray emission and surface magnetic flux, *Astronomy & Astrophysics*, **640**, A119

Acknowledgments

I am grateful to the members of my Thesis Advisory Committee (TAC), Sami, Johann, Hardi, and Karl-Heinz, for their support throughout my PhD. Sami has guided my PhD projects and provided me with numerous opportunities to attend conferences and engage with the solar community, helping me find my place within it. My day-to-day supervisors Johann and Hardi offered consistent supervision and support, always making themselves available for discussion or questions despite their busy schedules. I also want to thank my university supervisor Karl-Heinz, who not only showed continuous interest in my projects but also took it upon himself to help me get to know the university and the city of Braunschweig, giving me a personal tour and inviting me to present my research at the faculty seminar. I want to thank Pradeep, who, although not officially part of the TAC, frequently contributed to discussions on my projects and always had an open door for questions and exchange. I also want to thank the International Max Planck Research School (IMPRS) and our coordinator Sonja for enabling and supporting my doctoral work.

Appreciation also goes to my student buddy Jonas, who helped me navigate the early stages of the PhD during the pandemic lockdown by explaining how things work and making the initial transition much easier. Working with Isabela during our term as student representatives was a truly rewarding experience; we collaborated smoothly and complemented each other's strengths. Acknowledgement is also due to the secretaries, administrative staff, and IT support for their efforts in keeping everything running smoothly behind the scenes.

The friendships formed during my PhD through shared offices, business trips, and occasional private travels made my time at MPS truly enjoyable. I'm grateful to many of you and would like to mention a few in particular. Kok Leng played a key role in creating a welcoming atmosphere at MPS, uniting PhD students and postdocs by fostering a sense of community through laughter. She always

ensured that no one missed the common lunch, personally stopping by each desk every day to bring us along. The trips Yara and I took after business travels were amazing. Visiting the Giant's Causeway was especially memorable, with its stunning landscape leaving a lasting impression. Another adventure took us to Rome, where Yara showed me the city's most iconic sights as well as hidden gems that made it feel even more special. Despite the challenge when the hotel failed to provide any toilet paper on a public holiday, we still had an incredible time together. A big thanks to Jesper for two unforgettable Rocky Mountain adventures, an incredible full-day hike and a drive up the highest passes open that season. Nikolina kept my plants alive whenever I was away from Göttingen for longer periods of time. I want to thank my office mates Ziwen, Abhas, Amanda, Lisa, Yara, Jamie, and Philipp for the scientific discussions and all the fun we had together. I also appreciated the daily friendly greetings from the Lunchbox Mensa staff, who continued to greet us even when we occasionally met at Central Mensa on Saturdays. In this context, I want to thank Fernando and Xiang, the other founding members of our Saturday lunch group. What started with the three of us meeting at Central Mensa soon grew into a tradition and many others joined, with lunch followed by coffee in the city centre, sometimes lasting into the evening.

Finally, I am deeply grateful to my family, my parents, siblings, partner, our dog Egon, and to close friends for their unwavering support and patience throughout this journey. When visiting home, Egon always brought so much joy and excitement into my life that I did not mind at all the huge amounts of dirt he also carried into my bed. Of course, my mother's generous supplies of Tupperware boxes filled with home-cooked meals were always a much-appreciated comfort.

This work was supported by the International Max Planck Research School (IMPRS) for Solar System Science at the University of Göttingen and at TU Braunschweig.

Publications

REFEREED PUBLICATION

Nölke, J. D., Solanki, S. K., Hirzberger, J., et al. 2023, Coronal voids and their magnetic nature, *Astronomy & Astrophysics*, **678**, A196, doi:10.1051/0004-6361/202346040

CONFERENCE CONTRIBUTIONS

- Nölke, J. D., Solanki, S. K., Hirzberger, J., et al. (March–April 2025). ‘Magnetic structure of coronal dark halos’ [Oral Presentation]. DPG Spring Meeting of the Matter and Cosmos Section (SMuK). Göttingen, Germany.
- Nölke, J. D., Solanki, S. K., Hirzberger, J., et al. (February 2025). ‘Magnetic structure of coronal dark halos’ [Oral Presentation]. SDO 2025 Science Workshop: A Gathering of the Helio-hive! Boulder, CO, USA.
- Nölke, J. D., Solanki, S. K., Hirzberger, J., et al. (September 2024). ‘Magnetic structure of coronal dark halos’ [Poster Presentation]. 17th European Solar Physics Meeting (ESPM-17). Turin, Italy.
- Nölke, J. D., Solanki, S. K., Hirzberger, J., et al. (April 2024). ‘Magnetic structure of coronal dark halos’ [Poster Presentation]. Joint Solar Orbiter, Parker Solar Probe, and DKIST Meeting. San Antonio, TX, USA.
- Nölke, J. D., Solanki, S. K., Hirzberger, J., et al. (May 2023). ‘Coronal voids and their magnetic nature’ [Oral Presentation]. SOLARNET Conference: The Many Scales of the Magnetic Sun. Potsdam, Germany.
- Nölke, J. D., Solanki, S. K., Hirzberger, J., et al. (September 2022). ‘Dark voids in the quiet Sun corona and their magnetic nature’ [Oral Presentation]. 8th Solar Orbiter Workshop. Belfast, Northern Ireland, UK.

Curriculum Vitae

PERSONAL DATA

Name: Jonathan David Nölke

Place of birth: Paderborn, Germany

EDUCATION

- **Doctoral Researcher** **05/2021–Present**
at Max Planck Institute for Solar System Research, Göttingen (Germany)
enrolled at TU Braunschweig, Braunschweig (Germany)
Title of thesis: ‘Dark features in the solar corona and the underlying magnetic field studied with Solar Orbiter’
Thesis advisory committee: Sami Solanki, Johann Hirzberger, Hardi Peter, and Karl-Heinz Glaßmeier
- **Master of Science in Physics** **04/2013–03/2021**
Bielefeld University, Bielefeld (Germany, since 10/2018)
Focus: radio astronomy
Title of thesis: ‘Glitches and Timing Noise in Radio Pulsars’; supervisor: Joris Verbiest
Paderborn University, Paderborn (Germany, until 09/2018)
Focus: Computational Material Science
- **Bachelor of Science in Physics** **10/2007–08/2012**
Paderborn University, Paderborn (Germany)
Title of thesis: ‘Trends in the Electronic Structure of Alkali Niobates’; supervisor: Arno Schindlmayr
Universidad de Zaragoza, Zaragoza (Spain, 02/2011–09/2011)
Erasmus semester

TRAVEL FUNDING AWARDED

- 17th European Solar Physics Meeting (ESPM-17). Turin, Italy. September 2024.
- SOLARNET Conference: The Many Scales of the Magnetic Sun. Potsdam, Germany. May 2023.
- 8th Solar Orbiter Workshop. Belfast, Northern Ireland, UK. September 2022.

SUMMER SCHOOLS

- SOLARNET Summer School: Solar Atmospheric Dynamics – From Waves to Instabilities and Jets. Gyula, Hungary. 25–30 June 2023.
- The different spatio-temporal scales of the solar magnetism. L'Aquila, Italy. April 11–15 2022.

TEACHING EXPERIENCE

- Teaching tutorials at courses about the Sun and planetary system at the University of Göttingen and at TU Braunschweig.

INSTITUTIONAL SERVICE

- Student representative (07/2023–07/2024).
- Member of organising team for Solar System Science seminar 'S3' at MPS (03/2022–09/2024).
- Public outreach: 'Max Planck goes to School', talks for visiting pupils and students, institute tours.